Doctorado en Física

Universidad de Valencia

Crystal growth and characterization of $Zn_{1-x}Mg_xO$ advanced micro- and nanostructures

Tesis doctoral:
Esther Luisa de Prado Fernández

Directora:
Dra. María del Carmen Martínez Tomás

Valencia, Abril 2018

VNIVERSITAT DE VALÈNCIA Facultat de Física

Dpto. Física Aplicada y Electromagnetismo
Edificio de Investigación
Universitat de Valencia
C/ Dr. Moliner, 50 - 46100 Burjassot (Valencia)
Spain

T: +34 9635 44754
F: +34 9635 43146

María del Carmen Martínez Tomás, Catedrática de Universidad

INFORMA:

Que el presente trabajo titulado: "*Crystal growth and characterization of* $Zn_{1-x}Mg_xO$ *advanced micro- and nanostructures* (Crecimiento cristalino y caracterización de micro y nanoestructuras avanzadas de $Zn_{1-x}Mg_xO$)", ha sido realizado en el Departamento de Física Aplicada y Electromagnetismo de la Universitat de València por la licenciada en Física Dña. *Esther de Prado Fernández* bajo mi dirección y constituye su Tesis Doctoral.

Y para que así conste y en cumplimiento de la normativa vigente, emito el presente informe favorable para que se efectúe el depósito de la referida tesis doctoral, lo que firmo en Burjassot, a 10 de abril de 2018

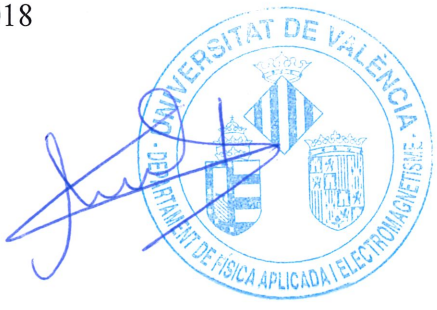

M. Carmen Martínez Tomás

A mi madre
A Natálka

It is the questions we can not answer that teach us the most. They teach us how to think.

The Wise Man's Fear.
Patrick Rothfuss

Agradecimientos

A veces no conoces el verdadero valor de un momento hasta que se convierte en recuerdo, como bien decía Theodor Seuss Geisel. Estos cuatro años constituyen un álbum inestimable de recuerdos y me gustaría dedicar unas palabras a todos aquellos que con su ayuda directa o indirecta han hecho posible este proyecto.

En primer lugar quiero darle las gracias a mi directora la profesora Dra. M. Carmen Martínez no solo en el aspecto académico, por su enorme dedicación en mi formación y corrección de esta tesis, sino también en el ámbito personal. Gracias por tu preocupación, por tu cariño, por tus consejos y por recordarme siempre que no debo menospreciar mi trabajo. Y también por transmitirme tu inquietud por analizar cada detalle y por compartir conmigo la ilusión con la que hemos esperado y recibido cada pico de difracción. Eres una gran profesora en todos los aspectos y me siento muy feliz y orgullosa de que hayas sido mi mentora.

También quería dar las gracias al profesor Dr. Vicente Muñoz, gracias por todas las horas que has dedicado a mi formación y corrección de mis trabajos, por tus sabios consejos, por enseñarme a ver las cosas con perspectiva y por tu preocupación continua, no solo por mi tesis, sino también por mí y mi familia.

Por otro lado, gracias también a todos los compañeros que son y han sido parte de mi grupo, a Antonia por estar siempre disponible a echar una mano, a Said por sus ideas, sus comentarios y su ayuda con el TEM. Thank you Kumar for be always so happy and friendly. A Ade, Lluis y Vicente, por todos los buenos momentos que hemos pasado juntos, por compatir nuestras penas y alegrías de doctorandos

y por sacarme cada día una sonrisa. También, a los que no formáis parte de mi grupo, Braulio, Càndid, David, Diego, Gloria, Javi y Martina por compatir no solo conversaciones y cafés en el departamento sino también, cenitas, buñuelos d'or, cremás y otras tantas salidas por Valencia.

Gracias a todos los miembros del departamento de Física Aplicada y Electromagnetismo de la Universidad de Valencia y a los miembros del SCSIE, en especial a aquellos con los que he tenido más trato, Alicia, Enrique, Pilar, Rafa, Tere y Tony, gracias por vuestra ayuda con el manejo de los equipos y por resolver cada una de mis dudas. También a los miembros de la secretaría del departamento, Antonio, Juanmi, Myriam y Tony, por hacernos siempre más fácil todos los tediosos papeleos y a las chicas de la limpieza Carmen y Santi, por su alegría y amabilidad así como por mover con cuidado cada uno de los chiquicientos poliedros de mi mesa para poder limpiarla.

Cambiando de escenario, un hecho que marca la trayectoria de la mayoría de los doctorandos son las estancias, yo tuve la oportunidad de hacer dos, una en Francia y otra en Madrid y si bien duraron poco comparado con el resto del doctorado, facilmente podrían llenar varias páginas de mi álbum mental de momentos felices.

Avec un style de vie qu'on amène d'un côté à l'autre, on arrive à quelque part, on rencontre de nouvelles personnes et puis, chacun va à un autre côté du monde, nous n'aurons que la mémoire... bien je vous ai connu pendant vos séjours, bien pendant le mien, je vous porterai toujours dans ma mémoire et dans mon coeur. Premièrement, je tiens à remercier ma très bonne amie Amira, merci d'être là au moment où j'en ai eu le plus besoin. Ensuite j'adresse un grand merci à toute l'équipe du CRHEA-CNRS, particulièrement à Jean-Yves Duboz pour me donner l'opportunité de travailler et d'apprendre au sein de son équipe et merci aussi à ceux avec lesquelles j'ai collaboré plus étroitement: Christiane Deparis, Jesús Zúñiga et Lars Kappei, je vous remercie pour tout ce que vous m'avez appris, pour votre patience et pour me traiter comme l'un des leurs. Merci aussi à Aimeric Courville, Anne-Marie Galiana, Eric Drezet, Olivier Tottereau et Virginie Brändli pour leur aide avec l'informatique, la logistique et l'utilisation des microscopes. I would like to thank also all my colleagues; Fulvio, Gema,

Kurtz, Michael, Roy, Sam and Stan for their support and friendship, I will keep an unforgettable memory of all of you.

Mi segunda estancia me brindó la oportunidad de volver a casa y a la universidad donde hice la carrera, la UCM. Recuerdo como si lo estuviese viviendo ahora mismo, la sensación de nerviosismo que tenía mi primer día de estancia, exactamente la misma que tuve mi primer día de clase allí, con 18 años. Iba a volver a ver a todos los que habían sido mis *profes*, solo que esta vez, ya no era una alumna sino que esta al otro lado de la barrera, junto a ellos. Echando la vista atrás creo que es ese cambio, esa evolución la que me hizo sentir, más que nerviosa, abrumada. Es una sensación que solo los que han estudiado y trabajado en el mismo sitio son capaces de comprender. Así, con mil mariposas en el estómago me dirijí al despacho de mi supervisora, la profesora Paloma Fernández y tras pocos minutos de estar hablando con ella todos mis miedos se desvanecieron. Gracias por todo el tiempo que me has dedicado, por toda tu ayuda y por hacerme perder el miedo a los congresos. Quiero dar las gracias también al resto del grupo de investigación de Física de Nanomateriales Electrónicos, Ana Cremades, Ana Urbieta, Bianchi Méndez, Carlos Díaz-Guerra, David Maestre, Emilio Nogales y Pedro Hidalgo, a los técnicos Carlos Romero y Esther Garrido, así como a mis compañeros becarios Alberto, Ali, Álvaro, Belén, Félix, Fer, Gregor, Jasmin, Jesús, Manu, María, Marta, Paloma, Papa y Víctor. Gracias por vuestra ayuda y por la gran acogida que me disteis.

Y ya, fuera de este micro-nanomundo científico, gracias a todos los "rosa-rosae" Alí, Dany, Elisa, Jasmina, Jorge, Lavi, Luis y Oleksii, por convertir nuestro adosado en un verdadero hogar, me llevo una gran amistad de nuestra convivencia. Muy en especial a mis dos chicos de "La Odisea", con los que he compartido más tiempo, viajes y aventuras; no hay nada que pueda deciros que no sepáis ya, tan solo recordaros que aunque la vida nos ha enviado a extremos distintos del planeta, somos los 3 mosqueteros y eso ni la distancia ni el tiempo podrá cambiarlo jamás.

Gracias a todos mis amigos de Madrid; Ali, Amanda, Anahí, Dano, Héctor, Inés, Javi, Jes, Marta, Patri, Pipe y Raquel, por recibirme con entusiasmo cada vez que volvía a casa, por interesaros siempre por

saber qué tal estaba o cómo iba mi tesis y por escuchar con interés cada vez que me ponía a hablar de picos de difracción.

Finalmente quiero agradecer a mi familia, a mis tías y primas Nana, Pitu, Montse y Tachi, gracias por haber estado ahí en los buenos y malos momentos. Chtěla bych poděkovat mé "sestře" Lucie za to, že pro mě znamená něco víc, než jen součást rodiny a pro všechnu její laskavost. A mi hermano Jorge por ser el mejor hermano mayor que podría tener, gracias por todo lo que has hecho y haces por mi. A mis padres por todos los sacrificios que habéis tenido que hacer para que yo llegara hasta aquí y muy especialmente a mi madre, por enseñarme a no rendirme, a perseguir mis metas, a ser siempre positiva y luchadora... por enseñarme a vivir. Gracias por tu incondicional confianza y apoyo.

List of Acronyms

2D Two dimensional
3D Three dimensional
AFM Atomic force microscopy
au Arbitrary units
BSE Back scattered electrons
CCD Charge coupled device
CL Cathodoluminescence
CNRS Centre National de la Recherche Scientifique
CRHEA Centre de Recherche sur l'Hétéro Epitaxie et ses Application
CSIC Consejo Superior de Investigaciones Científicas
DAP Donor-acceptor pair
DBR Distributed Bragg reflector
DL Deep level
EDX Energy dispersive spectroscopy
FWHM Full width at half maximum
HMD Hybrid multiple diffraction
HRXRD High resolution X-Ray diffraction
LIPSS Laser induced periodic surface structures
MBE Molecular beam epitaxy
MC Microcavity
MD Multiple diffraction
MOCVD Metal organic chemical vapor deposition
NBE Near band edge
NHs Nanohilos
NI Non iradiated
NWs Nanowires

O_{Zn} Oxygen antisite
PL Photoluminescence
PLD Pulsed laser deposition
PVT Physic vapor transport
QCSE Quantum confined Stark effect
RHEED Reflection high-energy electron diffraction
RMS Root Mean Square
RSM Reciprocal space map
RT Room temperature
SEM Scanning electron microscopy
SIMS Secondary ion mass spectrometry
UCM Universidad Complutense de Madrid
UV Ultraviolet
VLS Vapor-solid-liquid
V_O Oxygen vacancy
VS Vapor-solid
V_{Zn} Zinc vacancy
XRD X-Ray diffraction
V_{Zn} Interstitial zinc
Zn_O Zinc antisite

Contents

Part I

English version

Chapter 1

Introduction

Within the framework of the increasing research on semiconductor physics, the study of II-VI semiconductor compounds have become a fundamental field of material physics because their physical properties are unique to create a new generation of devices in the field of photonics and microelectronics. Between them, ZnO based semiconductors have gained substantial interest in the research community in part because of the ZnO large exciton binding energy of 60 meV, which is 2.4 times the effective thermal energy at room temperature and could lead to exciton lasing action even above room temperature. Furthermore, thanks to the high ZnO melting point and large cohesive energy, a low degradation of the material due to the generation of dislocations during the device operation can be expected. Finally, their constituent elements are abundant, nontoxic and low cost.

ZnO applications are very varied in different kind of devices. Many of these devices as light emitters, ultraviolet (UV) light detectors, UV-blue lasers, vertical-cavity surface emitting lasers... are based on the growth of layers, grown on different types of substrates, which must have morphological and structural properties of extreme quality [1–4]. In the nanoscale range, novel electrical, mechanical, chemical and optical properties are introduced. In particular one-dimensional ZnO nanostructures such as nanowires and nanorods have been extensively studied for other applications including chemical sensors, solar cells,

blue and UV light-emitting diodes, hydrogen storage and biomedical sciences [5–10].

On the other hand, the bandgap, the lattice parameters, the refractive index and many other properties of ZnO can be tuned by alloying ZnO with different materials. Among other, $Zn_{1-x}Mg_xO$ alloys have attracted considerable attention due to the similar ionic radii between Zn and Mg (Zn^{2+} (0.60Å) and Mg^{2+} (0.57Å)) [11]. This could raise the suspicion that ZnO-MgO alloy is easily obtainable. Nevertheless, ZnO has a wurtzite hexagonal structure while MgO has a rocksalt cubic one. In addition the solubility limit of Mg in ZnO depends on the employed growth method as well as the growth conditions. In fact, at the thermodynamic equilibrium this limit has been reported to be 4% mol [12]. These two drawbacks make the achievement of high quality monocrystalline $Zn_{1-x}Mg_xO$ alloys a really challenging issue.

Many conventional devices are based on simple structures that provide limited functionalities. The new technological requirements demand new configurations in order to create a new generation of devices in the field of photonics and microelectronics. In this context, nanowires (NWs) and multilayer structures present a special interest because they constitute the building blocks of many advanced devices.

The growth of $Zn_{1-x}Mg_xO$ NWs has been extensive studied using different methods such as metal organic chemical vapor deposition (MOCVD), pulsed laser deposition (PLD), hydrothermal, molecular beam epitaxy (MBE), vapor-liquid-solid (VLS), vapor-solid (VS) and physic vapor transport (PVT) [13–25]. These three latter offer some advantages which make them very interesting as growth methods, such as low cost and low temperature conditions. The benefits of NWs ordered structures is well known [26]. The typical self-organized growth mechanism for creating nanowires is the VLS which provides free-standing crystalline nanowires with fully controlled nucleation sites and diameters from pre-formed metal catalysts. Nevertheless the contamination caused by the use of a catalyst is a drawback that must have been into account and other ways to obtain them must to be explored. The aids of ex situ techniques, such as chemical etching or the use of patterned substrates, are desirable not only in fundamental research but also in future nanodevice design and fabrication. A

drawback of the former is that etching processes always lead to significant surface damage, and thus surface states are introduced into the nanostructures. Regarding to the latter, a very promising way to produce the needed substrates with surface structuration consists in the irradiation of the substrate surface with ultrashort laser pulses which generates the so-called Laser Induced Periodic Surface Structures (LIPSS). One of the first studies on this topic was performed in 1965 by Birnbaum [27] on several single crystal semiconductors. He explained the production of the grooves as diffraction effects produced at the focus of a lens. Several other explanations were proposed during the 1970's as frozen surface acoustic waves, plasma oscillations or interference between the incident and scattered waves. In 1983, Sipe *et al.* established a first principal theory for LIPSS formation [28], and a good agreement between experiments and theory was found by Young *et al.* [29]. More recently works which model LIPSS formation can be found elsewhere [30, 31]. Even though a complete understanding of LIPSS origin is still missing, it have been demonstrated that the use of the irradiated regions as 2D patterns enhances the growth of ordered nanostructures [32]. In the experiments usually reported in the literature irradiation was performed on single crystalline samples [30, 33], while the use of polycrystalline substrates has not been extensively exploited [32, 34]. That is, the difficulties and high cost associated to the production of such structures makes necessary to extend the research to procedures based on polycrystalline materials, rather than single crystals.

This framework allows us to address the question whether such an interesting material as $Zn_{1-x}Mg_xO$ could be satisfactorily obtained with two of the most pursued advantages, such as the growth of ordered NWs and without the use of catalyst. Surface patterning by LIPPS formation is a good candidate, as it has been remarked in the bibliography, but if in addition it could be done on polycrystalline samples, this might lead to cheaper and more competitive nanostructured devices in the field of photonics and microelectronics.

In this sense, one of the aims of this thesis is the attainment and characterization of highly ordered $Zn_{1-x}Mg_xO$ nanowires grown by an

easily, accessible and low cost method such as vapor-solid using patterned polycrystalline substrates.

Concerning the growth of $Zn_{1-x}Mg_xO$ epitaxial layers, there are many studies in which their optical and structural properties are studied. Due to the high quality required in photonic devices, usually $Zn_{1-x}Mg_xO$ epitaxial layers are grown by MBE, PLD and MOCVD [35–44]. Indeed, the fast progress of crystal growth techniques over the twentieth century has enabled the achievement of crystal structures that have singular and strongly interesting optical properties. Among them, semiconductor microcavities (MCs) concomitantly offer good optical confinement with a small mode volume and are promising candidates for achieve strong light-matter coupling [45]. In this structures the cavity polaritons, bosonic quasiparticles resulting from the strong coupling between excitons and confined cavity photons, can undergo to a Bose-Einstein condensate and emit coherent light, giving rise to the so-called polariton laser [46, 47]. As they do not require an electronic population inversion, polariton lasers are expected to present lower thresholds than conventional lasers [45]. Nevertheless, the evolution of such a laser, from a laboratory component to a useful commercial device, requires that it would be able to operate at room temperature (RT). Wide-bandgap semiconductors such as GaN [48] and ZnO [49] were proposed at the beginning of the last decade as appropriate candidates for RT operation because of their large exciton binding energy and oscillator strength. In ZnO, both quantities are much larger than in nitrides, and this feature makes ZnO-based structures an optimum choice for a blue-light and UV-emitting polariton laser device. For this reason, much effort has been devoted to study the strong-coupling in ZnO microcavities as well as the fabrication of ZnO-based polariton lasers [50–57]. These complex heterostructures usually are fabricated by sandwiching a ZnO layer between two sets of multilayers, which are formed by stacking two different bilayers. These multilayer system, more known as distributed Bragg reflectors (DBRs) must have two key properties: they should display a small lattice mismatch with respect to ZnO and, at the same time, a large refractive index contrast is needed. This is exactly where $Zn_{1-x}Mg_xO$ layers play a major role since their lattice parameters and refraction index depend

on the Mg amount and can be tuned until achieve a high reflectivity without sacrificing the MCs quality.

Despite the interest and the contribution to the advance of knowledge on such structures, almost all the studies performed on this topic until the beginning of this thesis were based on (0001) oriented ZnO, that is, without exploiting the benefits of other orientations. On the one hand, the use of quantum wells as active regions helps to enhance the Rabi splitting and makes the cavity polaritons more stable [45]. Nevertheless in polar quantum wells belonging to a *c*-oriented wurtzite materials, the quantum confined Stark effect (QCSE) aggravates the excitonic disorder due to quantum wells thickness fluctuations and creates a spatial separation of the electron and hole wavefunction. This leads to a reduction of the exciton oscillator strength and makes excitons more sensitive to non-radiative defects due to longer radiative lifetimes. On the other hand, in nonpolar and semipolar $Zn_{1-x}Mg_xO$/ZnO heterostructures it is possible to reduce, eventually nullify, the internal electric fields arisen due to the spontaneous and piezoelectric polarization mismatches between the different materials [58]. Thus it is desirable the growth of nonpolar or semipolar ZnO based MCs. Unfortunately, the nonpolar growth on sapphire substrates, which is the most frequently used substrate to grow ZnO and its related alloys, gives rise to a large density of stacking faults [59–61]. Because of this, in order to obtain highly quality samples, homoepitaxial growths must to be done.

Thus, given the interest of $Zn_{1-x}Mg_xO$ for constituting microcavities based on nonpolar and semipolar ZnO, a detailed study is needed, both of $Zn_{1-x}Mg_xO$/ZnO single layers, multilayers and complete MCs. Only a careful study of the structural properties of these complex heterostructures will allow to take all the advantages and benefits of these scarcely studied orientations.

In this respect the second aim of this thesis is to deep in the study of nonpolar and semipolar $Zn_{1-x}Mg_xO$/ZnO systems grown by MBE in order to obtain high quality microcavities, making special attention to the structural characterization.

For all the explained above, the objective of this thesis is to deep into some aspects related to such an interesting material as the ZnO-

MgO alloy thus covering some of the lacks revealed by the bibliography. First, the growth of high ordered $Zn_{1-x}Mg_xO$ nanowires by the vapor solid method without the use catalyst on polycrystalline substrates patterned by LIPPS formation. Next, the growth and characterization of high quality *m*- and *r*- oriented ZnO microcavities with $Zn_{1-x}Mg_xO$/ZnO distributed Bragg reflectors.

Then the thesis has been organized in seven chapters being the first one this introduction:

- Chapter 2: presents the main properties of both ZnO and MgO materials as well as a brief description of the growth methods that have been employed to achieve its alloy. It provides also the growth conditions used in each of one.

- Chapter 3: describes the characterization techniques employed to check the morphological, optical and structural properties of our experimental results.

- Chapter 4: the findings on highly ordered ZnO and $Zn_{1-x}Mg_xO$ nanowires on patterned polycrystalline pellets are presented, beginning with the initial growth of randomly oriented $Zn_{1-x}Mg_xO$ nanowires.

- Chapter 5: discusses the growth and the properties of homoepitaxial *m*-oriented microcavities using ZnO as active media and $Zn_{1-x}Mg_xO$/ZnO multilayer system as bottom and top mirrors.

- Chapter 6: with the aim of future developing of homoepitaxial *r*-oriented microcavities, this chapter illustrates the growth and properties of epitaxial *r*-oriented $Zn_{1-x}Mg_xO$ single layers on ZnO substrates. This low-symmetry material system exhibit an strange and poorly known phenomenon related with Multiple X-Ray Diffraction. The possibilities brought about this phenomenon from a structural characterization point of view are also studied.

- Chapter 7: summarizes the most important conclusions arisen from our study.

Finally, after the conclusion chapter, an appendix section that lists some additional information and a spanish summary of this thesis has been included.

Chapter 2

Materials and growth methods

As was stated in the previous chapter, the interest in the ZnO-MgO alloy and in the different methods to growth $Zn_{1-x}Mg_xO$ structures is highly increasing. As we were interested on the obtainment of nanowires by an easily and low cost way and also on the attainment of high quality heterostructures, Vapor-Solid and Molecular Beam Epitaxy growth methods were employed respectively. This chapter provides an insight into the main properties of the ZnO and MgO materials and into some concepts about the crystalline growth methods used in this thesis to obtain its alloy, affording also the employed growth conditions.

2.1 ZnO properties

ZnO is a semiconductor of II-VI family with a direct band gap of 3.36 eV at room temperature making it interesting for ultaraviolet optoelectronic devices. Its most thermodynamic stable phase is the wurtzite structure, although it is also possible to obtain ZnO in other crystalline structures, such as rocksalt (which may be obtained at relatively high pressures) or zincblende (which can be stabilized only by growth on cubic substrates) [62]. ZnO wurtzite structure can

be considered to be composed of two interpenetrating hexagonal close-packed (hcp) sublattices displaced along the c-direction by the internal parameter u, which is 3/8c in an ideal wurtzite structure. The lattice parameters were investigated for many decades and in general they are comprised in the ranges a=3.2475 − 3.2501 Å and c=5.2042 − 5.2075 Å [1]. In the ideal wurtzite structure, characterized by equal bond lengths, c/a is $\sqrt{8/3} = 1.63$. However, for ZnO c/a is slightly lower since O-Zn bound distance is 1.992 Å in the direction parallel to the c-axis and 1.973 Å in the other three directions [63]. Due to the low crystalline symmetry of the wurtzite hexagonal structure combined with the electronegativity difference between the Zn and O atoms, there is a spontaneous polarization along the c-axis. Because of that this direction is usually called polar direction and c-plane is referred as polar plane. On the contrary, along the directions perpendicular to the c-axis, the positive and negative charge distributions are symmetric so these directions do not have spontaneous polarization. The nonpolar planes mostly used are a- and m-plane. The semipolar r-plane is also object of interest due to the reduction of the undesired internal electric field that takes place in this direction. In Figure 2.1(a) a sketch of the ZnO structure is shown, where their most meaningful planes are indicated. In this thesis the four indices Miller-Bravais notation (hkil) has been employed, and in some cases, in order to lighten the reading, the contracted notation [64] using a dot instead the i has been used.

Regarding the optical properties, ZnO is a direct-bandgap semiconductor. Its electronic band structure is depicted in Figure 2.1(b) where the valence band can be seen split into three valence bands (A, B, C) as a consequence of the crystal field and the spin-orbit splitting. The bandgap energy of bulk ZnO at room temperature is ~ 3.36 eV. Their radiative transitions in the energy range of the visible spectrum can be categorized as two types: near band edge transitions (2.95 − 3.37 eV) and transitions related to deep levels within the bandgap (1.5 − 2.95 eV). The former, in addition with the band to band transition itself, covers the luminescence related with free and bounded excitonic transitions, their corresponding replicas and transitions related with donors, acceptors and shallow defects. The later, also referred as deep level

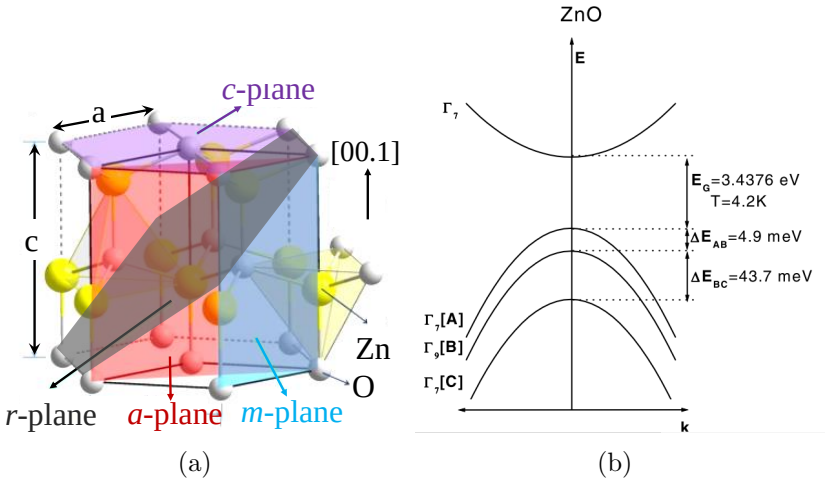

Figure 2.1: a) Three dimensional representation of the ZnO wurtzite structure, original image taken from wikipedia and b) band structure and symmetries of hexagonal ZnO, image taken from [65].

band, green band and defect band, is attributed to donors, acceptors and defects too. These different transitions are briefly explained below.

The electrons and holes are attracted by Coulomb forces and can give rise to a new type of quasi particle, the exciton. When this electron-hole pair recombines it produces a very narrow emission with a maximum of energy that is given by the following expression:

$$E_{EX} = E_g(T) - E_b \tag{2.1}$$

$E_g(T)$ is the temperature dependent bandgap which follows the Varshni's law:

$$E_g(T) = E_g(0) - \frac{\alpha T^2}{T + \beta} \tag{2.2}$$

where $E_g(0)$ is the bandgap energy at 0 K, T is the temperature, and α and β are the temperature coefficients.

E_b is the exciton binding energy, which is quantified and can be approximated using the model for the hydrogen atom as:

$$E_b = \frac{\mu e^4}{2\hbar^2(4\pi\epsilon n)^2} \tag{2.3}$$

where μ is the reduced mass of the system, e the electron charge, $\hbar$ the reduced Plank constant, ϵ the ZnO permittivity and n is the principle quantum number. In wide bandgap semiconductors as ZnO this energy is relatively high ($\sim$ 60 meV) if we compare with the thermal energy at room temperature ($\sim$ 25 meV), making possible to observe this type of transitions even at room temperature. The holes of the three valence band A, B and C can give rise to excitons. One of the first studies reported about excitonic transitions in ZnO was performed by Thomas in 1960 [66] by absorption and reflectance measurements at low temperature. There are many studies in which, using different techniques, slightly different values for these transitions are obtained. This discrepancy is due to the difficulty in the interpretation of the reflection spectra which are highly complex near the absorption edge. A and B excitons interact mainly with light polarized perpendicular to the c-axis, while C excitons mainly interact with light parallel to the c-axis. Their optical transition energies measured by photoluminescence and reflectivity measurements at 2K by Reynolds *et al.* [67] are 3.377, 3.394 and 3.433 eV for A, B and C free excitons respectively.

In materials with defects or impurities such as donors, acceptors and even ionized donors and ionized acceptors, the excitons can be bound to them by means of Van der Waals forces. This bounding reduces the energy of the free exciton therefore these transitions are located at lower energies than the free excitons ones. The origin of most of these transitions is uncertain, however for ZnO some of them have been identified and reported on ref. [65], as transitions due to hydrogen atoms (3.3628 eV), aluminum (3.3608 eV), gallium (3.3598 eV) or indium (3.3567 eV). When increasing the temperature, bound excitons get ionized due to thermal activation and free excitons dominate the emission spectra.

When the semiconductor effective thermal energy is higher than the excitonic one or when there is enough free charge in the semiconductor to dissociate the excitons by screening the coulombian interaction, the electrons and holes are free in their corresponding bands. They can

recombine radiatively emitting a photon with an energy that depends on the temperature and the excitation power. Therefore, at low temperatures and low excitation powers, the energy of the emitted photon is equal to that of the bandgap of the semiconductor. These transitions are called band to band recombination.

Sometimes, optical transitions entail the creation of phonons. In single crystal wurtzite ZnO there are four atoms per unit cell giving rise to 12 phonon modes: one longitudinal-acoustic (LA), two transverse-acoustic (TA), three longitudinal-optical (LO), and six transverse- optical (TO) branches. In particular, there is a LO-phonon band with an energy of E_{LO}=72 meV, which might interact strongly with excitons giving rise to different kind of replicas [65].

The impurities and defects present in the sample can introduce levels in the semiconductor that in turn produce radiative transitions as already commented. The ZnO native defects (imperfections in the crystal lattice that involve only the constituent elements) are oxygen vacancies (V_O), zinc vacancies (V_{Zn}), oxygen interstitial (O_i), zinc interstitial (Zn_i), oxygen anti-sites (O_{Zn}), zinc anti-sites (Zn_O) and clusters formed by the combination of two point defects as e.g. V_OZn_i cluster situated 2.16 eV below the conduction band minimum [68]. In Figure 2.2 a scheme of the native point defect levels in ZnO is shown, where this kind of transitions is exemplified.

Finally, the so-called donor-acceptor pairs (DAP) are given between the electrons of a donor level and the holes of an acceptor level. A DAP transition around 3.22 eV in bulk ZnO has been reported, although the chemical identity of the acceptor was unknown [65].

2.2 ZnO-MgO alloy properties

Although MgO is usually considered as a wide bandgap semiconductor, it is close to an ideal insulating ionic solid [70]. Its broad direct bandgap of 7.7 eV makes MgO a suitable candidate for bandgap engineering in the ZnO-MgO alloy system, which may provide an optically tunable family of wide band gap materials that can be used in various UV applications. The structure of MgO, which is depicted in Figure

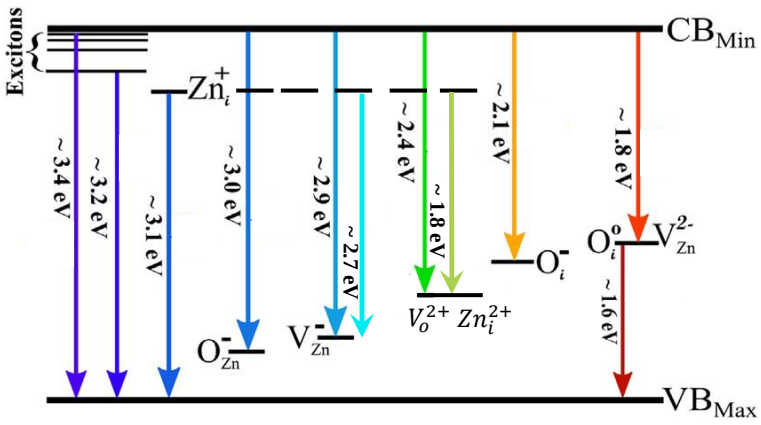

Figure 2.2: Sketch of some of the inter-band transitions in ZnO. Original image taken from [69]

2.3, can be described as two face centered cubic (fcc) sublattices displaced relative to one another by $1/2a$, where a is the lattice parameter $a = 4.211$ Å [70].

The difference in the crystal structures between ZnO and MgO limits the maximum Mg content that can be incorporated into the hexagonal structure of ZnO, causing the phenomenon of phase separation to appear at a certain concentration. This limit depends on the employed growth method and growth conditions. The experimental data for the evolution of the $Zn_{1-x}Mg_xO$ bandgap and lattice parameters with the amount of incorporated Mg varies considerably in the literature. As an example, figure 2.4(a) shows the values of the bandgap energy at 4.2K and at room temperature (RT) extracted from absorption and photoluminescence measurements as a function of the Mg concentration. The samples of the example consist in biaxially compressive strained $Zn_{1-x}Mg_xO$ epitaxial films, grown by plasma-assisted molecular beam epitaxy on a-plane sapphire substrates [43]. Figure 2.4(b) shows the typical variation of the wurtzite lattice parameters as a function of the Mg content of such films, with an increasing lattice parameter a and a decreasing lattice parameter c with increasing Mg concentration.

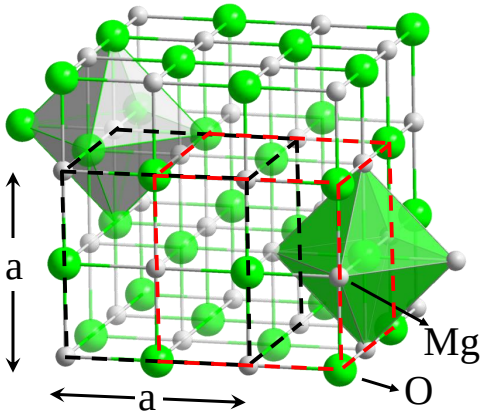

Figure 2.3: Three dimensional representation of the MgO rock-salt structure, original image taken from wikipedia.

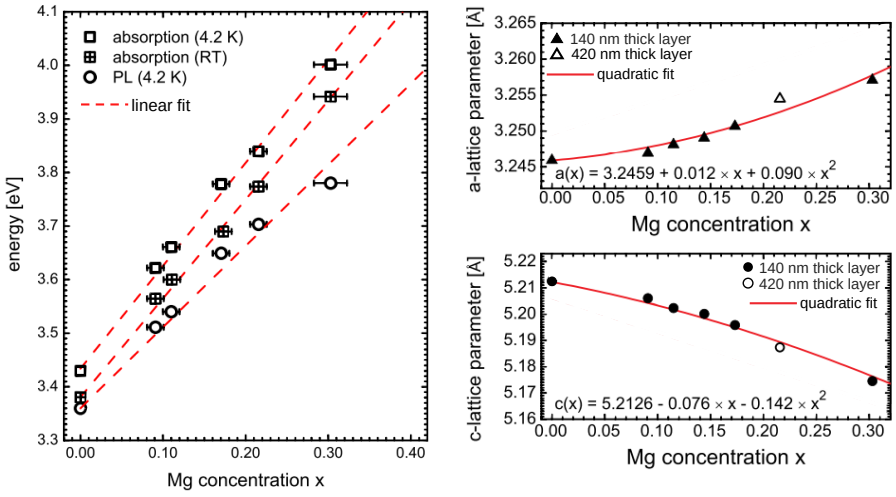

(a) (b)

Figure 2.4: a) Dependence on the Mg concentration of the PL peak energy at 4.2K and bandgap determined by absorption measurements at 4.2K and at RT, and b) dependence of the *a*- and *c*- lattice parameters on the Mg concentration, original images taken from [43].

When the geometrical ordering of the atoms is not symmetrical with respect to the crystalline axes of the material, the electromagnetic waves passing through the crystal can experience different refractive index, depending upon the direction of propagation. In the case of ZnO-MgO alloys this anisotropy results in an uniaxial birefringence, that is, there is a single direction governing the optical anisotropy whereas all directions perpendicular to it are optically equivalent. Thus rotating the material around this axis does not change its optical behavior. This special direction is known as the optic axis of the material and in the case of the ZnO it is the *c*-axis. Waves whose polarization is perpendicular to the *c*-axis are governed by a refractive index called ordinary (n_o) whilst waves whose polarization is parallel to the *c*-axis sees an optical index known as extraordinary (n_e) (see Figure 2.5(a)). The magnitude of the difference is quantified by the birefringence: $\Delta n = n_e - n_o$ and it is positive for both ZnO and $Zn_{1-x}Mg_xO$. The measured ordinary and extraordinary refractive index of $Zn_{1-x}Mg_xO$ epitaxial films, grown by pulsed laser deposition on *c*-plane sapphire substrates [36] are depicted in Figure 2.5(b).

These dependencies provide an important information for the design and modeling of ZnO/MgZnO heterostructure optoelectronic devices.

2.3 Vapor-Solid growth method

Crystal growth methods which run from the vapor phase can take place in both closed and open systems. All of them are based on the gas phase transport of the material from the evaporation zone to an area named crystallization zone, in which vapor to solid phase transition is produced. This transport is governed by convection and diffusion processes in the case of closed systems or by the use of a transport gas in the case of open systems. Then the crystallization of the material can be produced with or without catalysis. As said in the introduction chapter, ZnO nanowires (NWs) can be obtained in a huge variety of ways [71]. Vapor-Solid (VS) method is determined by direct condensation from vapor phase so that the contamination caused by the use

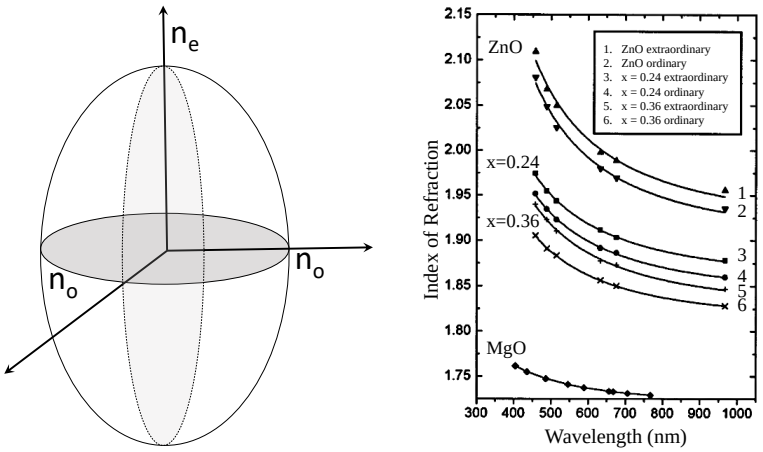

(a) (b)

Figure 2.5: a) Refraction index ellipsoid and b) ordinary and extraordinary refractive index of $Zn_{1-x}Mg_xO$ films for ZnO, x=0.24, and x=0.36. The solid curves are least-square fit to the first-order Sellmeier dispersion relationships, image taken from [36].

of a catalyst is avoided. Parameters as pressure, ambient, temperature and employed substrate will define the final morphology and size of the obtained nanostructures [72]. During this thesis randomly and self arranged $Zn_{1-x}Mg_xO$ NWs were achieved using a one-zone horizontal tube furnace, at the University Complutense of Madrid. A scheme of the VS system can be seen in Figure 2.6(a). All the growths were performed at atmospheric pressure, at 900 °C during different growing times and using 1.5 slm argon flow as carrier gas. A sketch of the thermal treatment and the temperature profile inside of the furnace are shown in Figure 2.6(b) and (c) respectively.

The precursors materials were milled in a centrifugal Retsch S100 ball mill during different times. Subsequently a compressive load of 1 ton was employed to make pellets in the form of disks with a diameter of 7 mm and 2 mm thickness. The growing conditions for randomly and self arranged NWs were different and will be explained separately.

In the case of randomly oriented NWs the configuration shown in Figure 2.6(d) was employed. In this setup one only pellet acted both

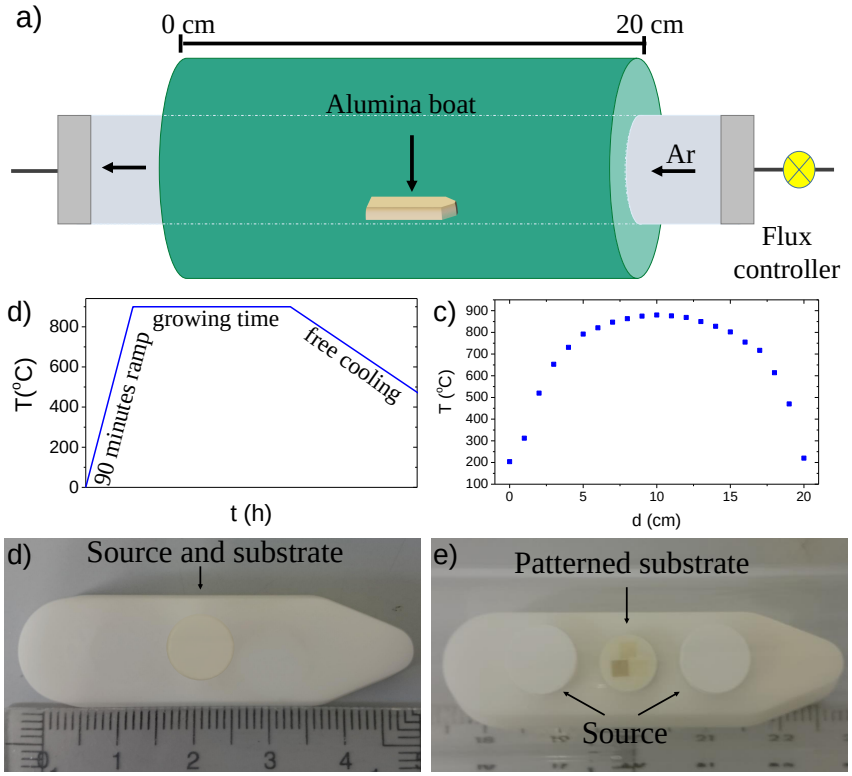

Figure 2.6: Configuration employed for both randomly and self arranged nanowires growth. a) Sketch of the horizontal tube furnace system, b) scheme of the used thermal treatments c) temperature profile inside of the oven, d) configuration for randomly NWs and e) configuration for self arranged NWs.

Laser parameters	
λ (nm)	1030
Spot radius (μm)	19.44
Line separation (μm)	15
FWHM pulse duration (fs)	350

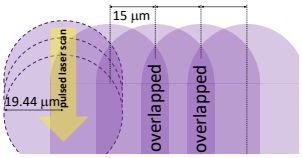

Table 2.1: Main laser parameters employed for obtaining LIPSS.

as source and substrate, that is, NWs grow on the source surface itself. The used configuration for the growth of self arranged NWs is shown in Figure 2.6(e). In this setup two source samples were placed at both sides of a patterned pellet which acted as substrate. Pellets were 900 °C air annealed before of been patterned in order to enhance the particle cohesion.

Patterned substrates were obtained by irradiation with ultra short laser pulses, that produced Laser Induced Periodic Surface Structures (LIPSS). The irradiation was carried out by the Laser Processing Group, at the Optic's institute of the Spanish National Research Council in Madrid (Spain) (known in spanish as CSIC). Irradiations were performed using a scanned femtosecond Yb doped fiber laser from Amplitude Systems (the details of this irradiation setup can be found elsewhere [73,74]). The operating central wavelength was 1030 nm, with a pulse duration of 350 fs (FWHM). The spot laser had a radius of 19.44 μm and the line separation was 15 μm, thus producing an overlapping between consecutive lines. The main laser parameters are summarized in Table 2.1 in which inset, a sketch of the commented overlapping is depicted. The irradiation strategy consisted in the formation of homogeneously irradiated areas by means of a high pulse overlapping along each irradiated line, covering in this way all the area of interest.

2.4 Molecular beam epitaxy

In the case of epitaxial layers growth, several methods as Molecular Beam Epitaxy, Metalorganic Chemical Vapour Deposition, Pulsed Laser Deposition... are close to obtain the ideal layer growth condition which consists of the deposition of the material atom by atom (or molecule by molecule) so that the growth takes place layer by layer. The layer properties and their quality are determined by growth factors as environmental conditions, deposition rate, purity of the material to be deposited, substrate temperature... As it has been commented, the large miscibility gap found between MgO and ZnO under thermal equilibrium limits the maximum Mg content achievable by chemical deposition techniques. This can be partially overcome by using molecular beam epitaxy (MBE), since the growth by MBE can be set far from the thermodynamic equilibrium conditions. In addition the elemental fluxes can be controlled independently and MBE allows in-situ monitoring techniques to control the growth, as reflection high-energy electron diffraction (RHEED). In this technique an electron beam generated by the electron gun impinges on the sample with a very small angle relative to the sample surface. The electrons diffracted by the atoms at the sample surface undergo constructive interferences and form regular patterns on the RHEED screen. The resulting pattern provides important information of the sample surface as it is directly related to the arrangement of surface atoms. In the case of two-dimensional (2D) growth, where the sample surface is atomically flat, the electrons are diffracted by a planar atomic array that results in streaky RHEED patterns. On the contrary, if the surface is three-dimensional (3D), the electrons are diffracted into different angles resulting in spotty RHEED patterns.

The growth process is performed under ultra high vacuum conditions by the reaction of one or more atomic or molecular beams on a monocrystalline substrate which is kept at a suitable temperature. There is therefore no transport gas for the reactive species. These conditions allow the atoms/molecules to have a mean free path much greater than the distance sources-substrate. Most of the source materials (Zn and Mg in this thesis) are contained in heated containers

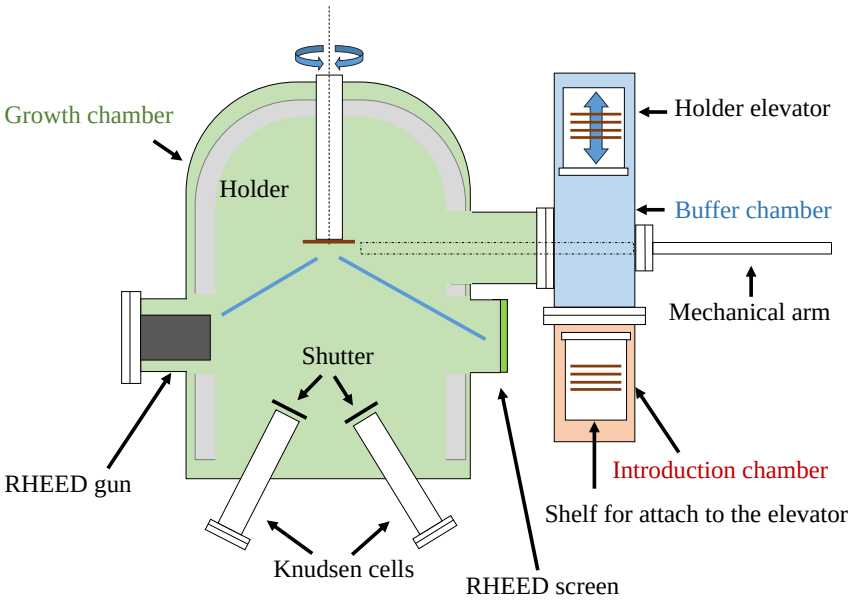

Figure 2.7: Molecular beam epitaxy system sketch.

named Knudsen cells. The flux of each beam is controlled through the temperature of each Knudsen cell, and can be turned open and close by using electronically controlled shutters. In the case of oxygen source, a radio-frequency plasma cell combined with a mass-flow controller is used.

The substrate is mounted in a holder which can be heated and continuously rotated to improve the growth homogeneity. Throughout the growth, liquid nitrogen is continuously flowing in order to keep the unincorporated/unpumped material stuck to the cooled chamber walls.

All the $Zn_{1-x}Mg_xO$/ZnO heterostructures analyzed in this dissertation were grown in a Riber Epineat MBE system at CRHEA-CNRS (Valbonne, France), in Figure 2.7 a sketch of it is shown. The growth system consists in three separately pumped chambers. A holder with the substrate is conducted through the introduction chamber, leaving it in a shelf that can been attached to an elevator. The lift transports

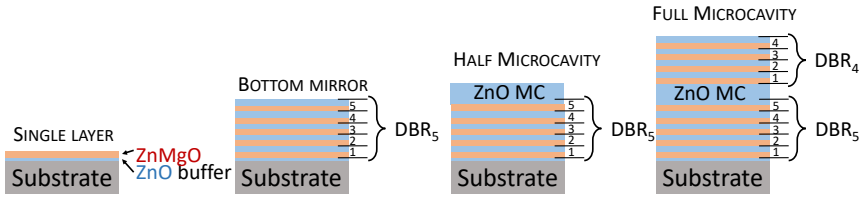

Figure 2.8: Sketch of the microcavity grown process.

the shelf with the holder to the buffer chamber where a mechanical arm takes the holder and leaves it on the growth chamber.

Heterostructures were epitaxily grown on a buffer layer of ZnO grown itself homoepitaxially on commercial 10×20 mm^2 nonpolar $(10\bar{1}0)$ and semipolar $(01\bar{1}2)$ ZnO substrates purchased from Crystec. Samples were grown at a growth temperature of around 400°C. Before introducing the ZnO substrates into the reactor they were annealed at high temperature (1100°C) in an oxygen atmosphere in order to smooth the surface.

These complex heterostructures were fabricated by sandwiching a ZnO layer between two mirrors named distributed Bragg reflectors (DBRs). This mirror consists in a set of $Zn_{1-x}Mg_xO$/ZnO multilayers. Depending on the quantity of grown layers, heterostructures are referred as single layer, bottom mirror, half microcavity and full microcavity as depicted in Figure 2.8, where the complete microcavity (MC) grown process is shown. The microcavities were designed to be in the weak-coupling regime (working at λ of 410 nm, i.e., 40 nm below the exciton resonance). In this respect the cavity consisted in a ZnO λ-thick layer while the layers belonging to the mirrors were $\lambda/4$-thick.

In the case of nonpolar samples it was possible to arrive until the complete MC process so several MCs with different number of bilayers were grown and characterized. However, in the case of semipolar samples, it was not possible to finish the study when this thesis was ending so different $Zn_{1-x}Mg_xO$ single layers were obtained and characterized.

Chapter 3

Characterization techniques

For the obtainment of the required quality structures not only is necessary to control the growth mechanism but also to be able to enhance the growth conditions. In this way growth and characterization constitute a self-reinforcing cycle. For a complete understanding of quality structures it is necessary a morphologic, optical and structural characterization, so that, this chapter aims to give an overview of the techniques that have been employed during this Ph.D. for characterizing the obtained samples.

3.1 Atomic force microscope

Atomic force microscope (AFM) allows the nanoscale morphological study of material surface. The operating principle is based on the attractive and repulsive forces between the sample surface and a very sharp tip attached to a cantilever. In the tapping mode, which used during this thesis for characterizing the samples, a piezoelectric cantilever oscillates at, or near, its resonance frequency while it scans the sample surface. When a change in the surface topography is present, the cantilever is deflected in order to assure that its oscillation amplitude remains constant. These deflections are registered by a photo diode detector through a laser beam reflected on the cantilever surface [75]. In Figure 3.1 a sketch of the microscope can be seen.

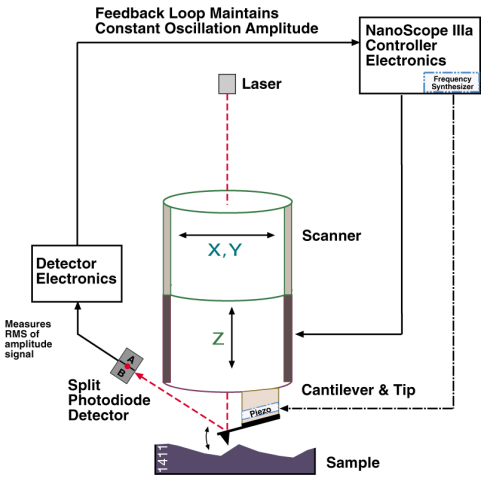

Figure 3.1: Sketch of an AFM taken from instrument instructions book.

The software provided with the microscope is able to make processing operations with the AFM images. The most widely used processing step applied to AFM data is the leveling, which aim is to correct the substrate tilt, since AFM images usually measure absolute sample height. A very common method for leveling AFM images is by polynomial fitting. Each line in the image is fitted to a polynomial equation. Then, the polynomial shape is subtracted from each scan line, leading them flattened. Once the data have been processed, and the surface topography function h(x,y) obtained, the most commonly used parameter for evaluate the surface quality is the Root Mean Square (RMS) roughness:

$$RSMroughness = \sqrt{\sum_{i=1}^{I}\sum_{j=1}^{J}[h(i,j) - \bar{h}]^2} \tag{3.1}$$

where the summations are performed over all the image pixels (i,j) of the scanned area and $\bar{h}$ is the mean height.

The AFM images of this manuscript were taken at CHREA-CNRS with a VEECO (Bruker) Nanoscope IV Dimension 3100.

3.2 Scanning electron microscopy

The scanning electron microscopy (SEM) uses a focused high-energy electron beam to reveal information about the sample as their morphology, chemical composition, crystalline structure and orientation. The electron gun generates an accelerated electron beam with energies in the range $1-40$ keV. Then the beam goes through several electromagnetic lenses which focuses the electron beam with the desired crossover diameter on the specimen. From the electron-sample interaction different signals are arisen: electrons, photons, X-rays... (Figure 3.2). The interaction volume increases with increasing incident beam energy and decreases with increasing average atomic number.

The information about the morphology and the surface topography is provided by the secondary electrons (SE) and by the back scattered electrons (BSE) signal. SE are low energy electrons emitted by the inelastic interaction between the incident electrons and the outer electrons of the atoms. Because of their low energy, SE can only escape from the sample if they are generated close to the surface. BSE are high energy electrons originated in the electron beam, which are reflected or back-scattered out of the sample due to elastic scattering interactions with the specimen atoms. BSE can provide also compositional information since the signal generated from regions with different composition is proportional to the difference in the average atomic number.

During this work the following SEMs have been used: Hitachi S-2500, Leica 440 Stereoscan, Fei Inspect (at the Complutense University of Madrid, UCM, Spain), Jeol JSM-7000F and ZEISS Supra 40 (at CRHEA-CNRS in Valbonne, France) and Hitachi S-4800 (at the university of Valencia, Spain).

3.2.1 Energy dispersive X-ray spectroscopy

Characteristic X-rays arise by inelastic collisions of the incident electrons with electrons in discrete orbitals of atoms in the sample. As the excited electrons return to lower energy states, they yield X-rays of a fixed wavelength that are characteristic for each element. These X-rays can be used to identify the elements present and establish their

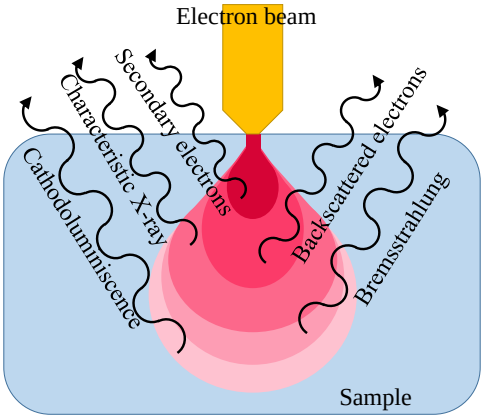

Figure 3.2: Interaction volume of an electron beam in its interaction with the sample.

concentration. The X-ray spectrum is composed of a series of peaks, characteristic of each element overlapped to a lower intensity continuous background (Bremsstrahlung X-rays). The intensity of the peaks can be represented as a function of its wavelength, (Wavelength Dispersive Spectroscopy, WDS) or as a function of its energy, (Energy Dispersive Spectroscopy, EDS or EDX). In figure 3.3 there is a sketch of the characteristic X-ray production and an example of a typical spectrum measured in one of our samples. Microanalysis was performed with a Bruker AXS Quantax detectors attached to the LEICA 440 SEM at UCM, to the Hitachi S-4800 at University of Valencia and with a SiriusSD detector for measurements taken at CRHEA-CNRS.

3.2.2 Cathodoluminescence

Cathodoluminescence (CL) is the emission of photons of characteristic wavelengths due to the recombination of electron-hole pair generated by the incident electrons. Solid-state luminescence can be divided into two basic types. On the one hand the intrinsic luminescence, which is produced by radiative near band-to-band recombination when an electron from the conduction band directly combines with a hole in the valence band. On the other hand, extrinsic luminescence which

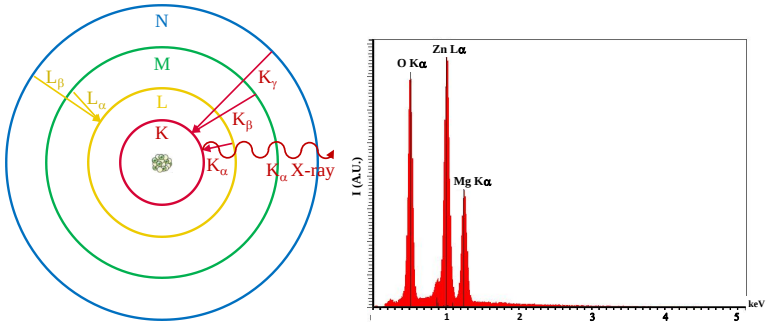

(a) (b)

Figure 3.3: a) Characteristic X-ray production b) EDX spectrum belonging to a $(01\bar{1}2)$ $Zn_{0.57}Mg_{0.43}O/ZnO$ system grown by MBE.

has its origin in lattice defects or impurities and arises when an electron (or hole) is trapped by an energy state in the forbidden region consequence of the defects in the crystal lattice. Two kinds of CL measurements can been done, spectrum measurements and panchromatic images. The former gives information about the bandgap and defect levels in an intensity versus emission wavelength plot, while the later provides information about the spatial distribution of luminescent centers. In these images the whole of the emitted spectrum in each point is detected and displayed.

CL measurements were performed at UCM in a LEICA 440 and in a Hitachi S2500 SEM. To record the CL images a Hamamatsu R928 photomultiplier was used, while in the case of CL spectra, a CCD Hamamatsu PMA 11 with built in spectrograph was employed.

3.3 Photoluminiscence

Photoluminiscence (PL) is the emission of photons of characteristic wavelengths due to the recombination of electron-hole pair generated by an incident photon beam with an energy larger than the bandgap energy. As well as CL, PL provides information about the material bandgap and also about the defect levels that could been throughout it.

While electrons in CL usually excites the greatest number of radiative transitions, PL is more selective since it depends on the energy of the exciting photons.

μ-PL measurements have been done at UCM with a confocal microscope Horiba Jobin-Yvon LabRam HR800 with micrometer spatial resolution. All the spectrum were generated by a UV He-Cd laser (λ = 325 nm) and registered by a CCD Synapse 354308. The employed diffraction grating was 600 lines/mm. All the measurements were done at room temperature.

3.4 X-Ray diffraction

X-Ray diffraction (XRD) is a technique to study the structure of crystalline materials. Diffraction effects can be observed when electromagnetic radiation of wavelength λ impinges on a periodic structure which has geometric variations in the same order of magnitude. The geometric constraint for constructive interference is that the path followed by the different rays must differ by an integer number of wavelengths (λ). This phenomenon is described by the Bragg's law through the equation:

$$2dsin\theta = n\lambda \tag{3.2}$$

where d is the interplanar distance, θ is the Bragg angle, n is the diffraction order and λ the used wavelength.

All the XRD measurements during this thesis have been made with a high resolution diffractometer, which allows to perform measurements beyond the typical $2\theta/\omega$ scans. Their main characteristics are that it employs a parallel beam (unlike the divergent beam used in typical powder diffractometers), it is equipped with a four-axis goniometer and it is able to make accurate movements in the three spatial directions (x, y, z) as well as spin around three different axis (ω, φ, χ).

High resolution X-Ray diffraction (HRXRD) measurements were taken in a Panalytical X-Pert MRD diffractometer with Cu tube at the Central Support Service for Experimental Research, known in local language by their initials SCSIE, (Valencia, Spain) and also at

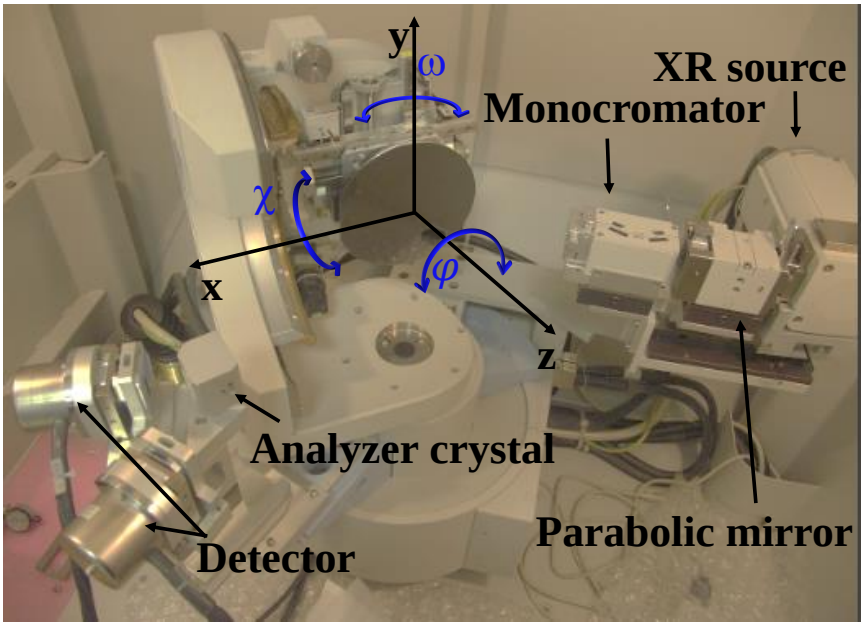

Figure 3.4: HRXRD system

CRHEA-CNRS (Valbonne, France). Parallel Kα_1 irradiation was ensured by a parabolic mirror and a 4-bounce hybrid monochromator situated in the incident beam. A three-bounce (220) Ge analyzer crystal was placed in the diffracted beam. The X-ray beam divergences were 0.005° in the incidence plane and 2° in the axial direction. A picture of this kind of diffractometer is shown in Figure 3.4.

Chapter 4

$Zn_{1-x}Mg_xO$ nanowires

This chapter illustrates the growth and the morphological, optical and structural characterization of self arranged $Zn_{1-x}Mg_xO$ nanowires (NWs) grown by Vapor-Solid method using polycrystalline patterned pellets as substrates. The properties of these patterned pellets are also analyzed in detail. As previously said, parameters as pressure, ambient, temperature and employed substrate will define the final morphology and size of the obtained nanostructures [72]. In this respect, previously to the study of the potential use of irradiated areas as growth patterns, the Vapor-Solid (VS) growth process itself is analyzed.

4.1 Randomly growth of $Zn_{1-x}Mg_xO$ NWs

The use of ZnS as a precursor is a good alternative way to grow pure and ZnO based nanostructures since it requires lower growing temperatures and shorter growing times [76–79]. Based on this, different mixtures of ZnS and MgO powders were used as source material, with a purity of 99.99% and 99.9% respectively. The weight proportions of ZnS and MgO were 99:1, 95:5 and 80:20 respectively. With these percentages two set of mixtures were performed, one was milled during 5 hours while the other one during 15 h. We will label the samples according to the weight percentage of Mg content ($1, 5$ or 20) and the milling time (low (set L); high (set H)). Compressed pellets

	Sample	Milling time (h)	wt.% MgO	at.% Mg
Set L	L1	5	1	1.2
	L5	5	5	5.7
	L20	5	20	18.9
Set H	H1	15	1	1.2
	H5	15	5	5.7
	H20	15	20	18.9

Table 4.1: Description of the randomly oriented NWs growth conditions. All the growths were performed at atmospheric pressure, at 900 °C during 5 hours and using 1.5 slm argon flow as carrier gas.

and thermal treatments were performed as described in Chapter 2 and details of the growth conditions can be seen in Table 4.1. Pure ZnO NWs were also grown for comparison.

As said, the used setup consisted in a single pellet which acted both as source and substrate. NWs growth takes place on the surface of the pellet. Regarding the morphology, after the growth all the pellets belonging to set L were absolutely covered by long nanowires whilst samples belonging to set H exhibited a negligible amount of NWs. Figure 4.1(a) shows a representative image of samples from set L. The samples consisted of randomly oriented NWs totally covering the pellet surface, with thickness between 50 and 150 nm and some stepped NWs clumps. These two kinds of NWs are shown in more detail in Figures 4.1 (b) and 4.1 (c). NWs belonging to the clumps were about 40 μm long and between 150 and 780 nm thick. The number of clumps and the length of NWs raised as the Mg content in the original mixture increased. In Figure 4.1(d) a representative image of samples belonging to set H is shown. These samples presented a very rough surface without NWs, although in some areas, mostly in pellet borders, a low density of nanowires was observed. Because of this, samples of set H were dismissed for subsequent studies, which was developed only for samples L.

Magnesium content in 5h milled set was investigated via Energy Dispersive Spectroscopy (EDX). No evidence of impurities, such as S coming from ZnS, was observed in the patterns, suggesting that ZnS

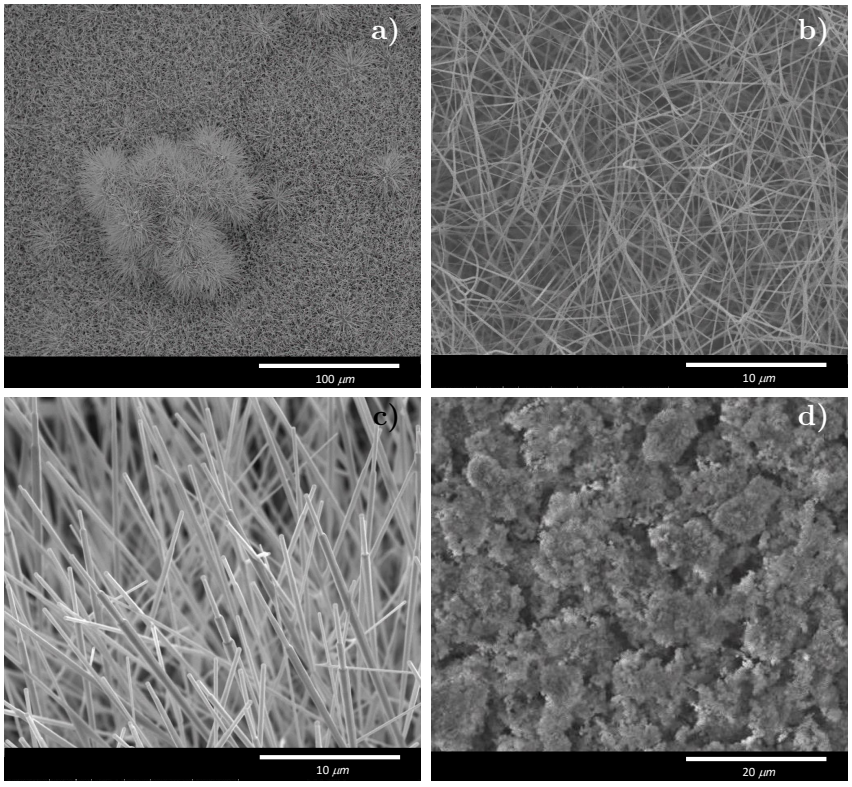

Figure 4.1: SEM images of the random NWs growth: a) Representative picture for the set of samples L, b) detail of randomly oriented NWs, c) detail of stepped NWs belonging to the clumps and d) representative image for the set of samples H.

has been oxidized into ZnO, as can be seen in Figure 4.2(a) which shows a 15 KV EDX spectrum for L20 sample. The measured Mg content was 7.2 Mg at. % for this sample. In the case of L5 this content was near the limit of resolution ($\sim$ 1% at.), being homogeneously distributed over the exposed surfaces (Figure 4.2(b)). Finally, for L1 sample no Mg was detected. Because of this, L1 samples, were dismissed for subsequent studies.

Regarding the structural properties, X ray diffraction (XRD) was performed on samples L5 and L20. Results are shown in Figure 4.2(c). Typical diffraction peaks of ZnO and MgO can be appreciated (ICDD No. 36−1451 and No.00−004−0829 respectively) in sample L20, while for sample L5 only peaks corresponding to ZnO were found. With respect to the crystallographic orientation, the most intense peak of ZnO corresponds to the (0002) plane, indicating a slight preferential orientation of NWs along the wurtzite c-axis.

About the optical properties, in order to exclude any contribution from the underlying pellet and to investigate the luminescence properties of the individual nanowires, μPL measurements were performed on scratched nanowires which were transferred to a clean Si substrate. Results are shown in Figure 4.2(d) where ZnO NWs luminescence is also shown as reference (black line).

All samples show a predominant emission corresponding to the near band-edge emission (NBE). For both pure and L5 samples NBE is centered at 3.26 eV while for L20 is centered at 3.29 eV. A narrowing of this band is appreciated in the L20 spectrum (red line), so the addition of MgO to the precursors suggests a reduction of the components associated to recombination via shallow levels. Regarding the deep level (DL) band, peaked at 2.37 eV and typically attributed to several intrinsic point defects such as oxygen vacancies (V_o) among others [1,68,80], there is a notorious decrease in the intensity relative to the NBE for doped samples. This could be associated to the extra oxygen supply of using MgO as precursor instead of elemental Mg.

Summarizing, 15h milled mixtures produced non covered and non homogeneous samples, while 5h milled ones generated absolutely covered samples, with nanowires having several sizes. EDX measurements reveled that L1 sample had a Mg content below the resolution limit.

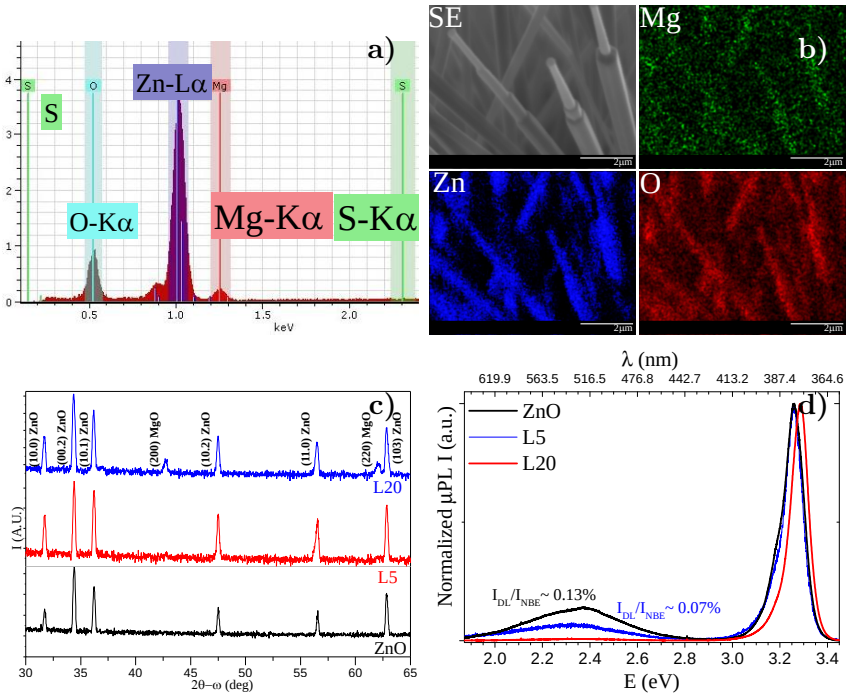

Figure 4.2: a) EDX spectra of 20wt%Mg-5h milled sample b) Compositional mapping of 5wt%-5h milled sample. For both samples: c) XRD spectra and d) μPL spectra at room temperature.

L5 presented a low Mg content but homogeneously distributed over the sample. The luminescent properties were well preserved for all the L set of samples. Despite L20 had better luminescent properties than L5, MgO-phase peaks were detected by XRD in the former and not detected in the latter. Consequently the conditions used in L5 sample were selected to constitute the sources for the growth of self arranged NWs on patterned pellets.

Before studying the potential use of the irradiated areas as 2D patterns for the growth of highly ordered nanowires, patterned pellets properties will be analyzed.

4.2 $Zn_{1-x}Mg_xO$ patterned pellets

Pellets for their use as substrates were produced as described before but using ZnO (with a purity of 99.9%) instead of ZnS in the mixture. In all the patterned pellets the weight proportion of ZnO and MgO was 95 : 5 and the mixtures were milled during 5 hours. As all the samples are performed using the same mixtures, in order to lighten the notation hereinafter $Zn_{1-x}Mg_xO$ will be referred to as ZnMgO. The Mg content will be indicated separately. The irradiation, which conditions are summarized in Table 4.2, was carried out with the femtosecond pulsed laser described in Chapter 2. Three homogeneously irradiated areas of about 2×2 mm^2 using different irradiating conditions were performed, giving rise to three different regimes of total deposited energy on the patterned pellet surface (E1, E2, E3). The rest of the pellet surface constitutes the non irradiated area (NI) which is the fourth region of interest. Pure ZnO patterned pellets were also prepared and irradiated to be used as reference.

4.2.1 Morphological properties before the growth

When a pellet is irradiated, Laser Induced Periodic Surface Structures (LIPSS) arise in form of parallel surface ripples. Ripples are perpendicular to the laser polarization independently of the scanning direction, as commonly observed [81]. In our case this spatial periodi-

350 fs pulser laser parameters λ=1030 nm, r=19.44 μm, Δ=15 μm			
Condition	**E1**	**E2**	**E3**
ν (kHz)	100	10	100
V (mm/s)	194	3.8	19.4
Fluence (J/cm^2)	1	1	2
Pulse E (μJ)	6	6	12
Total E (μJ)	242	1236	4844

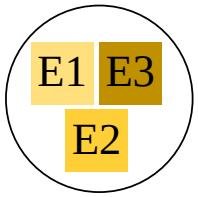

Table 4.2: Main irradiation conditions employed for obtaining LIPSS.

city resulted in the sense of the motion of the laser beam in each scanning line (see Figure 4.3(a)). In the LIPSS literature is usual to classify them into two different groups attending to the ripple spatial period (Λ), which depends on the properties of the material, mainly refractive index and band-gap, as well as on the processing conditions [82, 83]. These two groups are called low spatial frequency LIPSS, with periods of the order of the incident wavelength (λ/n) and high spatial frequency LIPSS, with smaller periods typically (λ/2n), being n the refractive index of the material. In addition to the LIPSS periodicity, other periodicity is generated in each irradiated zone due to the overlapping of the scanning laser lines. In Figure 4.3(a) both kinds of periodicities are illustrated in a sketch of the irradiated area. In Figure 4.3(b) a picture of the scanning lines overlapping, which generates a spatial periodicity of about 15 μm, can be seen for one of our samples.

On each irradiated area, Mg distribution on ZnMgO pellets were almost uniform except for several MgO precipitates which appeared both in irradiated and non irradiated areas. Figure 4.4 shows a mapping of the elements O, Mg and Zn on a ZnMgO irradiated pellet, where distribution along the irradiated area can be seen. The measured Mg content was between 1.2 and 3 at. Mg %.

In Figure 4.5 SEM images of the three irradiated zones for both pure ZnO and ZnMgO patterned pellets are shown. As expected from

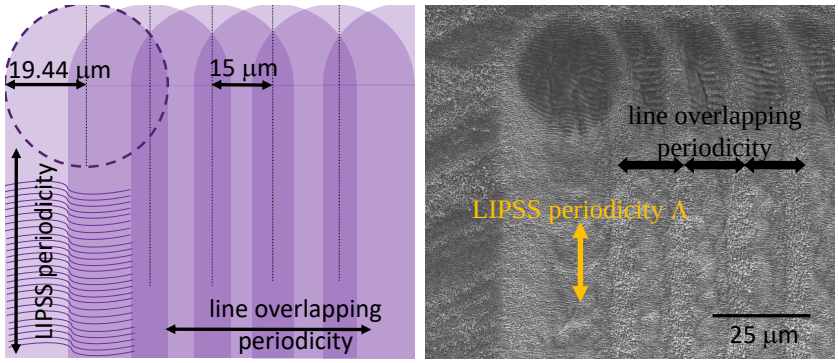

(a) (b)

Figure 4.3: a) Sketch of the irradiated areas showing both kinds of periodicities, one due to the LIPSS formation and the other one due to the line overlapping and b) picture of one of our samples.

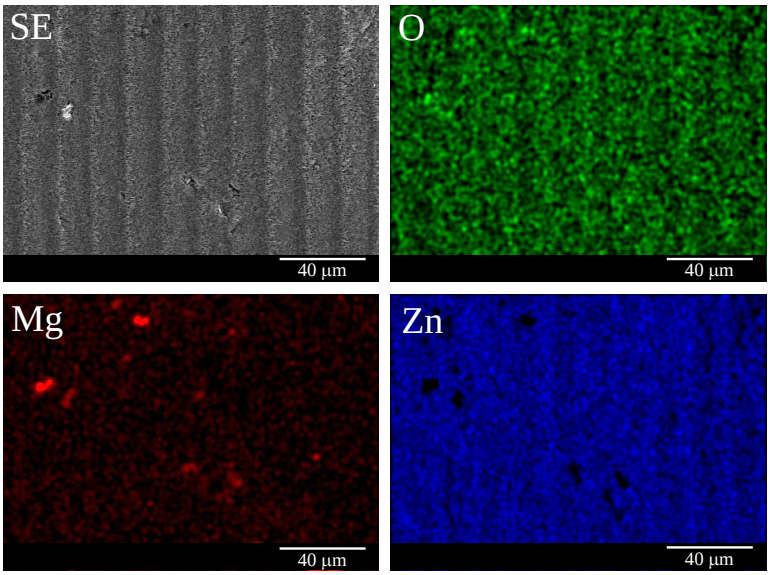

Figure 4.4: Compositional mapping of the irradiated region E2 in a ZnMgO patterned pellet.

the low magnesium content of the samples, negligible differences between pure and Mg doped ZnO pellets were found. In the case of E2 and E3 zones, LIPSS periods are found to be $\Lambda \sim 300$ nm which corresponds quite well with the expected value for high frequency LIPSS for this material ($\lambda/2n$=322 nm) being the ZnO refraction index at laser wavelength 1.6 [84]. In the case of the E1 area, the period for ZnO is around 800 nm, a bit higher than expected for low frequency LIPSS (λ/n=645 nm) but still in agreement with other reported values [30]. The period for ZnMgO in this zone ($\Lambda \sim 710$ nm) is lower than for ZnO probably because LIPSS on Mg doped samples were generally split (see red arrows in Figure 4.5(a1)). This could be associated to the roughness of the ZnMgO pellet before of the irradiation which was higher than in pure ZnO pellets.

Regarding the overlapped areas, the E3 region had redeposited material which was ejected as a consequence of the high pulse dose received during the scanning. For E2 areas this effect was also observed in lower amount. For region E1 the overlapped areas consisted in LIPSS with lower period Λ than in the non overlapped one.

4.2.2 Optical properties before the growth

The luminescent properties of pure ZnO and ZnMgO samples were evaluated through cathodoluminescence measurements. Spectra were measured at 15 KV, on areas of about $20 \times 10\mu m^2$, on the irradiated areas (E1, E2 and E3) as well as on the non irradiated (NI) one. We will use the ZnO spectrum taken on NI area as a reference which is shown in Figure 4.6, where the profile spectrum has been fitted with five gaussian functions following Ref. [69]. The ascription of the different emission bands is also indicated.

On Figure 4.7(a)-(d) spectra for both ZnO (black) and ZnMgO (red) samples taken in each different area are shown. All samples show a predominant emission corresponding to the near band-edge (NBE) around 3.24 eV together with the deep level (DL) band centered around 2.38 eV. In respect to the influence of Mg in the luminescence of the samples, it can be seen that all the different areas present a noteworthy decrease in the DL intensity with respect to the NBE for the ZnMgO

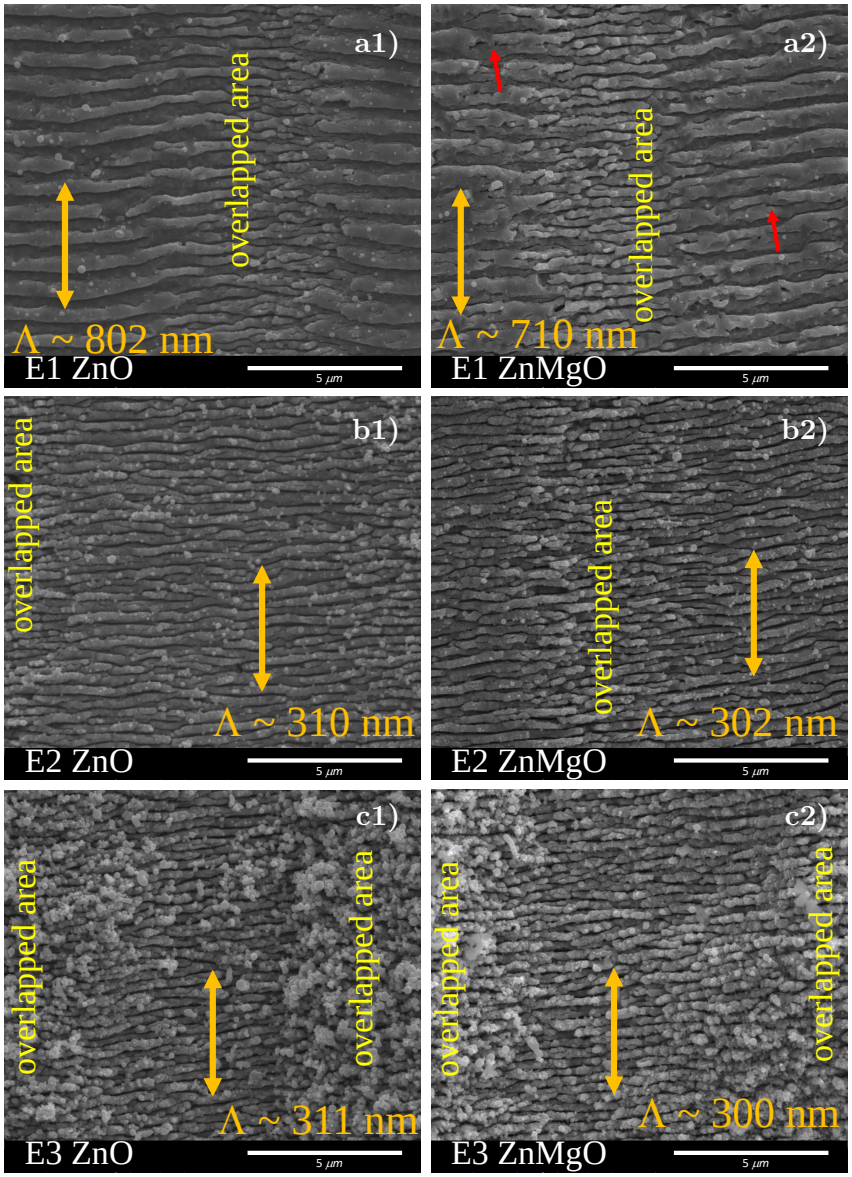

Figure 4.5: SEM images of patterned areas for ZnO and ZnMgO patterned pellets corresponding to the different regimes of total deposited energy a) Lowest value E1, b) medium value E2 and c) highest value E3.

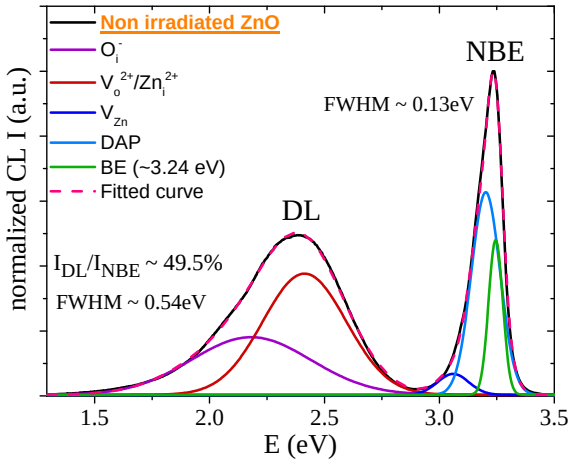

Figure 4.6: Gaussian decomposition of the CL spectrum for the non irradiated area of ZnO.

(red lines) compared with pure ZnO (black lines). Since one of the components of the green band may be ascribed to oxygen vacancies ($\sim$ 2.4 eV), this could be associated to the fact that alloy is made under richer oxygen conditions, when MgO is used instead of elemental Mg.

In Figure 4.7(e)-(f) the combined spectra of all the areas is represented for both ZnO and ZnMgO samples respectively. In respect to the impact of the irradiation conditions on the luminescence properties, while in all irradiated samples the dominant band corresponds to the NBE, and practically no difference is found between them, the situation is completely different for DL band. Comparing with non irradiated area (black), it can be inferred that the relative intensity of the DL increases in the regions with the lowest value of deposited energy (green) while decreases in E2 (blue) and E3 (red). This behavior would point towards an initial increase of defects as a consequence of the irradiation, followed by a recrystallization by an annealing process. In addition, since all the irradiations were performed in air, a major decrease of the component associate to oxygen vacancies would be expected.

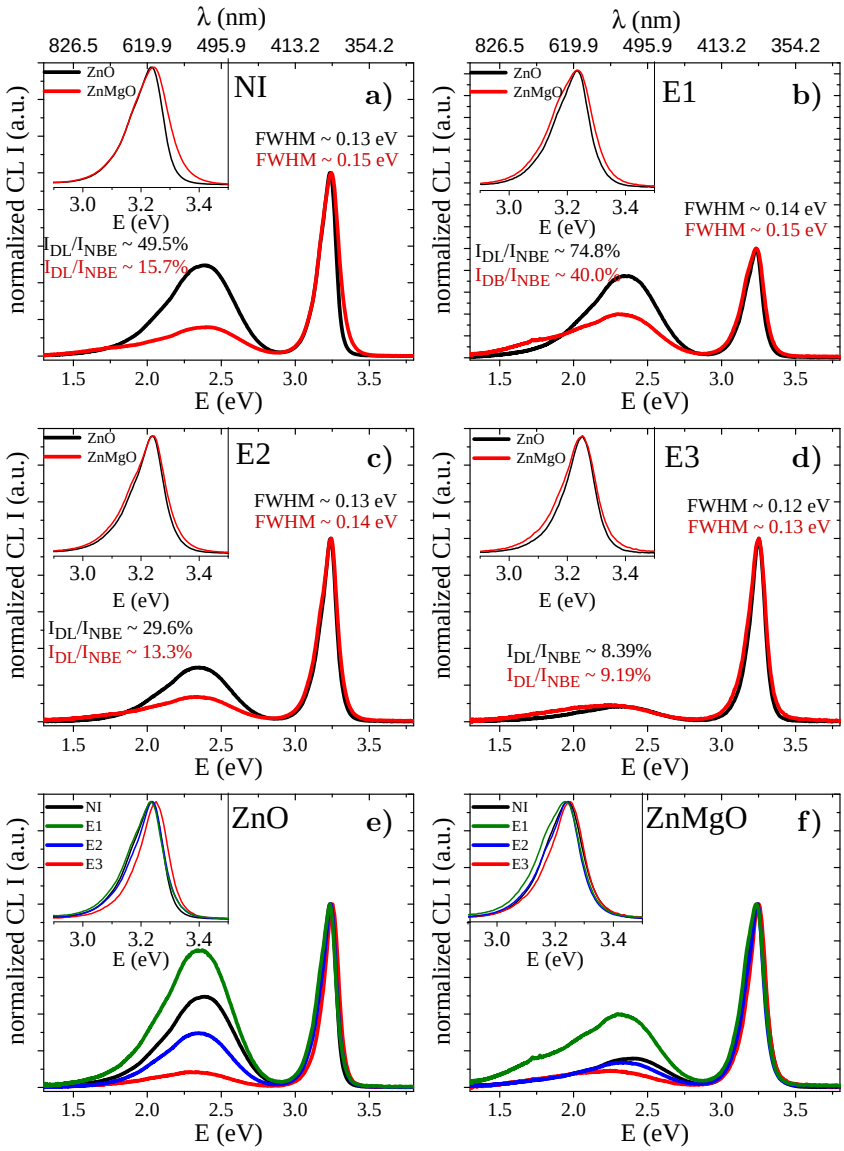

Figure 4.7: CL spectra of both pure and Mg doped ZnO patterned pellets measured on different areas: a) Non irradiated and in the irradiated areas, b) E1, c) E2 and d) E3. Combined CL spectra of all the areas on: e) ZnO and f) ZnMgO.

4.2.3 Structural properties before the growth

In order to investigate if the LIPSS presented any preferential orientation, $2\theta-\omega$/x maps, were done for several different "y" values 1 mm separated between them. The configuration used for making the measurements is shown in Figure 4.8, where the ZnMgO sample is represented as an example for two of these maps. From these maps a and c lattice parameters are calculated obtaining (± 0.0005 Å) $a_{ZnO} = 3.2526$ Å, $a_{ZnMgO} = 3.2566$ Å, $c_{ZnO} = 5.2068$ Å and $c_{ZnMgO} = 5.2097$ Å. Since the typical behavior of $Zn_{1-x}Mg_xO$ lattice parameters as a function of the Mg content is not obtained (see Figure 2.4(b)), this result suggests that the Mg atoms do not substitute Zn ones but occupy interstitial positions producing an increase of the unit cell in all the directions. Representative $2\theta-\omega$ scans taken from these maps are shown in Figure 4.9. It can be seen that there is no preferential orientation, being $(10\bar{1}1)$ the strongest peak, as usual in polycrystalline ZnO (ICDD No. $36-1451$).

4.3 Self arranged $Zn_{1-x}Mg_xO$ nanowires

Patterned ZnMgO pellets described in Section 4.2 with four different areas were used as substrates for the growth of $Zn_{1-x}Mg_xO$ ordered NWs. The used configuration consisted on two source pellets at both sides of a patterned pellet which act as substrate, as shown before in Figure 2.6(e). As a reference, ZnO NWs were also grown on ZnO patterned pellets during several growing times. The growth conditions are shown in table 4.3.

4.3.1 Morphological properties after the growth

First, NWs evolution in time was analyzed in the case of pure ZnO for growth times of $1, 5$ and 10 hours.

Figure 4.10 shows SEM pictures of the non irradiated area (a1-a3) and irradiated region E1 (b1-b3) for different growing times while in Figure 4.11 E2 (a1-a3) and E3 (b1-b3) irradiated regions can be seen. As can be appreciated 10 and 5 hours growths (labels 1 and 2 in the

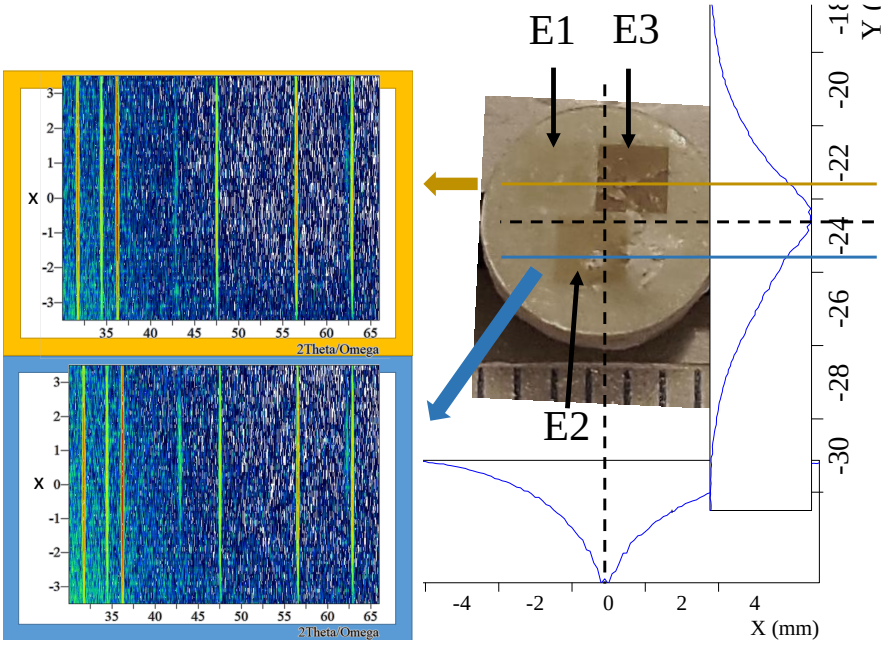

(a) ZnMgO $2\theta - \omega$/x maps (b) ZnMgO irradiated pellet

Figure 4.8: Used configuration for taking XRD $2\theta - \omega$/x mapping. The $2\theta - \omega$ scans were taken by steps of 0.02 degrees at x positions shifted by steps of 0.2 mm

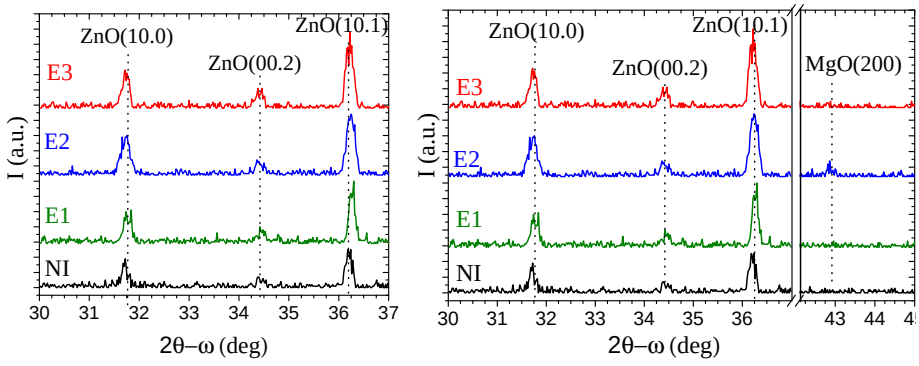

(a) ZnO XRD diffractogram (b) ZnMgO XRD diffractogram

Figure 4.9: $2\theta - \omega$ scans for patterned pellets a) pure ZnO and b) ZnMgO

	Samples	Growing time (h)	wt. % MgO	at. % Mg
Set ZO	Source ZnS Substrate: ZnO	10	0	0
	Source ZnS Substrate ZnO	5	0	0
	Source ZnS Substrate ZnO	1	0	0
Set ZMO	Source ZnS+MgO	10	5	5.7
	Substrate ZnO+MgO		5	4.8
	Source ZnS+MgO	1	5	5.7
	Substrate ZnO+MgO		5	4.8

Table 4.3: Description of the self arranged NWs growth conditions. All the mixtures were milled during 5 hours. All the growths were performed at atmospheric pressure, at 900 °C using 1.5 slm argon flow as carrier gas. Here substrate means patterned pellet acting as substrate.

pictures) resulted in plenty of non oriented NWs. The samples were so covered that it was almost not distinguishable the irradiated areas from the non irradiated one. It is worth to notice that in the irradiated regions the micro- and nanostructures appear earlier than in non irradiated one, giving rise for times as short as 1 hour (label 3 in pictures) to strong differences, between irradiated and non irradiated areas. In addition, for this time, in E1 region the NWs are self arranged in arrays which period corresponds to the laser line overlapping described in Chapter 2. For this reason 1 h was finally selected as the adequate growing time for the growth of self arranged ZnMgO NWs.

Figure 4.12 shows high magnification SEM images of nanostructures grown during 1h on the different irradiated areas for both pure ZnO (left column) and ZnMgO (right column). Structures grown on regions E1 (a) and E2 (b) consist in microcrystals with plates in which top, short and thin wires develop. These small wires seem to be the first stages of the absolutely NWs covering for longer growing times. In the pure ZnO samples (left column), where the density of these structures was lower than in ZnMgO (right column), it is possible to see the patterned pellet, in which the initial LIPSS are still visible between

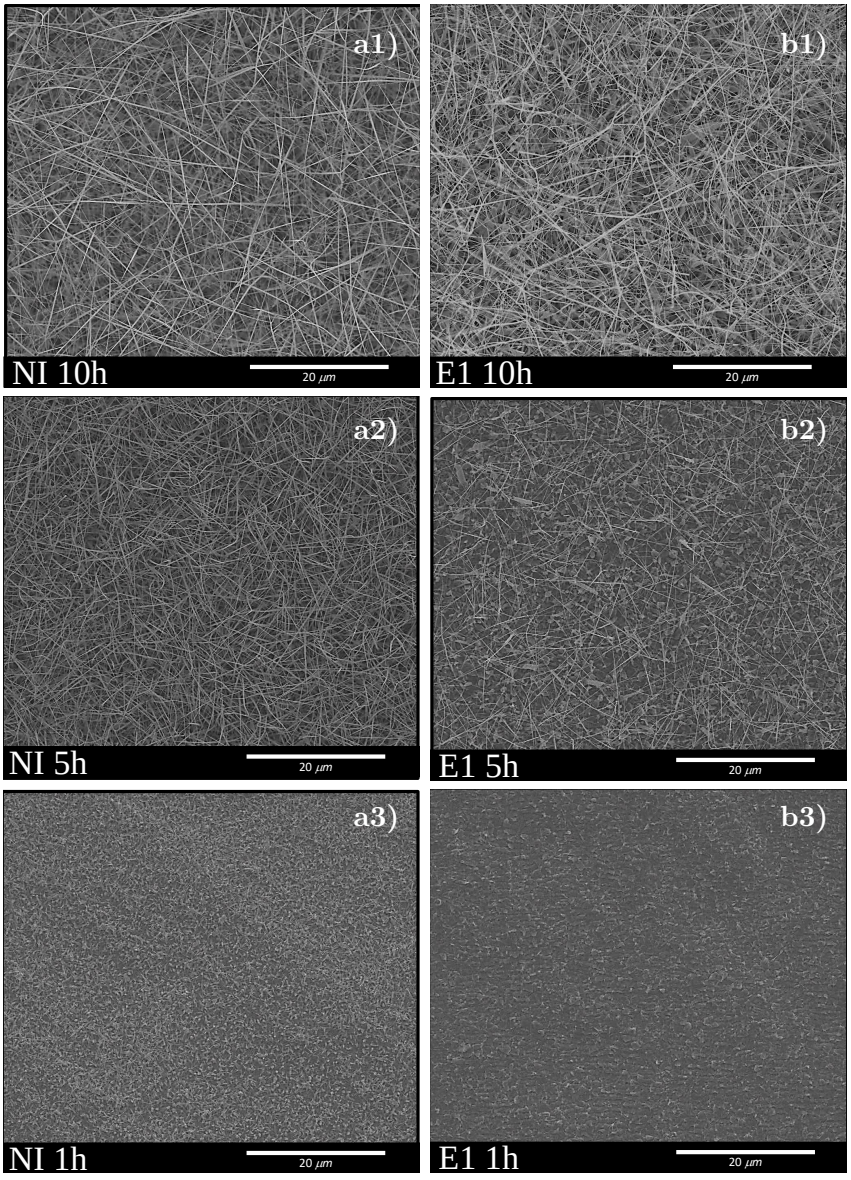

Figure 4.10: SEM pictures for ZnO nanostructues grown during different times grown on a) Non irradiated area and b) irradiated region E1. Labels $1, 2, 3$ refer to 1h, 5h and 10h growth respectively.

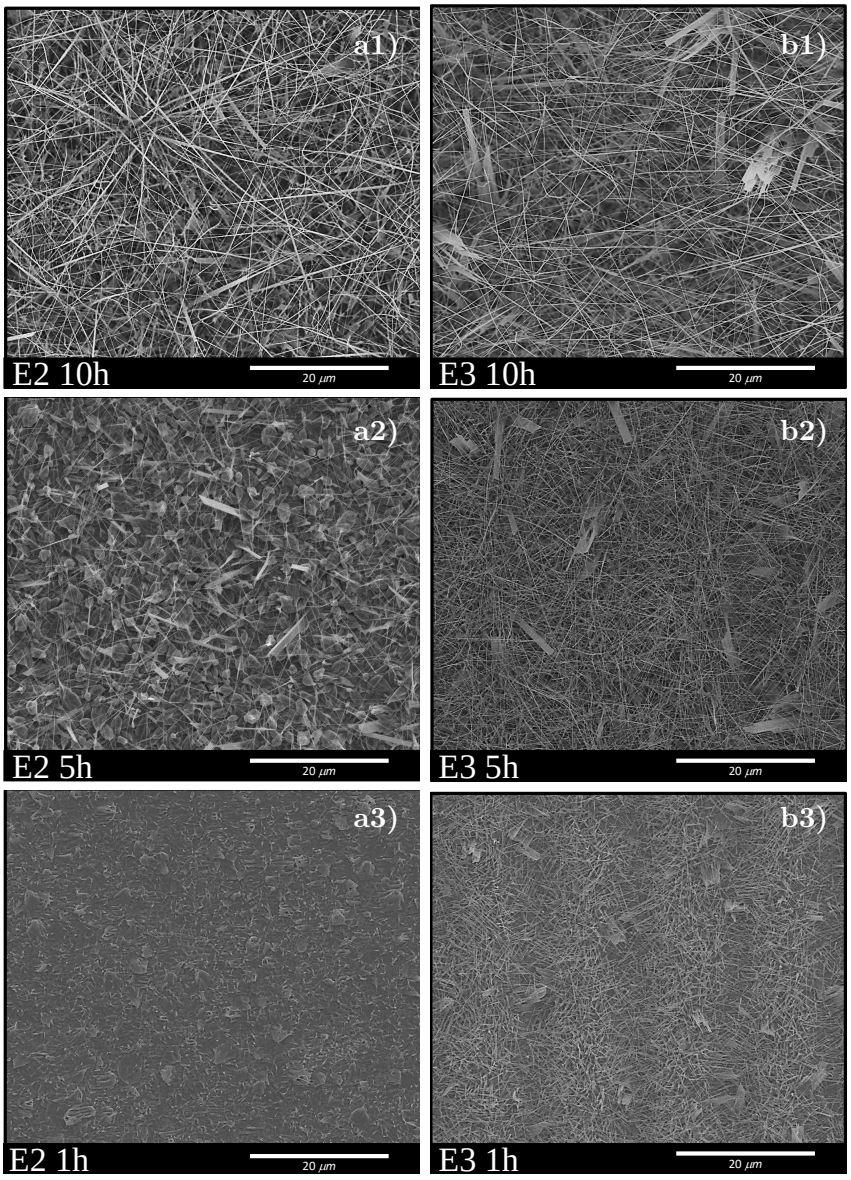

Figure 4.11: SEM pictures for ZnO nanostructues grown during different times grown on a) $E2$ and b) $E3$. Labels $1, 2, 3$ refer to 1h, 5h and 10h growth respectively.

the structures. In the case of E3 zones (c) the structures obtained consist in arrays of partially oriented nanowires and some beehive like microstructures. These structures emerge preferentially from the overlapped zones, where more material has been ejected and redeposited thus acting better as a nucleation site. NWs are several microns long and around $200-300$ nm thick whilst the beehive like structures consist on irregular shaped tubes with a transverse size of around $2-3$ μm and walls with a thicknesses of about 200nm. The inner part of the tubes is divided as well in smaller pipes by walls of the same thickness range. On top of some of the walls that form part of the beehive shaped microstructures, very thin (below 50 nm) NWs are observed. These NW became longer until cover almost all the irradiated surface for longer growing times. The main difference between ZnO and ZnMgO samples is that in the latter there are more structures beyond nanowires than in the former. This could be due to the fact that pellets doped with Mg presented higher roughness which acts as nucleation points.

The change of morphology in doped samples, in particular the formation of plates have been already reported for ZnMgO and attributed to differences in the surface energy of the different faces [79].

Related with the non irradiated zone, huge differences can be observed in respect the irradiated ones, as can be observed in Figure 4.13. Pure ZnO non irradiated areas (a) presented a low covering of needles ended by thin and short NWs which became, for growing times of 5 and 10h, in a high density of randomly oriented NWs (Figure 4.10(a2-a3)) having a diameter ranging from 60 to 200 nm as those obtained in the previous section. Meanwhile for 1 hour of growth time, ZnMgO samples presented a density of NWs that was much higher than for pure ZnO. This is attributed to the higher roughness of doped samples surface, as explained before.

4.3.2 Optical properties after the growth

After the growth of nanostructures, CL measurements as those described in Section 4.2.2 were taken on areas of about $20 \times 10 \mu m^2$. Spectra recorded in each irradiated area and in the non irradiated one are shown in Figure 4.14.

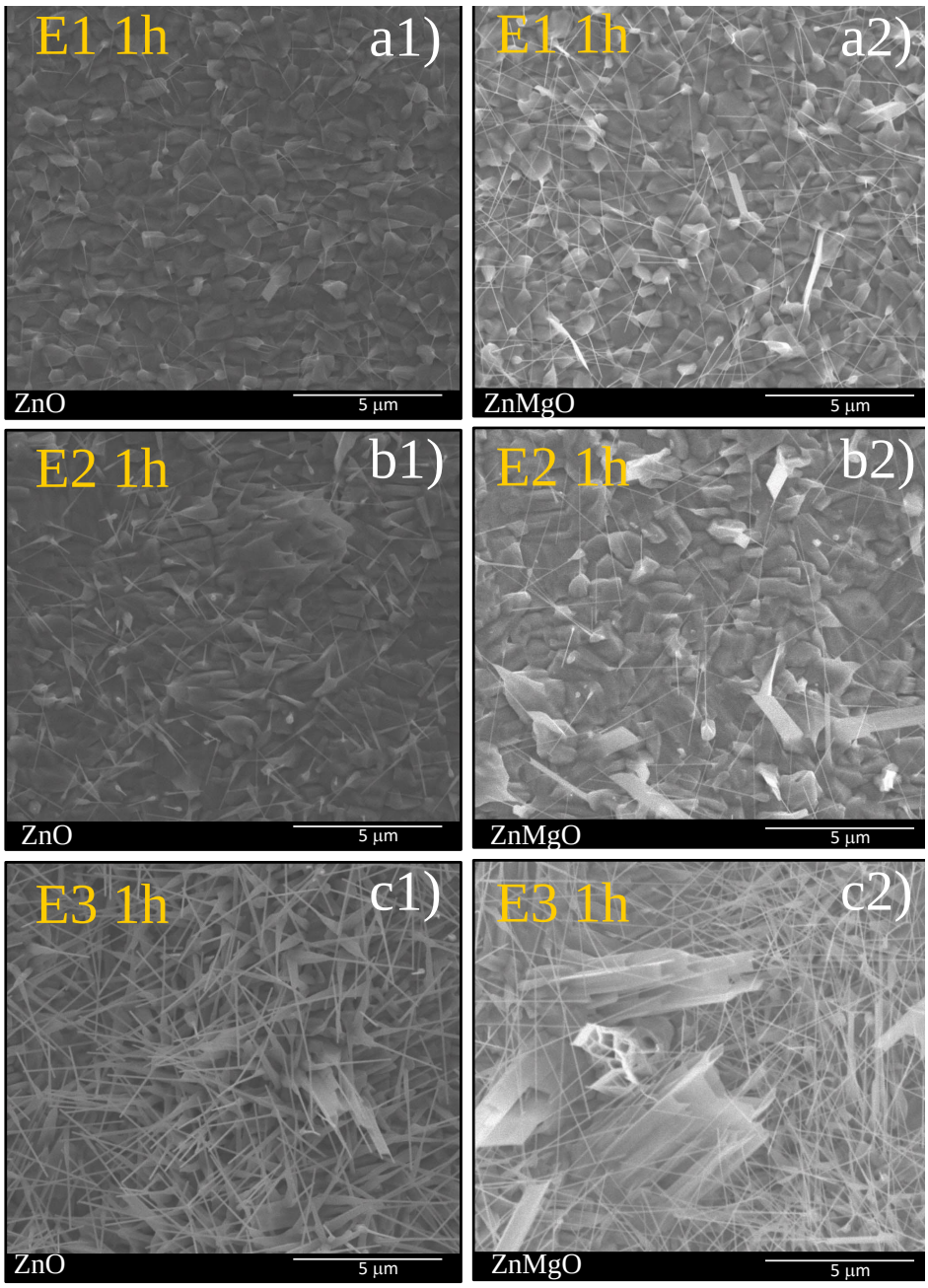

Figure 4.12: SEM pictures of ZnO and ZnMgO nanostructures grown during 1h on irradiated zones a) E1, b) E2 and c) E3.

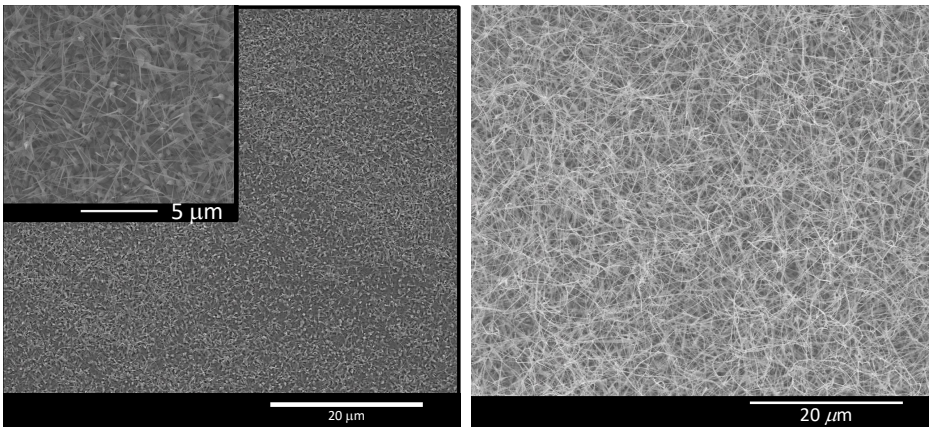

(a) ZnO non irradiated area (b) ZnMgO non irradiated area

Figure 4.13: SEM pictures of ZnO and ZnMgO nanostructures grown during 1h on non irradiated pellet areas.

Regarding the NBE band no major changes are observed between ZnO (black) and ZnMgO (red) samples, nevertheless it can be seen that Mg doped nanostructures produce an increasing of the DL band intensity in respect pure ZnO. In addition, irradiated areas present in general higher relative intensity than the non irradiated one for both materials. In order to know the origin of this behavior, punctual CL measurements were performed in different parts of the samples. Figure 4.15 shows CL spectra and a panchromatic CL image taken in region E3 of ZnO sample. As can be seen the luminescence of microstructures is greater than that one from other zones. Thus we associate the increased DL band intensity observed in the set of samples to the density of microstructures, that was higher in the irradiated zones and even more in ZnMgO samples.

Similar results were found in Al doped ZnO materials by Ortega *et al.* [85]. In this work is shown that the internal part of the microboxes emit with higher intensity than the external faces or other planar features of the sample. Authors attributed that to the higher intensity of the defect related green band in these zones.

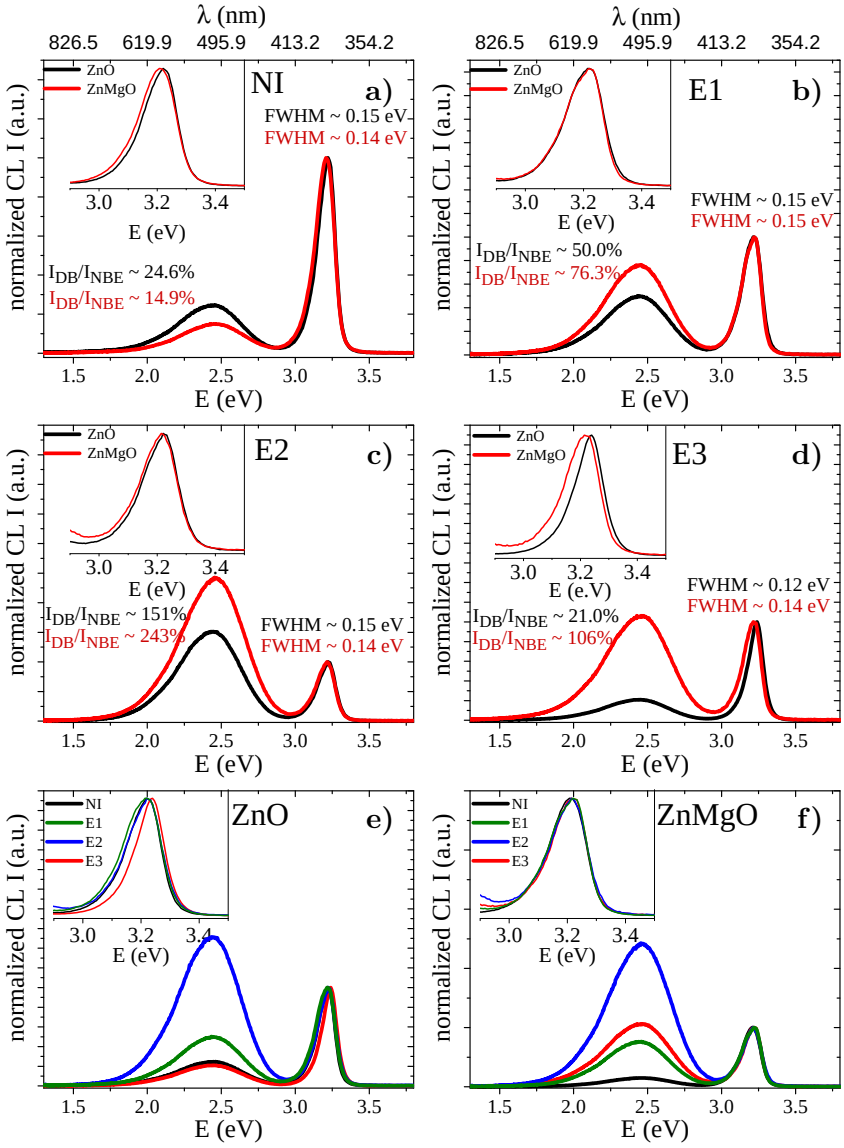

Figure 4.14: CL spectra after 1 hour growth on areas: a) Non irradiated and in the irradiated areas b) E1, c) E2 and d) E3. CL spectra on all the areas for samples: e) ZnO and f) ZnMgO.

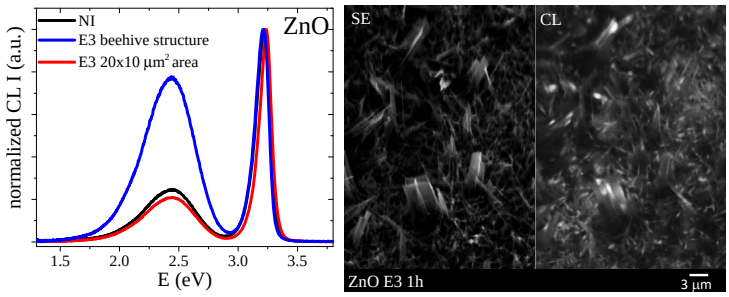

(a) (b)

Figure 4.15: CL measurements taken in ZnO sample a) spectra and b) panchromatic image.

This aspect is of great importance for the performance of ZnO-based sensing devices, since for NWs gas sensitivity was found to be strongly related to the luminescence intensity of DL [86, 87].

After micro- and nanostructures growth the different areas are not distinguishable at naked eye, so it is not possible to extract information about the structural properties of each area separately.

Luminescence properties in ZnO-MgO alloys are one of the most outstanding characteristics of the material, so the ability to change their morphology while preserving the luminescent emission, is a crucial aspect for obtaining ZnO based multifunctional materials. In the same way, the ability to change and enhance the optical properties of devices based on this alloy while keeping the same sample morphology is an interesting aspect, as will be shown in the next chapter.

Chapter 5

$(10\bar{1}0)$ $\mathbf{Zn_{1-x}Mg_xO/ZnO}$ heterostructures

As said in the Introduction chapter, growth of ZnO heterostructures in nonpolar and semipolar orientations is being a major area of research in recent years, due to the consequent reduction of the polarization in the growth direction. This chapter illustrates the morphological, optical and structural characterization that has been developed on nonpolar $(10\bar{1}0)$ $Zn_{1-x}Mg_xO$/ZnO based optical microcavities (MCs) grown by molecular beam epitaxy. The study has been made on *m*-oriented ZnO substrates and the layers were grown all of them with the same Mg composition at around 23%, so that under the same growth conditions. For notation simplicity $Zn_{0.77}Mg_{0.23}O$ layers hereinafter will be referred to as ZnMgO layers. This percentage allowed us to have a good reflectivity by means of a high enough index contrast in DBRs, without sacrificing the quality that would be arisen for high lattice mismatches between the bilayers.

As explained in Chapter 2, the microcavities were designed to be in the weak-coupling regime with a working λ of 410 nm. In this respect the cavity consisted in a ZnO λ-thick layer while DBRs were performed by stacking different quantities of ZnMgO/ZnO bilayers with a thickness of $\lambda/4$. In what follows, the form to label a complete microcavity structure will be, for example DBR_4/C/DBR_5 which consists in 5 pairs of ZnMgO/ZnO layers grown on the ZnO substrate followed by a ZnO

active region and finally a top 4 pairs of ZnMgO/ZnO layers. (See Figure 2.8).

A high crystalline quality of a complex multistructure as MC is, can only be acquired if every stage of the growth is assessed. Thus, in the following sections morphological, optical and structural properties of single ZnMgO layers, bottom DBRs, half MCs and the entire microcavity structures with different DBRs size will be described. Some of the findings of this chapter are based on the results previously obtained by the "Nano" team at CHREA-CNRS in Valbonne, France.

5.1 Morphological properties

The morphological properties of substrates and samples were analyzed exploring the surface by atomic force microscopy (AFM). As said in Chapter 2, before introducing the ZnO substrates into the reactor, substrates were annealed at high temperature (1100 °C) in an oxygen atmosphere, leading to a step-and-terrace surface that can be seen in Figure 5.1(a). The typical root mean square (RMS) roughness of all the employed substrates was in the order of 0.2 nm for a 5×5 μm^2 scanned areas. Figures 5.1(b)-(d) show AFM pictures of the different stages of a MC growth. Samples exhibit a stripe-like morphology, with elongated features parallel to the in-plane c direction.

Figure 5.2(a) shows the RSM roughnes of different m-oriented systems. In blue squares is represented the ZnMgO/ZnO multilayers roughness (including bottom mirrors, half and full MCs) as a function of the number of $\lambda/4$ bilayers. The single ZnMgO layers roughness (pink circles) is depicted as a function of their thickness. As can be seen, the RMS roughness of both kind of structures raised as the total thickness of the sample increased. Comparing with the multilayers RMS roughness evolution, single ZnMgO layers roughness increases with a higher raising rate. In both cases single layers and multilayers systems, the high surface quality remains constant at larger scales, as displayed in Figure 5.2(b). This figure shows the measured RSM for the thickest single layer (pink circles) and the thickest multilayer system (blue squares). As can be seen the RMS roughness is independent

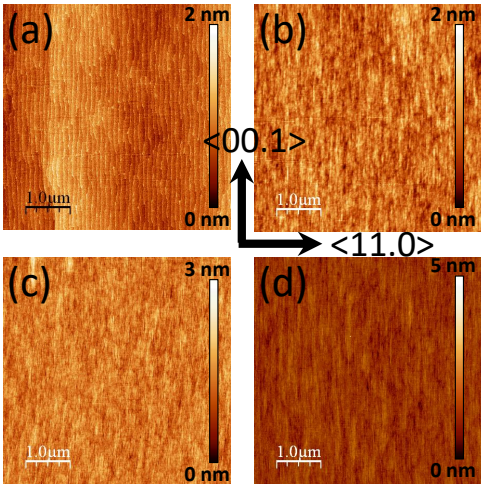

Figure 5.1: AFM images of a) an annealed $(10\bar{1}0)$ substrate, b) a DBR_{10}, c) a DBR_{21} and d) a $DBR_{10}/C/DBR_{21}$ microcavity.

of the surface area and can be kept in the order of 1 nm even for the DBR_{66} structure.

If homogeneous cavities with high quality factors want to be obtained, the previous in-plane uniformity must be accompanied by constant Mg composition in consecutive ZnMgO layers. In order to assure that, secondary ion mass spectrometry (SIMS) profiles were performed by Nano team in both single ZnMgO layers and in the full ZnMgO/ZnO microcavities. In these profiles the Mg content is depicted as a function of the depth, throughout the whole structure, from the top surface of the sample up to the substrate. The Mg concentration is found to be homogenous along the epitaxial single films, as can be seen in Figure 5.3(a) for one of our samples. However, it was observed that for multilayer structures a slight increase of Mg composition within consecutive ZnMgO layers occurs when the growing time is longer than 10 hours uninterrupted, as observed in Figure 5.3(b). This effect was accompanied of a slight decrease in the thickness of the individual ZnO layers. There are two ways to overcome this problem, one solution is to correct the growth time of individual $\lambda/4$ layers by comparing with these slow variations. The other possibility is to perform the growth by steps.

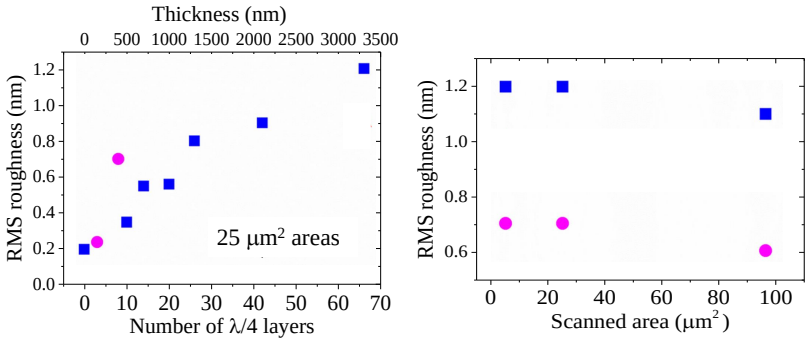

Figure 5.2: a) RMS roughness of single ZnMgO layers (circles) and different ZnMgO/ZnO multilayer systems (squares): a) as a function of the number of $\lambda/4$ layers (or equivalent thickness for pure ZnMgO layers) b) as a function of the size of the scanned area for the thickest samples.

We check this last option revealing that to stopping the growth does not affects microcavity quality even if the sample is taken out of the chamber in order to perform their characterization. The high control in Mg composition that the MBE method provides, combined with the low growth temperature, which helps in preventing any interdiffusion between ZnO and ZnMgO, allowed to have a constant Mg composition and the achievement of abrupt interfaces. This can be seen in Figure 5.4, where cross section SEM pictures for a DBR_9/C/DBR_{10} MC are shown.

Notwithstanding the high homogeneity of the MCs, the structures were cracked as can be seen in Figures 5.5(a) and 5.5(b), where optical and SEM images of the DBR_{15}/C/DBR_{16} microcavity can be respectively seen. Cracks appear along to $< 11.0 >$ in plane direction with a density between 0.03 and 0.04 μm^{-1} which corresponds with a mean crack distance of $24 - 38$ μm. These cracks are perpendicular to the sample surface, extending along the entire structure and penetrating into the ZnO substrate as can be seen in 5.5(b). This type of fissures has been observed in all the heterostructures displaying more than $20\lambda/4$ layers and also in the 400 nm thick single ZnMgO layer.

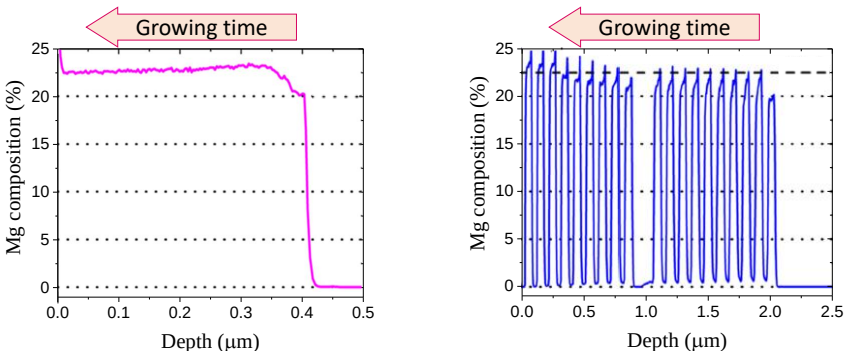

(a) (b)

Figure 5.3: SIMS profile of the Mg concentration in a) a single 400 nm thick ZnMgO layer and b) a $DBR_9/C/DBR_{10}$ microcavity. Original images taken from [88].

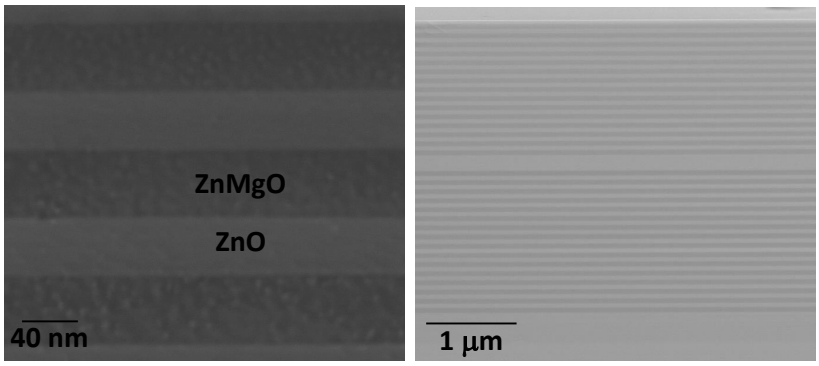

(a) (b)

Figure 5.4: Cross-section SEM pictures of a) several layers belonging to a $DBR_{15}/C/DBR_{16}$ MC and b) full $DBR_{15}/C/DBR_{16}$ microcavity.

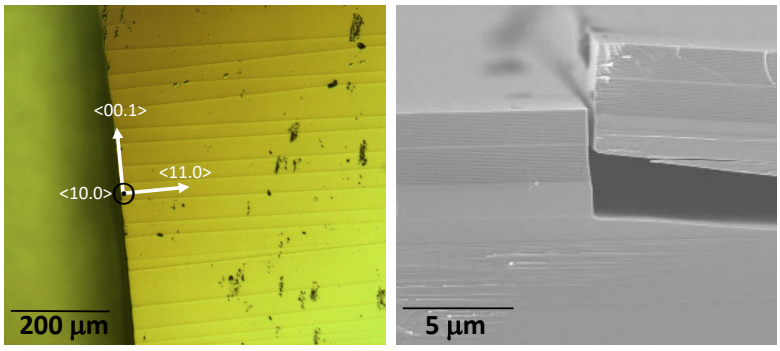

(a) (b)

Figure 5.5: Pictures of a DBR_{15}/C/DBR_{16} microcavity a) optical microscopy surface image and b) low magnification SEM cross section image.

Similar results has been reported in *m*-oriented GaN-based heterostructures [89, 90]. The origin of this behavior can be at the biaxial strain observed in these samples (analyzed in more detail in section 5.2), which is of tensile type along the $< 00.1 >$ crystallographic direction and compressive one along $< 11.0 >$. This fact, together with the difference in the thermal expansion coefficients which shows up upon cooling down the growth chamber, results in cracked samples.

5.2 Structural properties

Structural properties of samples were analyzed through High Resolution X Ray Diffraction measurements. 2θ-ω scans show the peaks corresponding to the substrate and layer, joined to those associated to Pendellösung fringes, as can be seen in Figure 5.6, confirming the flatness of the multilayer interfaces and also of the interface between the ZnMgO layer and the ZnO substrate. Lattice parameters and strain state of the heterostructures were checked by Reciprocal Space Maps (RSM). Symmetrical and 20.2 asymmetrical RSM are shown in Figure 5.7 where the ZnMgO and the ZnO layers exhibit almost the same in-plane lattice parameter, i.e., the growth is pseudomorphic. It is worth

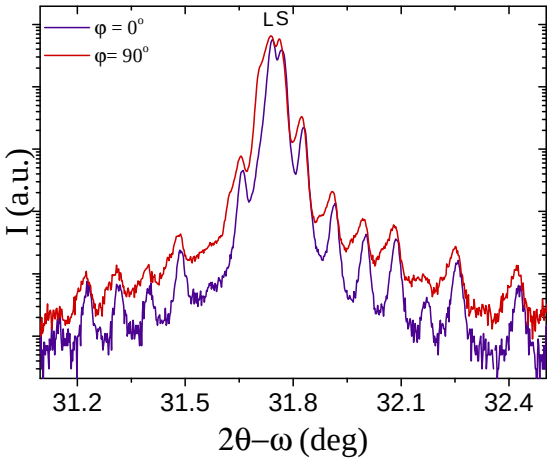

Figure 5.6: Symmetric 2θ-ω scans along the c-axis (blue) and perpendicular to it (red).

Lattice	a (Å)	c (Å)	$\epsilon_{[11.0]}(\%)$	$\epsilon_{[00.1]}(\%)$
ZnO	3.2499	5.2105		
$Zn_{0.77}Mg_{0.23}O$	3.2523	5.1938	0.074	-0.32

Table 5.1: Calculated lattice parameters of samples (±0.0005 Å) and their lattice mismatch obtained from the combination of symmetric and asymmetric RSM.

to notice that the Pendellösung fringes are still clearly observed, even in the asymmetrical configuration.

The mean values of ZnO and ZnMgO lattice parameters were obtained from symmetrical and asymmetrical RSM. These lattice parameters give rise to an in plane compressive lattice mismatch along [11.0] and tensile one along [00.1]. (See Figure 5.8). These values are shown in Table 5.1.

Our results are consistent with those obtained by Laumer *et al.* [43] for ZnO-MgO alloys with similar Mg amount. This tensile stress could be the origin of cracks. The large spot size (around 1×1 mm^2) of the X-Ray beam provides mean values, thus the analysis of the strain gradient as a function of the distance to the crack is not possible.

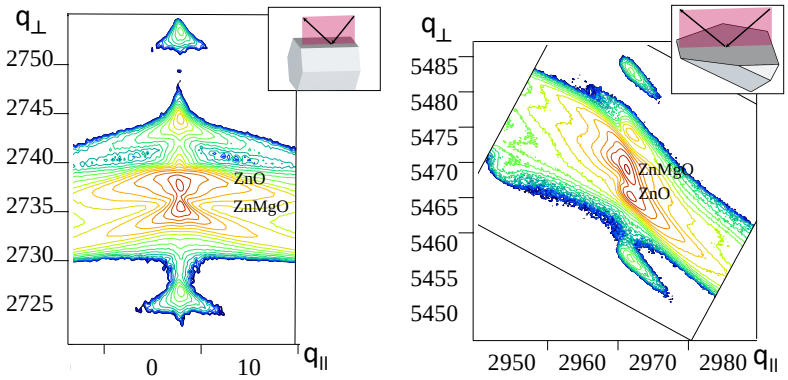

(a) 10.0 symmetric RSM (b) 20.2 asymmetric RSM

Figure 5.7: Reciprocal space maps for a half MC C/DBR_{30} taken with the diffraction plane coplanar with the plane that contains the c-axis.

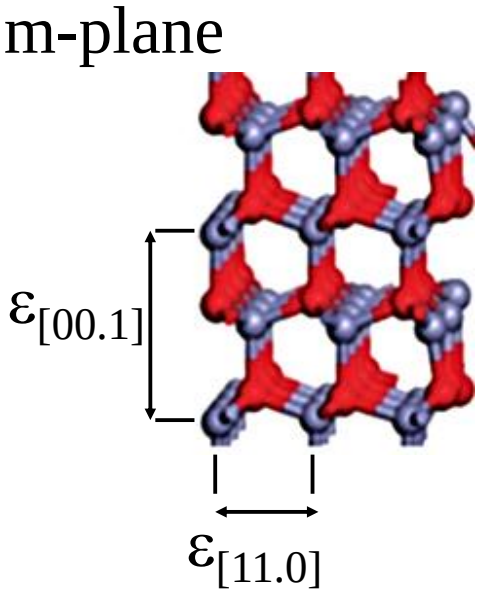

Figure 5.8: View of the m- ZnO crystal surface. Original image taken from [91].

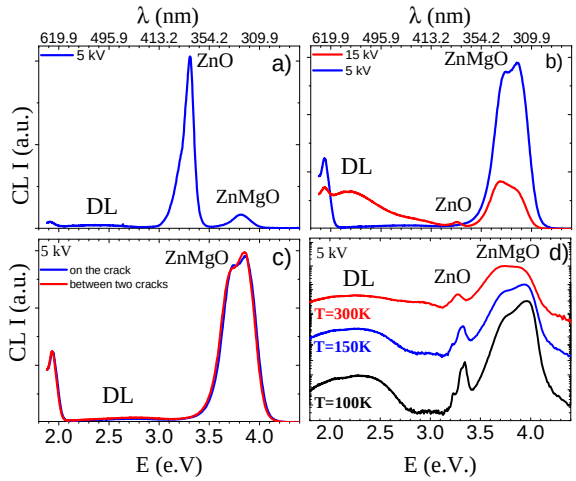

Figure 5.9: RT CL measurements of a) $DBR_{18}/c/DBR_{22}$ MC taken at 5 kV, b) Single ZnMgO layer taken at low and high acceleration voltages and c) Single ZnMgO layer taken at the crack and between two of them. d) Single ZnMgO layer taken at different temperatures.

5.3 Optical properties

CL measurements were performed in order to analyze the optical properties and quality of microcavities. Figure 5.9(a) shows room temperature CL measurements for a $DBR_{18}/c/DBR_{22}$ sample. In general, CL spectra of MCs are dominated by the near band edge (NBE) ZnO optical transition around 3.3 eV in company with the weak deep level (DL) emission, which is indicative of high NBE radiative efficiency and excellent optical properties. ZnMgO NBE peak can also be seen around 3.8 eV.

Figure 5.9(b) corresponds to a single ZnMgO layer with a slightly gradual Mg content. It can be inferred from Figure 5.9(b) that the DL band is related with the ZnO substrate, since it only appears in company with the ZnO NBE peak for a high acceleration voltage. In Figure 5.9(c) the spectra taken at low acceleration voltage in the crack and in the middle between two cracks is depicted. It is worth to notice that no differences were found between both spectrum suggesting that the presence of cracks do not change the luminescence properties.

Finally, spectra taken at different temperatures can be seen in Figure 5.9(d) in which the ZnO DAP transition can be observed at 3.22 eV.

5.4 Microcavities quality factor

The following measurements have been provided by Nano team at CRHEA and are included in this thesis because of their importance for the evaluation of MCs quality.

In a microcavity, since the mirrors reflectivity is not 1, the intensity of the confined cavity mode decays with time by photon escaping through the mirrors. These losses are characterized by a dimensionless parameter, the cavity quality factor Q, which can be calculated by measuring the energy of the cavity mode (E_c) and its linewidth (ΔE) using the expression:

$$Q = \frac{E_c}{\Delta E} \tag{5.1}$$

The quality of the MCs was analyzed by polarization resolved room temperature macroreflectivity measurements. The spot diameter was in the order of 100 μm and the measurements were taken at normal incidence, in the center of the sample, using a polarization parallel to the c-axis (optical axis) and perpendicular to it.

In Figure 5.10(a) results for a DBR_{10} are shown as an example. The stopband of the DBR is clearly visible and centered at different energies in each polarization directions, as expected from ZnO and ZnMgO birefringence ($\Delta n = n_e - n_o$). Both spectra are characterized by a flat stopband, with a stopband width of about 0.32 eV. The center energies with light polarized perpendicular and parallel to the c-axis are 2.96 and 2.94 eV, respectively. Such birefringence effect has also been reported on m-plane nitride DBRs [92–95]. For the same reason, two orthogonally polarized cavity modes are detected at normal incidence in full microcavity structures, as shown in Figure 5.10(b).

These cavity modes give rise to quality factors in the order of several hundreds, as is shown in Figure 5.11(a). It is worth to notice that the Qs corresponding to a polarization perpendicular to the c-axis are

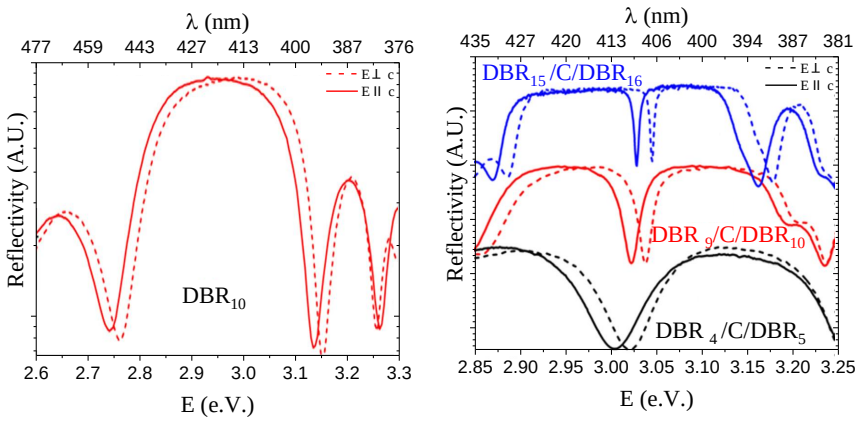

Figure 5.10: Polarization-resolved room-temperature macroreflectivity measurements at normal incidence on: a) DBR_{10} and b) several entire microcavities where the spectra are vertically offset for clarity. Original images taken from [88]

larger than those of the polarization parallel to the c direction; this observation is consistent with the birefringence evolution as a function of Mg composition (i.e., larger birefringence than ZnO and same sign) [36].

In order to analyze the spatial homogeneity, polarization resolved microreflectivity (diameter about 2 μm) spectra were taken. Figure 5.11(b) shows microreflectivity measurements acquired at the sample border, where the inhomogeneities are expected to be larger, for a $DBR_{15}/C/DBR_{16}$ microcavity. For comparison the corresponding macroreflectivity spectra, taken at the sample center, are also displayed. As can be seen there is a slight shift of the cavity mode, which is attributed to the fact that layers are slightly thinner at the samples borders. With the purpose of studing in more detail this shift, microreflectivity measurements were performed every 10 μm along a line of 150 μm. The analysis of the microreflectivity spectra indicates a negligible shift of the cavity modes as well as of the FWHM, with typical variations being in the order of hundreds of μeV (see Figure 5.12).

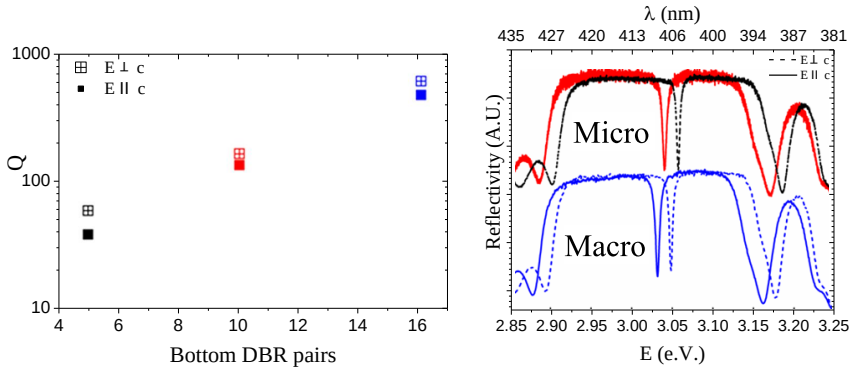

(a) (b)

Figure 5.11: a) Q as a function of the number of pairs in the bottom DBR and b) Polarization resolved room temperature reflectivity measurements at normal incidence on a $DBR_{15}/c/DBR_{16}$. Original images taken from [88].

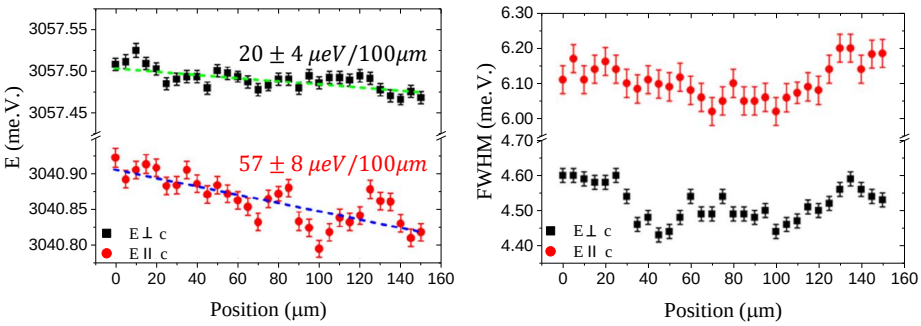

(a) (b)

Figure 5.12: a) Energy and b) FWHM of the cavity modes extracted from polarization resolved microreflectivity measurements performed every 10 μm close to the sample border. Original images taken from [88]

Chapter 6

$(01\bar{1}2)$ $\mathbf{Zn_{1-x}Mg_xO/ZnO}$ systems

In the previous chapter, nonpolar *m*-oriented ZnO-based microcavities (MCs) obtained by MBE have been analyzed. As a first step towards future semipolar ZnO-based MCs, the MBE growth conditions were optimized for the obtention of $(01\bar{1}2)$ $Zn_{1-x}Mg_xO$/ZnO heterostructures. In this respect, this chapter shows the characterization of $(01\bar{1}2)$ $Zn_{1-x}Mg_xO$ layers grown by MBE. In such a low-symmetry material system, during the structural characterization, additional features appear in symmetric-reflection scans, which can be described as arising from hybrid multiple diffraction (HMD). This is a rare case of multiple diffraction phenomenon which appears only in heterostructures with high crystalline quality.

This finding gave us the opportunity to study this outstanding behavior and analyze, to our knowledge for the first time, HMD in a system with a symmetry as low as it is the $(01\bar{1}2)$ $Zn_{1-x}Mg_xO$/ZnO heterostructure. This study opens the door to interesting applications of which we can take advantage.

Thus, in this chapter the possibilities brought about by HMD are illustrated from a structural characterization point of view. Also, the morphological and optical properties of the layers will be shown.

Sample	% Mg (EDX)	Thickness ZnO buffer layer	Thickness $Zn_{1-x}Mg_xO$ layer	Substrate RMS	Layer RMS
S27	27	45	525	0.133	0.416
S35	35	45	76	0.221	0.572
S43	43	45	188	0.163	0.457

Table 6.1: Morphological and compositional characteristics of samples. All the thickness are given in nm.

6.1 Morphological properties

The study was performed on $Zn_{1-x}Mg_xO$ single layers grown on $(10\bar{1}2)$ ZnO substrates with three different Mg contents of $27 \pm 3\%$, $35 \pm 6\%$ and $43 \pm 5\%$, as determined by EDX and confirmed by optical measurements. These samples have different thicknesses and we will refer to them as S27, S35 and S43 respectively (see Table 6.1).

Morphological properties were explored by AFM. Annealed substrates exhibit a RMS roughness of 1.7 Å, for a 1×1 μm^2 scanned area, and atomic terraces of around 50 nm wide as shown in Figure 6.1(a). Furthermore the $Zn_{1-x}Mg_xO$ layers display typically a surface roughness of $\sim$ 4.8 Å, as shown in Figures 6.1(b)-(d). Since the samples have different Mg content, we can not evaluate the roughness as a function of the thickness, nevertheless the measured RSM roughness is in the range of values reported for *m*-oriented single layers in the previous chapter. Any of these layers grown of *r*-oriented substrates presented any crack, even the thickest one with a thickness of more than 500 nm, unlike the *m*-oriented layers, which exhibited cracks in the layers with thickness of 400 nm.

6.2 Structural properties

All the structural measurements shown in this chapter have been labelled according to the system of reference depicted in Figure 6.2. Our choice of orthogonal axes is the following: the X axis matches the

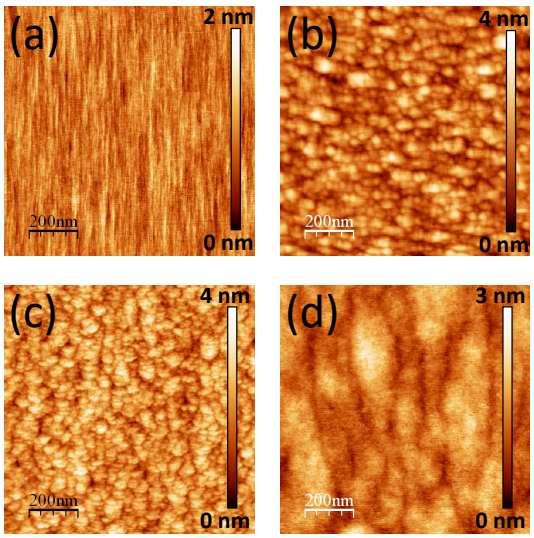

Figure 6.1: AFM images of a) an annealed $(10\bar{1}2)$ substrate, b) a $Zn_{65}Mg_{35}O$ layer, c) $Zn_{57}Mg_{43}O$ layer and d) a $Zn_{73}Mg_{27}O$ layer.

$[0\bar{1}.1]$ direction, the Y axis matches the $[2\bar{1}.0]$ direction and the Z axis is perpendicular to the (01.2) plane. In this figure the incident angle (ω_0) and the angle (φ_0) between the diffracting plane and the reference X axis can also be seen.

$2\theta - \omega$ scans were performed in the set of samples showing satellite peaks in all of them, besides the peaks corresponding to the substrate and layer and those associated to Pendellösung fringes for the two thinnest samples (Figure 6.3). Two families of satellite peaks could be identified, observed at two different 2θ Bragg angles and for different φ_0 positions. The one with lower Bragg angle appears with an approximated six-fold symmetry in φ, at $\sim 0°$, $\pm 60°$, $\pm 120°$ and $180°$ with respect to the φ_0 reference angle (the X axis); we will refer to them as P1-P6 peaks. The other family, observed at a higher 2θ angle, has a two-fold symmetry in φ and is found at $\pm 90°$ (P7 and P8 peaks).

Figure 6.3(a) and (c) shows $2\theta - \omega$ scans for samples S27 and S43 respectively, measured for all the φ_0 angles at which a satellite peak is present. However, in the case of sample S35 (Figure 6.3(b)), the relative intensity of the layer and substrate peaks related with the satellites

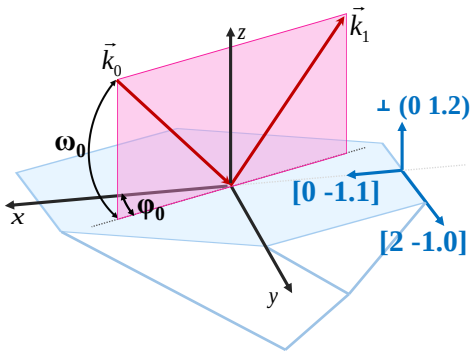

Figure 6.2: Description of the angles and the selected orthogonal system.

ones was low, probably due the low layer thickness, so only the patterns for $\varphi_0 = 0°$ (P1) and $\varphi_0 = 90°$ (P7) are shown as representative.

These "additional" peaks depend clearly on the Mg content of the epilayer, as shown in Figure 6.3(d) where it can be seen that their positions converge towards the position of the ZnO peak. These peaks will be analyzed in more detail in Section 6.4.

The strain state of the samples and the lattice parameters were evaluated through symmetrical and asymmetrical RSM. Figure 6.4 shows the asymmetrical 01.4 and 21.4 RSM for sample S27, where the fully strained state of the sample can be clearly seen.

Initially the determination of lattice constants was made as usual, from RSM measurements. Using the interplanar distance for a hexagonal structure:

$$\frac{1}{d_{hkl}^2} = \frac{4}{3}\frac{h^2 + k^2 + hk}{a^2} + \frac{l^2}{c^2} \tag{6.1}$$

it is possible to obtain the mean lattice parameters of the layers and their in plain lattice mismatches (see Figure 6.5). These values are shown in Table 6.2.

It can be seen that, as expected, the a lattice parameter increases with the Mg content while the c lattice parameter decreases. Regarding to the in plane lattice mismatch, it is compressive along [0$\bar{1}$.1] and tensile along [2$\bar{1}$.0]. These values are higher than those for the m-oriented samples analyzed in the previous chapter ($\epsilon_{[11.0]}$=0.074% and $\epsilon_{[00.1]}$=−0.32%).

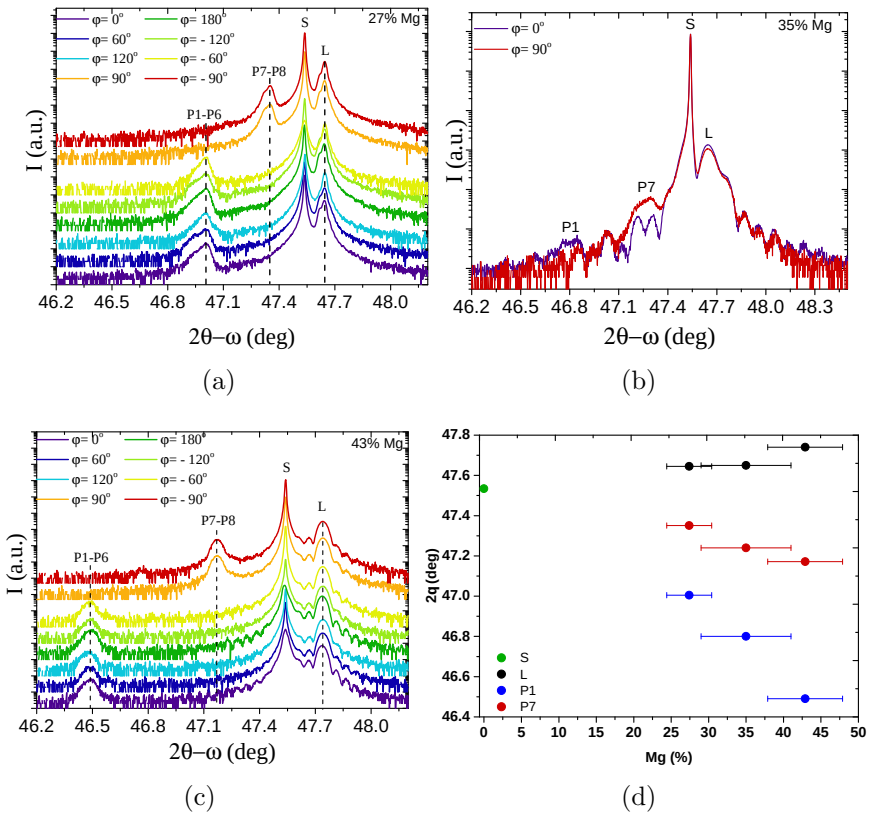

Figure 6.3: $2\theta - \omega$ scans around $(01\bar{1}2)$ primary ZnO reflection for a) S27, b) S35 c) S43 samples and d) Bragg angle positions of satellite, layer and substrate peaks for the set of samples. S/L indicates substrate or layer respectively. When needed, baselines are shifted for clarity.

Sample	a (Å)	c (Å)	$\epsilon_{[0\bar{1}.1]}(\%)$	$\epsilon_{[2\bar{1}.0]}(\%)$
Substrate	3.2495	5.2070		
S27	3.2580	5.1757	0.14	-0.26
S35	3.2608	5.1640	0.19	-0.34
S43	3.2683	5.1445	0.28	-0.45

Table 6.2: Calculated lattice parameters of samples (±0.0005 Å) and their lattice mismatch obtained from the combination of symmetric and asymmetric RSM.

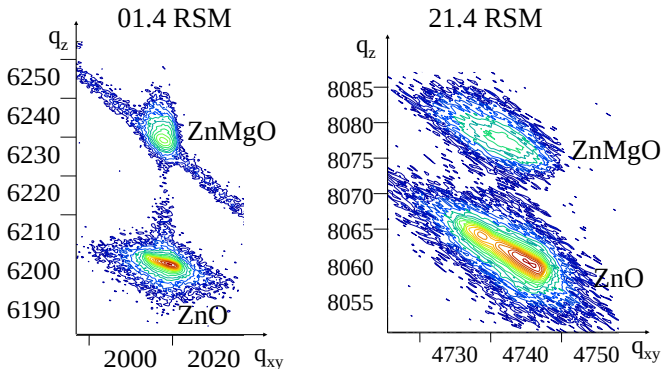

Figure 6.4: Asymmetrical 01.4 and 21.4 RSM for a semipolar *r*- oriented $Zn_{0.73}Mg_{0.27}O$/ZnO system

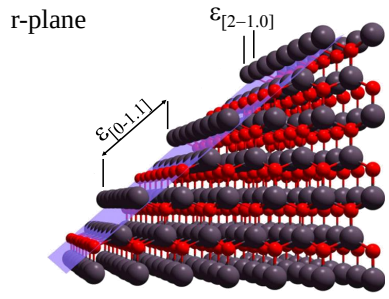

Figure 6.5: Side view of the *r*- ZnO crystal surface. Original image taken from [96].

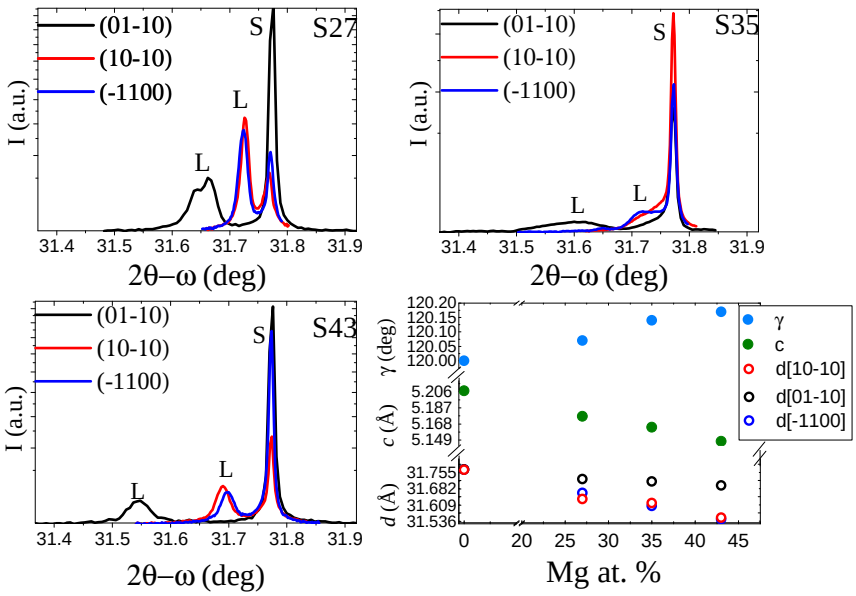

Figure 6.6: $2\theta - \omega$ scans for samples: a) S27, b) S35, c) S43 and d) structural parameters of samples as a function of the Mg content. The directions are based on the coordinate system depicted in Figure 6.7(a)

Nevertheless, as ZnO has different thermal expansion coefficients in the directions normal and parallel to the c-axis [97], an anisotropic strain, joined to a distortion of the basal plane can appear. For an undistorted wurtzite structure, we would expect $d(01\bar{1}0) = d(10\bar{1}0) = d(\bar{1}100)$, thus in order to check the possible distortion, $2\theta - \omega$ measurements were taken for $\{10\bar{1}0\}$ (Figures 6.6(a)-(c)).

From this results it can be concluded that, in fact, the layer basal plane has an orthorhombic distortion as shown in Figure 6.7(a). The doted lines and solid lines show the basal plane of a perfect and distorted hexagonal unit cell, respectively. In the axis system shown, a complete description of the distorted lattice requires four lattice parameters: a, b, c and the angle γ. Thus, in this situation the interplanar distance must be calculated by means of the generic expression for triclinic systems [98]. However, with a properly selection of the coordinate axis, depicted in Figure 6.7(b), then a=b and the interplanar distance can be reduced to [99]:

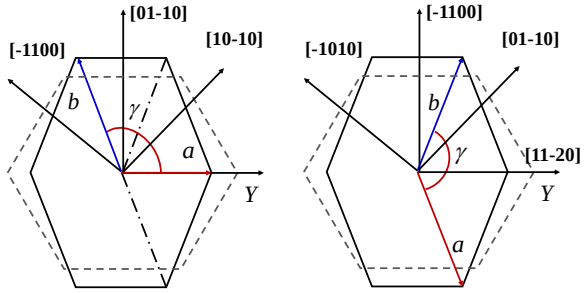

Figure 6.7: Different possibilities for the coordinate axis for a distorted basal plane.

Sample	$d_{[11-20]}$ (Å)	a (Å)	c (Å)	γ (deg)
Substrate	3.2495	3.2495	5.2070	120
S27	3.2554	3.2590	5.1770	120.07
S35	3.2573	3.2643	5.1640	120.14
S43	3.2606	3.2693	5.1475	120.17

Table 6.3: Calculated structural parameters of samples (±0.0005 Å) with orthorombic distortion using eqn. 6.2 and coordinate system depicted in Figure 6.7(b).

$$\frac{1}{d_{hkl}^2} = \frac{h^2 + k^2 - 2hkcos\gamma}{(asin\gamma)^2} + \frac{l^2}{c^2} \tag{6.2}$$

Using this equation and the measurements depicted in Figures 6.6(a)-(c), the structure parameters can be obtained, which are summarized in Table 6.3. Lattice parameter along the c-axis has been determined from (0002), (0004) and (0006) reflections and the fitting of the $l^2 = c^2(2\sin\theta/\lambda)^2$ straight line. It is worth to notice that the a lattice parameters obtained by RSM (Table 6.2) are a mean between that ones obtained if the distorted basal plane is taken into account.

This distortion is found to be dependent on the Mg content of the layer, as can be seen in Figure 6.6(d).

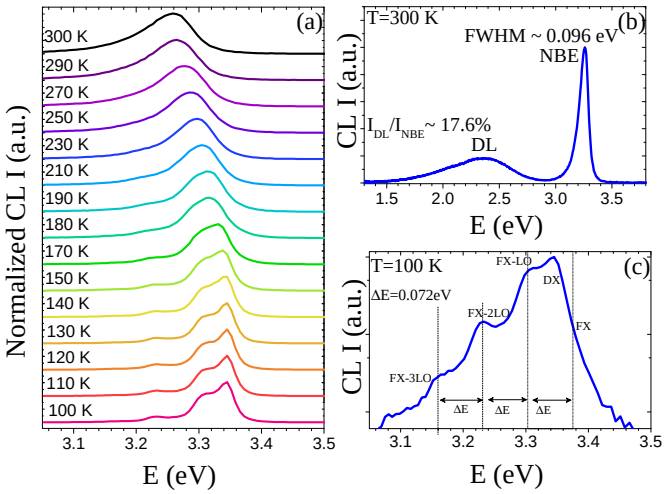

Figure 6.8: CL spectra of a ZnO substrate at at 15 kV a) temperature dependent spectra from 100K to 300K b) at room temperature and c) at 10 K.

6.3 Optical properties

In this section the luminescence of the different $Zn_{1-x}Mg_xO$/ZnO heterostructures will be analyzed. Luminescence of as received ZnO substrates was measured by CL at 15 kV. Figure 6.8(a) shows the temperature dependent spectra from 100K to 300K of the NBE peak. Different features can be observed at low temperature but most of them vanish at high temperature suggesting donor- and/or acceptor-bound excitons. When increasing the temperature, bound excitons get ionized due to thermal activation and free excitons dominate the emission spectra. The free-exciton energy redshifts, due to the thermal induced shrinking of the bandgap, and ends up at about $\sim$ 3.27eV at 300K, as shown in Figure 6.8(b). At RT the spectrum is dominated by the ZnO NBE peak, which is broadened at the low energy side. This peak can be resolved at low temperatures, as can be seen in Figure 6.8(c). Comparing with previous studies [65] the origin of most of these emission features can be identified. Free exciton (FX), donor-bound excitons (DX), first, second and third LO-phonon replicas of free

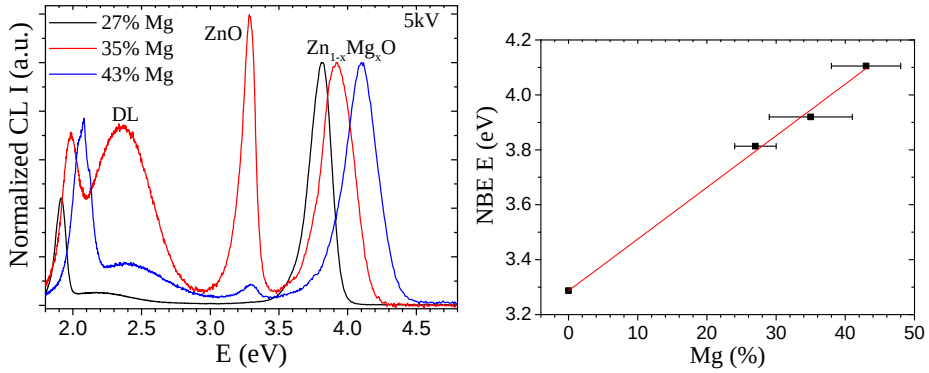

(a) (b)

Figure 6.9: a) CL spectra of the set of samples at 5 kV and b) ZnMgO NBE band energy as a function of the measured Mg content.

excitons (FX-LO, FX-2LO and FX-3LO, respectively) are depicted in this figure.

In Figure 6.9(a) the RT cathodoluminiscence spectra taken at 5 kV for the set of samples is shown. The blueshift in the CL peak as the Mg content increases can be clearly seen. The peak around 3.3 eV is attributed to the ZnO NBE and the band around 2.4 eV can be assigned to DL. It is worth noting that for the S27 sample, which is the thickest, the DL does not appear nor the ZnO NBE peak. This behavior, combined with results shown in Figure 6.8 is an evident sign that the defects belong to the substrate, as happened with m-oriented samples in the previous chapter. Related with the ZnMgO NBE peak, it can be linearly fitted as can be seen in Figure 6.9(b) suggesting that the Vegard's law is satisfied within this range of Mg contents.

6.4 Hybrid Multiple Diffraction

6.4.1 Multiple diffraction

Beyond the routine measurements such as $2\theta - \omega$ scans, reciprocal space maps (RSM)... which employ a two-beam geometry, the analysis of multiple diffraction (MD) processes could provide an alternative

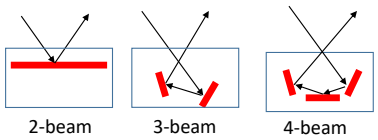

Figure 6.10: Sketch of a n-beam process.

method for the structural characterization of samples. One of the first studies reported on this topic was made by Renninger in 1937 [100] and used for the 222 reflection of diamond, obtaining accurately its lattice parameters [101]. With the same aim and also for the analysis of surface perfection it was later on employed by Cole *et al.* [102], for germanium, and by Post and coworkers, [103, 104] for diamond, silicon and germanium. More recently, MD has been used for the analysis of GaN and ZnO wurtzite materials by several authors, including Bläsing *et al.* [105], Martínez-Tomás *et al.* [106, 107] and Grundmann *et al.* [108]. From a general perspective, MD provides information on crystal symmetry, crystal quality and defects [109, 110].

MD takes place inside a material when more than one set of planes fulfills simultaneously the Bragg condition in the path of the incident beam. We will only consider the case in which two sets of planes are involved, also called as three beam diffraction (See Figure 6.10). In the MD literature these two sets of planes are known as primary and secondary, with diffraction vectors $\vec{P}$ and $\vec{S}$ respectively (see Figure 6.11). The secondary beam is itself diffracted by a third set of planes (so-called as cooperative planes with diffraction vector $\vec{C}$) towards the outgoing primary direction (θ). That is, the combined diffracting effects produced by secondary and cooperative planes ends up matching the direction stated by the primary family of planes. So that, the primary diffraction vector can be expressed as a sum of secondary and cooperative vectors.

$$\vec{P} = \vec{S} + \vec{C} \tag{6.3}$$

Experimentally, since it is not possible to discriminate the different contributions to diffraction between conventional two-beam diffraction and MD, this phenomenon is generally studied for forbidden or very

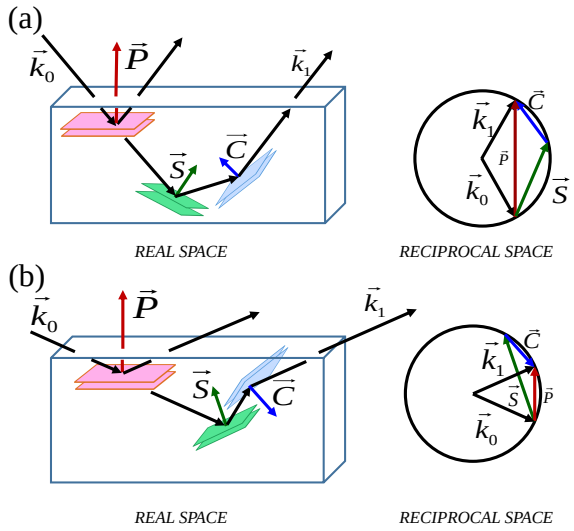

Figure 6.11: Geometry of a three-beam MD in real and reciprocal space. The sum of secondary ($\vec{S}$) and cooperative ($\vec{C}$) vectors produces the primary one ($\vec{P}$). The incidence can take place a) at the upper side of both planes or b) at the upper/bottom side. Images taken from [112]

weak reflections, in which changes in intensity may be more easily observed [111]. Figure 6.11 shows two particular cases of MD in which the incident beam, primary, secondary and cooperative diffraction vectors are coplanar.

The three-beam X-Ray diffraction condition can be fulfilled by rotating the sample around the primary diffraction vector $\vec{P}$ of the reflection whose intensity is monitored, generally a symmetric one. That is, secondary and cooperative reflections are excited only at some specific azimuthal angles φ_0 of the incident direction. This makes that this type of diffraction could be observed only for some particular azimuthal angles.

6.4.2 Hybrid multiple diffraction

Hybrid Multiple Diffraction (HMD) is a particular and poorly studied kind of multiple diffraction that can happen in heteroepitaxial systems. In these systems two different materials are involved in the

generation of MD in such a way that the secondary and cooperative planes belong to different reciprocal lattices. In this respect, the final beam is not diffracted exactly towards the outgoing primary direction (θ) but in a direction very close to it (θ_H). Thus HMD phenomenon can be observed also for allowed reflections unlike as happens with MD. One of the first studies in this frame was performed by Isherwood *et al.* [113], who investigated cubic $Ga_{1-x}Al_xAs$ epitaxially grown on (001) GaAs substrates. Later, it was studied by Morelhão *et al.* [114–118] and Domagala and coworkers [119] for different cubic and, ultimately, for wurtzite *c*-oriented materials.

In our case, the materials involved in the HMD process are the ZnO substrate and the $Zn_{1-x}Mg_xO$ layers. The usual vision of the reciprocal space of these systems is a superposition of both reciprocal lattices, one from the substrate and another from the layer. In this situation, if MD occurs exclusively within the substrate, or exclusively within the layer, the sums of diffraction vectors $\vec{S}$ and $\vec{C}$ always end up at a reciprocal-lattice point of the corresponding spaces. Figure 6.12(a) and (b) shows an example of MD for the case of a layer completely relaxed and completely stressed respectively.

When hybrid multiple diffraction happens, secondary and cooperative planes belong to different lattices, giving rise to a hybrid reciprocal space much more complex than just a superposition of the bare substrate/layer reciprocal spaces, as depicted in Figure 6.12(c) and (d). In reciprocal space these conditions lead to a hybrid diffraction vector $\vec{P}_H$ that can differ in magnitude, direction or both with respect to the primary one $\vec{P}$.

Figure 6.12(c) corresponds to a HMD system in which the epilayer is completely relaxed. It can be observed that the hybrid vectors near the symmetric reflection have different directions, but maintain a similar magnitude, exhibiting hybrid points at both sides of the out-of-plane axis. This case is equivalent to that treated by Morelhao *et al.* [118] for cubic ZnSe/GaAs (001) structures. In Figure 6.12(d) a scheme of reciprocal space is depicted when fully strained layers are considered. In this case there is a negligible change in the direction of hybrid diffraction vector, and layer, substrate and hybrid peaks are nearly aligned along the out-of-plane axis. This is similar to the situ-

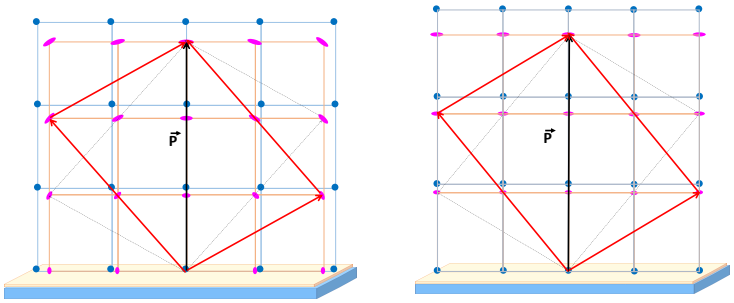

(a) MD in a relaxed layer (b) MD in a fully strained layer

(c) HMD in a relaxed layer (d) HMD in a fully strained layer

Figure 6.12: Scheme of a MD and HMD process in the reciprocal space map.

ation analyzed by Domagala *et al.* [119] with $Al_{0.14}Ga_{0.86}N$ epilayers grown on *c*-oriented GaN substrates.

In this context there are two different possibilities for the calculation of the hybrid primary vector $\vec{P}_H$:

$$\vec{P}_H = \vec{S}_L + \vec{C}_S \tag{6.4a}$$

$$\vec{P}_H = \vec{S}_S + \vec{C}_L \tag{6.4b}$$

The choice between 6.4a and 6.4b to determine $\vec{P}_H$ has to be done by comparing calculated and experimental values of both θ_H and φ_0 angles. (See Apendix A for information about the different equations involved in the HMD process.)

In our case, we have RSM exhibiting a distribution of points as in Figure 6.12(d), consequently satellite peaks P1-P8 observed in $2\theta - \omega$ scans of Figure 6.3 can be interpreted in the frame of a HMD, as an interactive process between the $Zn_{1-x}Mg_xO$ layer and the ZnO substrate. The behavior of hybrid peaks as a function of the Mg content depicted in Figure 6.3(d) can now be easily understood. $2\theta_H$ values of hybrid peaks converge towards the position of the ZnO peak since, for the limit case of 0% Mg, both secondary and cooperative reflections belong to the ZnO reciprocal space. That means that sums of diffraction vectors $\vec{S}$ and $\vec{C}$ shall end up at a reciprocal-lattice point so no extra features should be found.

6.4.3 Indexing of participating planes

As has been stated, in HMD there are two types of key angles, the azimuthal angle φ_0 and the Bragg angle $2\theta_H$ at which this special type of diffraction is observed. These values depend on the planes participating in the multiple diffraction process and its knowledge allows the accurate determination of other interesting values, as will be shown later. All the calculated values detailed in this paragraph have been obtained from equations given in Apendix A.

To prove that the satellite peaks previously found are in fact a consequence of HMD, we have carried out the indexation of planes that

are involved in their generation, and we have calculated the theoretical azimuthal φ_0 and Bragg $2\theta_H$ angles. Then we have confronted all these values with the experimental findings.

In order to determine the participating planes and the expected angles, all the kinematically allowed reflections (for the secondary and cooperative planes) were systematically investigated. Theoretical values of the Bragg ($2\theta_{theo}$) and azimuthal (φ_{theo}) angles at which HMD is expected were provided by eqn. A.10 and A.11, respectively. For the lattice constants needed in the calculations we used the mean values depicted in Table 6.2. Finally, the planes that matched better the experimental angles were selected. Table 6.4 displays these planes and their characteristic angles. In all the calculations the tilt and twist of the layer with respect to the substrate has been taken into account.

Five combinations of secondary and cooperative planes are found to explain the experimental hybrid peaks:

$$\begin{gathered}
\left(\bar{1}105\right)_S + \left(10\bar{1}\bar{3}\right)_L \\
\left(10\bar{1}5\right)_S + \left(\bar{1}10\bar{3}\right)_L \\
\left(0\bar{1}13\right)_S + \left(02\bar{2}\bar{1}\right)_L \\
\left(0004\right)_S + \left(01\bar{1}\bar{2}\right)_L \\
\left(0002\right)_S + \left(01\bar{1}0\right)_L
\end{gathered}$$

It has been found that, for a given azimuthal angle, different combinations of secondary-cooperative set of planes contribute to the same hybrid peak. More precisely, two at 0°, ±90° and 180° and three at ±60° and ±120°, as indicated in Table 6.4.

The low number of observed HMD peaks is not surprising, given the low symmetry of the system and the expected reduced intensities of MD reflections in ternary compounds, as they are extremely sensitive to the content of the alloy [105, 108].

The theoretical confirmation of the φ_0 angles at which HMD is observed can be seen in Figure 6.13(a) where the computed azimuthal positions at which HMD appears in sample S43 is shown as a function of the wavelength and taking into account all the previous sets of

Peak	$\vec{P} = \vec{S} + \vec{C}$	$Zn_{0.73}Mg_{0.27}O$				$Zn_{0.65}Mg_{0.35}O$				$Zn_{0.57}Mg_{0.43}O$			
		$2\theta_{exp}$ (FWHM)	$2\theta_{theo}$	φ_{exp} (FWHM)	φ_{theo}	$2\theta_{exp}$	$2\theta_{theo}$	φ_{exp}	φ_{theo}	$2\theta_{exp}$ (FWHM)	$2\theta_{theo}$	φ_{exp} (FWHM)	φ_{theo}
1	$(\bar{1}1.5)_S + (10.\bar{3})_L$		47.011	0.05	0.04		46.735	0.02	−0.27		46.522	−0.29	−0.44
	$(10.5)_S + (\bar{1}1.\bar{3})_L$		47.011	(1.11)	-0.04		46.735		0.27		46.523	(1.29)	0.44
2	$(0\bar{1}.3)_S + (02.\bar{1})_L$		47.020	61.36	62.02		46.692	60.97	62.01		46.531	59.88	62.00
	$(10.5)_S + (\bar{1}1.\bar{3})_L$		47.011	(1.06)	61.11		46.735		60.80		46.523	(1.01)	60.63
	$(00.4)_S + (01.\bar{2})_L$		47.061		61.34		46.797		61.19		46.613		61.12
3	$(02.\bar{1})_L + (0\bar{1}.3)_S$		47.020	119.10	117.94		46.692	120.34	118.02		46.531	118.83	118.00
	$(10\bar{3})_L + (\bar{1}1.5)_S$	47.005	47.011	(0.99)	118.88	46.80	46.735		119.35	46.486	46.522	(0.88)	119.48
	$(01.\bar{2})_L + (00.4)_S$	(0.052)	47.061		118.59		46.797		118.83	(0.052)	46.613		118.84
4	$(10.\bar{3})_L + (\bar{1}1.5)_S$		47.011	179.89	180.03		46.735	180.24	179.91		46.522	179.67	179.66
	$(\bar{1}1.\bar{3})_L + (10.5)_S$		47.011	(1.06)	−180.23		46.735		-179.91		46.523	(1.13)	-179.86
5	$(0\bar{1}.3)_S + (02.\bar{1})_L$		47.020	-61.12	-62.01		46.692	-60.05	-62.01		46.531	-61.17	-62.00
	$(\bar{1}1.5)_S + (10.\bar{3})_L$		47.011	(0.86)	-60.80		46.735		-60.80		46.523	(0.95)	-60.63
	$(00.4)_S + (01.\bar{2})_L$		47.061		-61.19		46.797		-61.19		46.613		-61.12
6	$(02.\bar{1})_L + (0\bar{1}.3)_S$		47.020	-119.10	-118.14		46.692	-119.36	-118.02		46.531	-120.04	-118.20
	$(\bar{1}1.\bar{3})_L + (10.5)_S$		47.011	(1.11)	-119.08		46.735		-119.35		46.522	(1.36)	-119.68
	$(01.\bar{2})_L + (00.4)_S$		47.061		-118.79		46.797		-118.83		46.613		-119.04
7	$(01.0)_L + (00.2)_S$		47.352	90.30	90.05		47.221	90.00	89.83		47.175	89.21	90.16
	$(00.2)_S + (01.0)_L$	47.350	47.352	(0.99)	89.90	47.24	47.221		90.18	47.172	47.175	(1.30)	89.80
8	$(01.0)_L + (00.2)_S$	(0.045)	47.352	-87.97	-90.25		47.221	-90.00	-90.18	(0.048)	47.175	-90.61	-90.36
	$(00.2)_S + (01.0)_L$		47.352	(0.98)	-89.90		47.221		-89.83		47.175	(1.30)	-89.80

Table 6.4: Sets of planes that contribute to each hybrid peak and their corresponding peak positions. Full Width at Half Maximum is shown in parenthesis. For the thinnest sample ($Zn_{0.65}Mg_{0.35}O$) FWHM could not be accurately determined. All the angles are given in degrees.

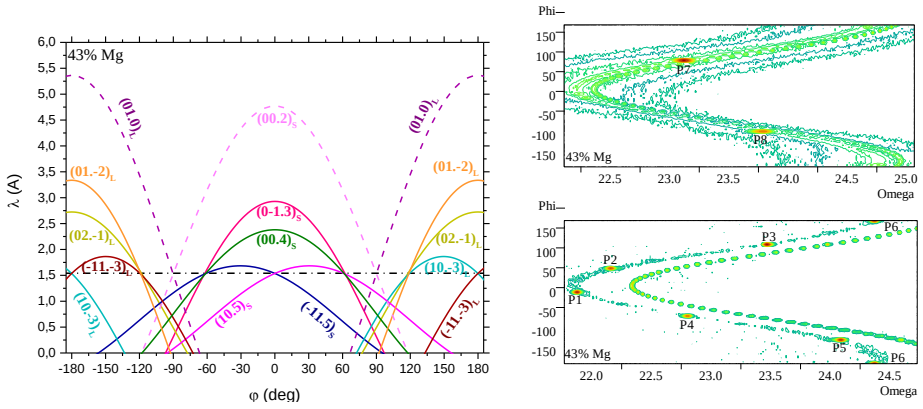

(a) (b)

Figure 6.13: a) Azimuthal positions at which HMD appears in sample S43 as a function of the wavelength for the considered set of planes. Solid/dashed line correspond to planes with 6-fold/2-fold symmetry respectively, horizontal dot-dashed line corresponds to Cu Kα_1 wavelength, b) phi/ω maps for hybrid peaks at both low and high Bragg angles. In both maps rocking curves around hybrid peak are made in steps of 5 degrees in the azimuthal angle.

planes. A two-fold symmetry around $\varphi = 0°$ can be observed due to the mirror symmetry of the wurtzite r-plane across the plane containing the c-axis. Obviously in higher-symmetry configurations, similar calculations give smaller azimuthal periodicities, concretely six-fold in c-wurtzite ZnO [107, 108, 120]. In our case, due to the low symmetry of the r-oriented wurtzite structure, the whole interval 0° to 180° has to be considered. It can be seen that the predicted azimuthal angles at which HMD is expected using the cupper $K\alpha_1$ wavelength are effectively 0°, ±60°, ±120° and 180° for P1-P6 peaks and at ±90° for peaks P7 and P8.

Hybrid peaks are best observed in φ/ω maps where Bragg angle is fixed and a rocking curve is performed around it for each phi angle. Figures 6.13(b) show these maps for sample S43 at both, low and high hybrid Bragg angles. Periodicity in φ of hybrid peaks is clearly seen, whereas the intensity associated to the substrate peak is observed whatever the azimuthal angle.

The calculated values for the azimuthal angles are given also in Table 6.4. For a given peak, the azimuthal spread of the calculated contributions span an azimuthal range of $\sim 1.4°$ or less. This range falls within the FWHM of the experimental peaks. Another factor that can contribute to this spread is the orthorhombic distortion, which might not be homogenous for all the thickness. Most importantly, calculated and measured azimuthal values coincide for all peaks.

When HMD takes place, the incidence and exit X-ray trajectories for a given combination of secondary and cooperative planes need not be at 180° azimuthally. These azimuthal deviations ($\Delta\varphi$) in the beam path can be calculated through eqns. A.11 (a) and (b) and are shown in Table 6.5. In all cases, the azimuthal deflection indicates a twist of the beam path towards the plane that contains the c-axis ($\varphi = 180°$), as shown in Figure 6.14. Again, the agreement between calculations and experiments is excellent.

Similarly, for a given azimuthal angle it can be seen that the different combinations of planes give rise to slightly different $2\theta_H$ values but, once again, the agreement between theoretically calculated values and measured ones is excellent. The combination of all of them gives rise to wide Bragg peaks. This is illustrated for peaks P3 and P7 in figure 6.15. In these maps the FWHM in Bragg angle (abscissa axis) is clearly smaller than the FWHM in the phi angle (ordinate axis). This behavior matches the theory, since the spread of theoretical $2\theta_H$ values for a given peak is much smaller than the corresponding spread for the azimuthal values, typically 0.1° against 1.4°. Besides, one should note that, while the X-ray beam is well conditioned in the diffraction plane, it is much less in the plane perpendicular to the diffraction one. This fact might further contribute to increase the azimuthal spread with respect to the one in 2θ.

6.4.4 Lattice parameters calculation from HMD

Once the occurrence of HMD has been demonstrated and planes involved have been determined, next we will show how this singular behavior has interesting and useful applications. Both lattice parameters (a and c) can be obtained by measuring just one RSM on a sym-

Planes $\vec{S}+\vec{C}$	Beam path	$Zn_{0.73}Mg_{0.27}O$		$Zn_{0.57}Mg_{0.43}O$	
		$\Delta\varphi_{exp}$	$\Delta\varphi_{theo}$	$\Delta\varphi_{exp}$	$\Delta\varphi_{theo}$
$(\bar{1}1.5)_S+(10.\bar{3})_L$	$0°/180°$	$0.16°$	$0.07°$	$0.04°$	$0.04°$
$(10.5)_S+(\bar{1}1.\bar{3})_L$			$0.27°$		$0.36°$
$(0\bar{1}.3)_S+(02.\bar{1})_L$			$0.17°$		$0.26°$
$(10.5)_S+(\bar{1}1.\bar{3})_L$	$60°/-120°$	$0.46°$	$0.20°$	$0.08°$	$0.37°$
$(00.4)_S+(01.\bar{2})_L$			$0.13°$		$0.22°$
$(0\bar{1}.3)_S+(02.\bar{1})_L$			$0.03°$		$0.06°$
$(\bar{1}1.5)_S+(10\bar{3})_L$	$-60°/120°$	$0.22°$	$0.00°$	$0.00°$	$0.05°$
$(00.4)_S+(01.\bar{2})_L$			$0.07°$		$0.10°$
$(00.2)_S+(01.0)_L$	$90°/-90°$	$0.27°$	$0.05°$	$0.18°$	$0.22°$
$(01.0)_L+(00.2)_S$			$0.15°$		$0.10°$

Table 6.5: Azimuthal deviations for the set of planes.

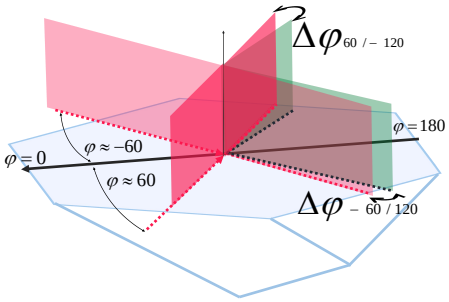

Figure 6.14: Scheme of the different paths in the $60°/-120°$ and $-60°/120°$ trajectories.

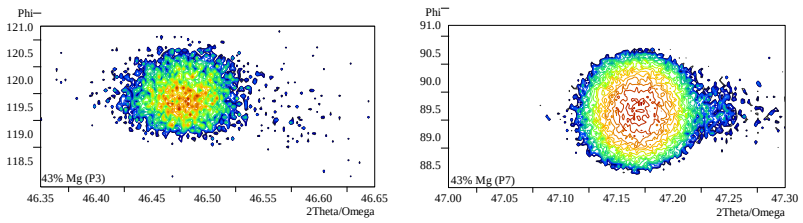

(a) (b)

Figure 6.15: $Phi/2\theta - \omega$ maps for sample S43 of peak around a) peak P3 and b) peak P7.

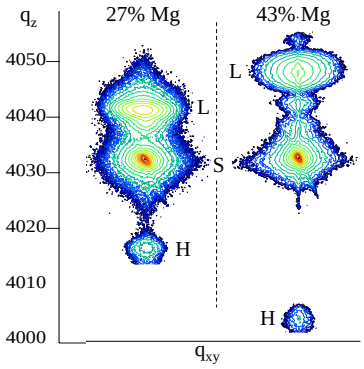

Figure 6.16: RSM of samples S27 and S43 measured at φ=90°, scan dimensions: 0.28 $\mathring{A}^{-1}$ in q_{xy} per 0.44 $\mathring{A}^{-1}$ in q_z

metric reflection exhibiting HMD, without the need of measurement of asymmetrical reflections. The method will be applied to $Zn_{1-x}Mg_xO$ layers grown on an r-oriented ZnO substrate but can be generalized to other orientations easily.

For this purpose it is enough to obtain a RSM of a symmetric reflection at an azimuthal angle at which a hybrid peak appears and in which substrate, layer and hybrid peaks are observed together. In our case, we have chosen the hybrid peak observed at $\varphi = 90°$ generated by planes $(00.2)_S$ and $(01.0)_L$ due to its relative large intensity. Figure 6.16 shows the RSM at $\varphi = 90°$ for samples S27 and S43.

Experimental method	$Zn_{0.73}Mg_{0.27}O$		$Zn_{0.57}Mg_{0.43}O$	
	a	c	a	c
RSM of (01.2) and (01.4) reflections	3.2580	5.1757	3.2683	5.1445
HMD of (01.2) reflection	3.2582	5.1731	3.2676	5.1446

Table 6.6: Calculated lattice parameters of samples using RSM and HMD. All the values are given in $\mathring{A}$ (± 0.0005 $\mathring{A}$).

Once this map is obtained, the analysis of the out-plane coordinates q_z for the layer and hybrid peaks will give the layer lattice parameters. This coordinate, for the point corresponding to the layer $q_z(01.2)_L$, is related to the lattice constants of the layer (a_L, c_L) through eqn. 6.1 [98]. On the other hand, eqn.6.4a and 6.4b give the relation between the measured coordinates for the hybrid peak and the lattice constants of substrate (a_S, c_S) and layer ($q_z(01.2)_H$=$q_z[(00.2)_S$+$(01.0)_L]$).

$$\left.\begin{aligned} q_z(01.2)_L &= 2\sqrt{\tfrac{1}{3a_L^2}+\tfrac{1}{c_L^2}} \\ q_z(01.2)_H &= \frac{2}{c_S^2\sqrt{\frac{1}{3a_S^2}+\frac{1}{c_S^2}}} + \frac{2}{3a_L^2\sqrt{\frac{1}{3a_L^2}+\frac{1}{c_L^2}}} \end{aligned}\right\} \tag{6.5}$$

As the lattice constants of the ZnO substrate are known, lattice constants of the layer can be obtained by solving the above system.

For the sake of comparison, Table 6.6 displays the calculated lattice constants for samples S27 and S43 using the typical combination of RSMs on symmetric and asymmetric reflections and those calculated from the experimental value of the hybrid Bragg angle and the procedure proposed here using high resolution HMD. As can be seen, by using the high-resolution HMD procedure described here both lattice parameters can be obtained with high accuracy (as large as that obtained by combining symmetric and asymmetric RSMs) and employing roughly half of the time.

Chapter 7

Conclusions

This chapter summarizes the main contributions of this work to the growth and characterization of nano- and microstructures of $Zn_{1-x}Mg_xO$ in the configuration of nanowires and thin layers respectively.

7.1 $Zn_{1-x}Mg_xO$ NWs

The search of ordered $Zn_{1-x}Mg_xO$ nanowires (NWs) has lead us to experiment with self-organized growth mechanisms. The selected method to grow these structures has been the vapor-solid (VS) method, which do not necessitate catalyst. The way to obtain ordered nanostructures has been the use of pellets, which act as substrates, patterned by means of Laser Induced Periodic Surface Structures (LIPSS). The main conclusions related to the growth of these $Zn_{1-x}Mg_xO$ NWs are detailed next.

- In order to found the best conditions for the VS growth, a previous study of the randomly growth of $Zn_{1-x}Mg_xO$ NWs was made, obtaining that the best conditions for this type of growth were a low time milling (5 h) of the precursor mixture and a content of 5 wt. Mg %. Out of these conditions low covered substrates and non-homogeneous distribution of NWs were found, joined to the presence of the binary compound MgO.

- The analysis of the optical properties of the randomly grown $Zn_{1-x}Mg_xO$ NWs has shown a narrowing of the Near Band Edge (NBE) band and a decreasing of the Deep Level (DL) band for increasing values of the Mg content.

- For obtaining patterned substrates, self-organized LIPSS structures have been fabricated by irradiation with a high repetition rate femtosecond laser on polycrystalline ZnO based samples. All samples were prepared in the previously determined best conditions for the growth process. The capability of the structured surfaces to serve as substrate template for the growth of low dimensional structures has been investigated, showing that the best regions to be used as growth templates are those irradiated in the highest energy deposition regime.

- On these patterned substrates, wires with large aspect ratios, arranged in arrays with the scanning line spatial period have been obtained after the VS growth. The luminescent characteristics of the so obtained $Zn_{1-x}Mg_xO$ nanostructures consisted mainly on an increasing of the DL band intensity in respect pure ZnO. This aspect is of great importance for the performance of ZnO-based sensing devices, since gas sensitivity in NWs was found to be strongly related to the luminescence intensity of the DL band.

7.2 $Zn_{1-x}Mg_xO$ thin layers

Given the high interest on $Zn_{1-x}Mg_xO$/ZnO microcavities (MCs) constituted by Distributed Bragg Reflectors (DBR) and based on nonpolar and semipolar ZnO, a careful study, mainly about their structural characteristics, has been developed. Thus, $Zn_{1-x}Mg_xO$ thin layers grown by Molecular Beam Epitaxy (MBE) have been analyzed in two different configurations, *m*-oriented $Zn_{1-x}Mg_xO$/ZnO systems (both single layers and multilayers) and *r*-oriented $Zn_{1-x}Mg_xO$/ZnO single layers, as building blocks for the achievement of MCs.

In the case of *m*-oriented microcavities the main conclusions are:

- $Zn_{1-x}Mg_xO$ single layers and complete MCs have been obtained with flat surfaces and interfaces confirmed by atomic force microscopy and high resolution X ray diffraction (HRXRD) measurements. Surface roughness has been studied as a function of the number of layers in the DBR and it has been proven that the roughness of these heterostructures raised as the total thickness increased, but with a lower raising rate than single layers do. Mg composition has been found to be homogeneous, even for heterostructures with a thickness in the range of micrometers. Despite these good qualities, samples thicker than 400 nm presented cracks along to $< 11.0 >$ in plane direction. Nevertheless, it has been proven that these cracks do not affect the macroscopic optical and structural properties of the system.

- HRXRD has shown that m-oriented layers were grown pseudomorphically, that is totally in-plane strained, exhibiting almost the same in-plane lattice parameters than the substrate. Measurements of the lattice parameters revealed the typical behavior of ZnO-MgO alloy, an increased lattice parameter a and a decreased lattice parameter c with respect to ZnO ones. In-plane measurements indicated a relatively high (-0.32%) compressive mismatch along the [11.0] in-plane direction and a relatively small ($+0.078\%$) tensile mismatch along the [00.1] in-plane direction, that could be the origin of cracks. Nevertheless, the high difference in the thermal expansion coefficients of the layer and the substrate could also contribute.

- When optical properties have been studied, it has been shown that the cathodoluminescence (CL) spectra of microcavities based on m-oriented multilayers are dominated by the NBE of ZnO, in company with a weak DL emission. These characteristics are indicative of a high NBE radiative efficiency and excellent optical properties. Reflectivity measurements show a high and wide stop band with a cavity mode centered at $2.94 - 2.96$ eV.

- As a culmination of all of the above, the possibility of stacking a large number of bilayers, together with the high contrast of index

in the DBR mirrors and their excellent structural properties, have enabled to obtain optical microcavities with quality factors in the order of 600 with a photonic disorder one order of magnitude smaller than the state-of-the-art in wide bandgap microcavities.

In the case of r-oriented microcavities, only the first step of the equivalent study made previously on m-oriented multilayers system has been carried out. Thus MBE growth conditions were first optimized for obtaining $(01\bar{1}2)$ $Zn_{1-x}Mg_xO/ZnO$ single layers and a deep study of the structural properties was carried out as a function of the Mg content. During the development of this study, satellite peaks in $2\theta - \omega$ scans were observed that gave us the opportunity of studying an unusual and barely studied case of multiple diffraction phenomenon called hybrid multiple diffraction (HMD) which is a consequence of the high crystalline quality of heterostructures. As far as we know, HMD has never been studied on systems with a symmetry as low as that of r-oriented wurtzite structures. The main conclusions obtained in this study are:

- Related to roughness, r-oriented layers also display flat surfaces, independently of the Mg content of the studied range. In addition, the samples showed no cracks even for thicknesses higher than 400 nm.

- HRXRD has shown that these layers were also pseudomorphic with respect to the substrate, independently of the Mg content of the studied range. These measurements revealed also that the lattice parameters follow the previously described as typical behavior of ZnO with Mg content. However they also bring out the fact that the basal plane had an orthorhombic distortion, with the gamma angle slightly higher than 120°, increasing this deviation with the increasing Mg content.

- Structural analysis of layers by HRXRD confirmed the good quality of layers, although exhibiting satellite peaks in $2\theta - \omega$ scans. The value of the Bragg angle at which these satellite peaks were observed $2\theta_H$ was dependent of the Mg content. These satellite

peaks could be interpreted in the frame of the HMD, a special kind of multiple diffraction in which the participating planes in the phenomenon belong to different lattices, in this case substrate and layer.

- Two sets of hybrid reflections were found, one exhibiting smaller $2\theta_H$ with an approximate six-fold azimuthal symmetry and the other one exhibiting a larger $2\theta_H$ with an approximate two-fold symmetry in the azimuthal angle. Interestingly, for these hybrid reflections the difference between forward and reverse beam path is not 180° azimuthaly.

- Planes that contribute to HMD were identified, finding five sets of planes which explain all the observed satellite peaks. This set of planes allow the calculation of the Bragg angles $2\theta_H$ and the azimuthal angles at which HMD appears, finding an admirably good agreement with experimental values.

- The analysis and the achieved angular precision leads us to propose a very interesting application of HMD, as is the accurate measurement of lattice parameters. This method provides an easy way to shorten the measurement time without sacrificing accuracy.

From a global point of view, this thesis has allowed, not only the aforementioned achievements, but also the acquisition of skills and wide knowledge on different growth and characterization techniques.

Appendix A

Multiple diffraction

MD arises when for a given incident beam there are more than one set of planes that fulfill simultaneously the Bragg condition. That is, when more than one lattice point lie on the Ewald sphere for an incident beam $\vec{k}_0$. When two sets of planes are involved (three beam diffraction), we will refer to them as primary and secondary, with diffraction vectors $\vec{P}$ and $\vec{S}$ respectively. In the current treatment the primary reflection will involve planes parallel to the surface of the sample (symmetric reflection), while the secondary reflection is related to planes tilted with respect to the surface (asymmetric reflections). In order to obtain the azimuthal angle at whih MD can be observed, we have to consider the Bragg conditions for primary and secondary reflections, which are respectively:

$$\vec{k}_0 \cdot \vec{P} = -\vec{P} \cdot \vec{P}/2 \tag{A.1}$$

$$\vec{k}_0 \cdot \vec{S} = -\vec{S} \cdot \vec{S}/2 \tag{A.2}$$

Since the secondary beam is diffracted by a third set of planes (cooperative planes with diffraction vector $\vec{C}$) towards the outgoing primary direction, we have:

$$\vec{P} = \vec{S} + \vec{C} \tag{A.3}$$

and the Bragg condition for the cooperative reflection is written as:

$$\vec{k}_0 \cdot \vec{C} = -\vec{C} \cdot \vec{C}/2 - \vec{C} \cdot \vec{S} \tag{A.4}$$

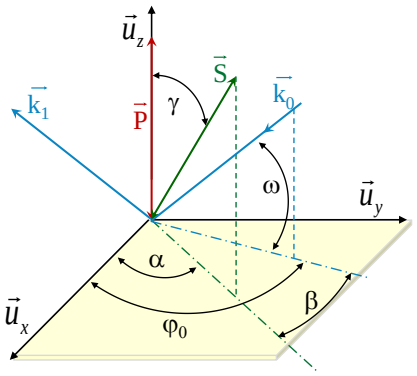

Figure A.1: Selected reference system.

First of performing any calculus, it is necessary to fix a reference system, as for instance, that one depicted in Figure A.1. The three-beam X-Ray diffraction condition can be fulfilled by rotating the sample around the primary diffraction vector $\vec{P}$. The secondary and co-operative reflections will be excited only at some specific azimuthal angles φ_0 of the incident direction. This angle can be calculated by entering $\vec{k}_0$ and $\vec{S}$ in the Bragg condition of the secondary planes, eqn. A.2

$$\vec{k}_0 = -\left|\vec{k}_0\right| \left[\cos\omega_0 \cos\varphi_0 \vec{u}_x + \cos\omega_0 \sin\varphi_0 \vec{u}_y + \sin\omega_0 \vec{u}_z\right] \tag{A.5}$$

$$\vec{S} = \left|\vec{S}\right| \left[\sin\gamma \cos\alpha\, \vec{u}_x + \sin\gamma \sin\alpha\, \vec{u}_y + \cos\gamma \vec{u}_z\right] \tag{A.6}$$

$$\cos\beta = \frac{\lambda \left|\vec{S}\right| /2 - \sin\omega_0 \cos\gamma}{\cos\omega_0 \sin\gamma} \tag{A.7}$$

$$\varphi_0 = \alpha \pm \beta \tag{A.8}$$

where λ is the wavelength of the X-ray beam, ω_0 the incidence angle for the primary reflection, γ is the angle between the primary and secondary diffraction vectors and α is the angle between the in-plane projection of the secondary diffraction vector and a reference

direction. The aforementioned φ_0 must be computed with respect to the same reference direction. Then, the expected direction between the incidence and the reference direction in which MD can be observed is given by $\varphi_0 = \alpha \pm \beta$.

When HMD happens, the final beam is not diffracted exactly towards the outgoing primary direction (θ) but in a direction very close to it (θ_H). In this case, secondary and cooperative planes belong to different lattices. The secondary planes can belong to the substrate reciprocal lattice (S) or to the layer lattice (L). As well can happen with the cooperative planes. Consequently there are two different possibilities for the calculation of the hybrid primary vector:

$$\vec{P}_H = \vec{S}_L + \vec{C}_S \tag{A.9a}$$

$$\vec{P}_H = \vec{S}_S + \vec{C}_L \tag{A.9b}$$

The Bragg angle of hybrid peaks (θ_H) can be calculated in the framework of the previous analysis by applying the Bragg law to the diffraction vector $\vec{P}_H$:

$$\frac{2}{|\vec{P}_H|} \sin\theta_H = n\lambda \tag{A.10}$$

The choice between A.9a and A.9b to determine $\vec{P}_H$ has to be done by comparing calculated and experimental values of φ_0 and θ_H angles.

For each hybrid peak, the incident azimuthal angle φ_0 at which HMD is expected is given also by eqn. A.7. It is worth to notice that in the case of MD, for each combination of secondary and cooperative planes, the same result is found after a rotation of 180 degrees around the primary vector, i.e., the forward and reverse paths for a given combination of secondary and cooperative planes are the same. However in HMD, since the planes involving the HMD process belong to different materials, it is not the same if the first diffraction (that is, the diffraction produced by the secondary planes) takes place in the substrate or in the layer. Thus, the forward and reverse paths for a given combination of secondary and cooperative planes are different (see Figure A.2). This results in an azimuthal angular difference, which we compute as

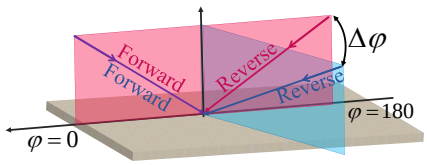

Figure A.2: Sketch of the different trajectories for a MD process (pink) and a HDM one (blue).

$180 + \Delta\varphi$. The azimuthal difference between both trajectories can be calculated as $\Delta\varphi = \beta - \beta'$, where:

$$\cos\beta = \frac{\lambda \left|\vec{S}_S\right| /2 - \sin\omega\cos\gamma_S}{\cos\omega\sin\gamma_S} \tag{A.11a}$$

$$\cos\beta' = \frac{\lambda \left|\vec{S}_L\right| /2 - \sin\omega\cos\gamma_L}{\cos\omega\sin\gamma_L} \tag{A.11b}$$

This calculation method is easier than those used in other studies [110, 117, 118] where authors calculate the incidence conditions in a hybrid system by solving a two equations system.

List of Figures

List of Tables

Part II

Spanish summary

Resumen en español

Algunos de los acrónimos empleados en este resumen provienen de las siglas en inglés del término en cuestión. En algunas ocasiones se emplea ZnMgO en lugar de $Zn_{1-x}Mg_xO$ para aligerar la lectura, dando la información del contenido de magnesio por separado.

Dentro de la creciente investigación en el área de la física de semiconductores, los pertenecientes a la familia II-VI se han convertido en un campo fundamental de la física de materiales debido a que sus propiedades fotofísicas son únicas para crear una nueva generación de dispositivos en el campo de la fotónica y la microelectrónica. Entre ellos los semiconductores basados en ZnO han ganado un considerable interés debido a varias razones. Por un lado, el ZnO tiene una alta energía de enlace excitónica, la cual es 2.4 veces mayor que la energía térmica a temperatura ambiente, lo cual podría dar lugar a emisión laser excitónica a temperaturas incluso mayores que la ambiente. Por otro lado, tiene un alto punto de fusión y una alta energía de enlace, por lo que es de esperar que la degradación del material durante su uso en dispositivos sea baja. Finalmente, sus elementos constituyentes son abundantes, no son tóxicos y son de bajo coste.

Las aplicaciones del ZnO son muy variadas en los distintos tipos de dispositivos. Muchos de ellos, como por ejemplo los emisores de luz, los detectores de luz ultravioleta (UV), los emisores superficiales de cavidad vertical..., están basados en el crecimiento sobre diferentes sustratos de capas epitaxiales, las cuales deben tener unas propiedades morfológicas y estructurales de una calidad extrema [1–4]. Cuando pasamos al rango nanométrico aparecen nuevas propiedades mecánicas, químicas y ópticas que pueden ser explotadas para el diseño de dispo-

sitivos. En particular, las estructuras 1D de ZnO tales como nanohilos (NHs) y nanovarillas han sido extensamente estudiadas para aplicaciones como detectores químicos, células solares, diodos emisores de luz azul y UV, almacenadores de hidrógeno y otras aplicaciones biomédicas [5–10].

Las propiedades del ZnO tales como el gap, los parámetros de red, el índice de refracción..., se pueden variar a través de aleaciones con otros materiales. Entre otras, la aleación ZnO-MgO ha atraído una especial atención debido a la alta similitud entre los radios iónicos del Zn y el Mg (Zn^{2+} (0.60Å) and Mg^{2+} (0.57Å)) [11], lo que podría dar a pensar que el ZnMgO es un semiconductor fácil de obtener. Sin embargo, ambos materiales poseen estructuras diferentes, el ZnO es hexagonal mientras que el MgO es cúbico y además, el límite de solubilidad del Mg, aunque depende del método de crecimiento, es bastante bajo en condiciones de equilibrio termodinámico (en torno al 4% [12]). Estos dos inconvenientes hacen que la obtención de aleaciones monocristalinas de alta calidad de ZnMgO sea un verdadero reto.

Desde un punto de vista práctico, las estructuras usadas en los dispositivos convencionales no pueden dar respuesta a la alta demanda tecnológica actual, por lo que es necesario adoptar configuraciones más sofisticadas que puedan dar lugar a una nueva generación de dispositivos. En este sentido, los NHs y las multicapas presentan un gran interés, dado que estas configuraciones forman parte de la mayoría de los dispositivos modernos.

El crecimiento de NHs de $Zn_{1-x}Mg_xO$ ha sido extensamente estudiado, mediante el uso de diferentes métodos de crecimiento tales como la deposición química metalorgánica en fase de vapor (MOCVD), deposición por láser pulsado (PLD), epitaxia por haces moleculares (MBE), vapor-liquido-solido (VLS), vapor-solido (VS)... [13–25]. En el caso concreto de NHs ordenados, cuyas ventajas son bien conocidas [26] la técnica mas típicamente empleada es la de VLS. Esta técnica permite obtener NHs alineados y a su vez, controlar su diámetro y posición a través de las partículas catalizadoras previamente depositadas. Éstas, dirigen y confinan el crecimiento cristalino a una orientación y espacio definido. El crecimiento está asistido por la presencia de una interfase líquida/sólida en la que la partícula atrapa reactivo hasta que se pro-

duce una sobresaturación, momento en que comienza el crecimiento del cristal. El inconveniente de este método es la contaminación por impurezas que puede provocar el uso de catalizadores, por lo que es necesario explorar otras alternativas. Otro modo para controlar los puntos de nucleación, consiste en el uso de sustratos grabados con algún patrón. Frente al tedioso proceso que supone la litografía, la estructuración superficial a través de la irradiación con láseres pulsados ultracortos supone una alternativa para producir los patrones. Esta irradiación genera los conocidos LIPSS, de sus siglas en inglés *Laser Induced Periodic Surface Structures*. Uno de los primeros trabajos en este campo fue realizado por Birnbaum en 1965 [27] sobre diferentes semiconductores monocristalinos, y lo consideró como un efecto causado por la difracción en el foco de la lente del sistema. Desde entonces, se han desarrollado muchas teorías diferentes que intentan dar una explicación al motivo por el cual aparecen los patrones [28–31], aunque aún no se ha llegado a una teoría completa que pueda explicarlo. Sin embargo, se ha demostrado que los patrones originados mediante esta ténica favorecen el crecimiento de nanoestructuras ordenadas [32]. En la mayoría de los estudios que se pueden encontrar en la bibliografía, se utilizaron muestras monocristalinos [30,33] mientras que el uso de sustratos policristalinos, con las ventajas que supone en cuanto al coste, no ha sido muy extensamente estudiado [32,34].

En este sentido uno de los objetivos de esta tesis es la obtención y caracterización de nanohilos ordenados mediante un método facilmente accesible y de bajo coste, el método VS y utilizando sustratos policristalinos grabados.

Respecto al crecimiento de capas eitaxiales de $Zn_{1-x}Mg_xO$, debido a la alta calidad necesaria para integrarlas en dispositivos fotónicos, generalmente se utilizan sofisticadas ténicas para su obtención, tales como MBE, PLD y MOCVD [35–44]. El rápido desarrollo de estas téncnicas de crecimiento durante el último siglo ha permitido la obtención de estructuras con interesantes propiedades ópticas. Entre otras, las microcavidades (MCs) ofrecen una alto confinamiento óptico en un pequeño volumen y son buenas candidatas para alcanzar un acoplamiento fuerte luz-materia [45]. En estas estructuras, los polaritones de la cavidad, es decir, las quasipartículas resultantes del

acoplamiento fuerte entre excitones y los fotones confinados en la cavidad, pueden dar lugar al condensado de Bose-Einstein y emitir luz coherente, obteniendo así los llamados láseres polaritónicos [46, 47]. Como en estos dispositivos no se necesita inversión de poblaciones, es de esperar que la corriente umbral sea menor que para los láseres convencionales. La condición necesaria para que estos láseres puedan pasar de un simple prototipo de laboratorio, a un dispositivo real, es que puedan ser usados a temperatura ambiente (TA). Para ello es necesario que el semiconductor en el que esté basado el láser tenga una gran enegía excitónica y que la fuerza del oscilador sea alta, lo que hace del ZnO uno de los mejores candidatos [48,49]. Por ello en los últimos años se ha dedicado un gran esfuerzo al estudio del acoplamiento fuerte en MCs de ZnO así como en la fabricación de láseres polaritónicos basados en ZnO [50–57]. Estas complejas estructuras se fabrican embebiendo una capa de ZnO, llamada medio activo, entre dos espejos, generalmente reflectores de Bragg distribuidos (DBR) dada su alta reflectividad. Los DBR consisten en una multicapa formada por dos materiales que deben de cumplir dos condiciones; deben de tener un alto contraste de índice de refracción y además un bajo desajuste de red, tanto entre ellos como con el ZnO. Es aquí donde las capas de $Zn_{1-x}Mg_xO$ cumplen el papel protagonista ya que sus parámetros de red y sus índices de refracción (tiene dos dado que es un materal birefringente) pueden ser ajustados en función de la cantidad de Mg en la aleación. Por tanto se pueden conseguir altas reflectividades sin sacrificar por ello la calidad de la microcavidad.

La mayoría de los trabajos publicados en este campo hasta el comienzo de esta tesis estaban basados en ZnO orientado (00.1), con todos los inconvenientes que ello supone, sobretodo si se desea utilizar pozos cuánticos como medio activo. El carácter polar de esa orientación da lugar al efecto Stark cuántico con la consecuente pérdida de eficiencia del dispositivo. Por ello es preferible obtener las MCs con orientaciones no polares o semipolares. En cuanto al sustrato a utilizar, aunque el zafiro sea el más común para crecer ZnO, en el caso de orientaciones no polares da lugar a altas concentraciones de defectos [59–61].

Así pues, el segundo objetivo de esta tesis es profundizar en el estudio de sistemas $Zn_{1-x}Mg_xO$/ZnO no polares y semipolares crecidos sobre sustratos de ZnO mediante MBE con el fin de obtener MCs de alta calidad.

Por todo lo explicado anteriormente, el objetivo de esta tesis es profundizar en algunos aspectos relacionados con un material tan interesante como la aleación de ZnO-MgO, cubriendo así algunas de las deficiencias encontradas en la bibliografía. Dichos aspectos comprenden desde el crecimiento de la aleación hasta su integración en estructuras más complejas. Así pues, se han abordado dos frentes, primero, el crecimiento de nanohilos ordenados de $Zn_{1-x}Mg_xO$ por el método de vapor-sólido sin el uso de catalizador, sobre pastillas policristalinas con patrones en forma de LIPPS. Y segundo, el crecimiento y la caracterización de microcavidades ZnO de alta calidad, con orientaciones m- y r-, usando diferentes configuraciones en los DBRs $Zn_{1-x}Mg_xO$/ZnO.

Capítulo 2

El capítulo 2 resume las propiedades más importantes del material que es objeto en esta tesis, el $Zn_{1-x}Mg_xO$ así como de los binarios que le dan lugar, el ZnO y el MgO. También se da una breve descripción sobre los métodos de crecimiento empleados.

El ZnO es un semiconductor de la familia II-VI, su fase más estable es la wurtzita, de estructura hexagonal. Sus parámetros de red reportados en la bibliografía varían ligeramente según la fuente, pero están en el rango a=$3.2475 - 3.2501$ Å y c=$5.2042 - 5.2075$ Å [1]. Debido a la baja simetría de la estructura y a la diferencia de electronegatividad entre el O y el Zn, hay una polarización espontánea a lo largo del eje c, llamado también eje polar. Este campo eléctrico interno se puede reducir o incluso anular en otras orientaciones, como las no polares (a- y m-) o semipolares (como la r-) respectivamente. En lo referente a sus propiedades ópticas, es un material birrefringente positivo, tiene tres sub-bandas de valencia como resultado del campo cristalino y la interacción spin-órbita y posee un gap directo de ~ 3.36 eV a temperatura ambiente, lo que le hace interesante para su uso en dispositivos que operen en el azul-UV. Su espectro luminiscente se puede dividir en

dos regiones bien distinguidas, una en el rango $2.95 - 3.37$ eV y otra en $1.5 - 2.95$ eV. La primera se corresponde con defectos poco profundos, el gap, transiciones excitónicas y réplicas del acoplamiento de los excitones con fonones de la red. A medida que aumenta la temperatura, los excitones ligados se ionizan debido a la energía térmica y los excitones libres dominan la emisión. En estas circustancias, los electrones y huecos están libres en sus respectivas bandas y pueden recombinarse emitiendo un fotón, proceso llamado recombinación banda-banda. Debido a que la energía de enlace excitónica del ZnO es relativamente alta ($\sim$ 60 meV) comparada con la energía térmica a temperatura ambiente ($\sim$ 25 meV), el ZnO es un buen candidato para dar lugar a láseres polaritónicos.

La otra región, la comprendida entre 1.5 y 2.95 eV, está asociada a defectos. Si bien no hay un consenso sobre qué da origen a esta ancha banda, la mayoría de estudios la atribuyen a diferentes sub-bandas debidas a diferentes tipos de defectos, siendo las vacantes de oxígeno, vacantes de zinc y átomos de óxigeno intersticial los más reportados.

En cuanto al MgO, es un semiconductor de gap directo de 7.7 eV. Su fase más estable es la sal de roca, estructura cúbica de parámetro de red $a = 4.211$ Å [70]. El alto gap de este semiconductor hace que sea posible cubrir un amplio rango de energías de emisión mediante su aleación con el ZnO. En este sentido, y en lo referente a la estructura, se han reportado cantidades mayores al 50% de Mg [121] sin que se producta la separaración de fases. En la fase hexagonal, la incorporación del Mg a la red del ZnO produce un incremento en el parámetro de red a y una disminución en el c [43]. Los índices de refracción de la aleación (también birrefringente positiva) se pueden variar en función del contenido de magnesio en la red [36].

Respecto de los métodos de crecimiento, el método VS es un buen método para la obtención de nanoestructuras auto-ordenadas. Consiste en la evaporación de la fuente para su depósito sobre un sustrato, utilizando para ello un horno horizontal de temperatura controlada. Con el fin de optimizar los parámetros de crecimiento, antes de abordar el caso de nanohilos ordenados se han probado distintas condiciones para el caso de nanohilos desordenados. Para ello se ha utilizado una configuración consistente en una pastilla prensada de unos 7 mm de

diámetro constituída por diferentes mezclas de ZnS y MgO, la cual actúa como sustrato y fuente, proporcionando el crecimiento de las nanoestructuras sobre su superficie. Para el caso de nanohilos ordenados, como sustrato se ha utilizado una pastilla similar a las anteriores en cuya superficie se grabó un patrón, rodeada de dos pastillas fuente. El grabado del motivo se ha realizado mediante irradiación con un laser pulsado ultracorto, en el rango del femtosegundo, el cual induce una estructuración periódica de la superficie (LIPSS).

Para el crecimiento de capas y multicapas se ha empleado el método MBE. La epitaxia por haces moleculares es una técnica idónea en el crecimiento de heteroestructuras de semiconductores debido a la gran perfección cristalina que proporciona. El crecimiento se produce en condiciones de ultra alto vacío, asegurando así que los átomos de los materiales precursores no interactúen entre ellos ni con otros gases presentes en el interior de la cámara de vacío. Esto es posible gracias al elevado camino libre medio de los átomos conseguido mediante el vacío. La velocidad de crecimiento es aproximadamente 1 nm/sec lo que permite la variación gradual de la composición del material. Los materiales precursores (Zn y Mg en esta tesis) están contenidos en celdas de efusión, donde se realiza su evaporación térmica controlada y pueden ser abiertas/cerradas de manera electónica. En el caso del oxígeno, se utiliza una fuente de plasma de oxígeno activado con radio frecuencia, junto a un controlador de flujo.

Los sustratos se colocan en un portamuestras, de temperatura controlable y que puede ser continuamente rotado, con el fin de adquirir mayor homogeneidad en el depósito.

Capítulo 3

En el capítulo 3 se explican brevemente las técnicas de caracterización utilizadas en esta tesis. Para el estudio morfológico de las muestras se ha empleado microscopía electrónica de barrido (SEM) combinada con microscopía de fuerza atómica (AFM) en el caso de las capas. En el SEM, un haz de electrones acelerado y focalizado barre la muestra punto a punto, dando lugar entre otras señales, a electrones secundarios. Estos son electrones de baja energía generados por la interacción

inelástica del haz incidente con la muestra y proporcionan información sobre su morfología superficial. Dependiendo de las condiciones de la medida se puede llegar hasta la resolución de unos pocos nm. En cuanto al AFM utiliza como sonda una punta colocada en el extremo de un cantilever que rastrea la muestra vibrando a su frecuencia de resonancia. La variación de la amplitud de oscilación de la punta, debida a los cambios en la topografía de la superficie es lo que se utiliza como señal de control. Aunque el área de análisis del AFM es muy pequeña comparada con la del SEM, la resolución es subnanométrica.

Entre las otras señales que genera el SEM, se han empleado los rayos X para analizar la composición de las muestras, identificar los elementos presentes y establecer su concentración y los fotones para analizar su luminescencia. En las medidas de microanálisis, el haz de electrones primario arranca electrones de capas internas. Cuando otro electrón de capas superiores decae a la posición libre emite la diferencia de energía en forma de radiación X. La intensidad de los rayos X emitidos se representa en función de su longitud de onda o en función de su energía (EDX). En las medidas de catodoluminiscencia (CL) el haz primario genera miles de pares electrón-hueco en la muestra que, al recombinarse radiativamente, provoca la emisión fotones. La señal de CL es el resultado de todos los procesos radiativos debidos a la estructura de bandas, impurezas, defectos... por lo que se puede obtener información sobre su gap y algunos tipos de defectos.

Finalmente la información sobre la estructura se ha obtenido mediante difracción de rayos X de alta resolución (HRXRD). A diferencia de los difractómetros de polvo permite girar la plataforma portamuestras según diferentes ángulos por lo que es posible obtener información no sólo en la dirección perpendicular de la muestra sino también en muchas otras. En términos generales, los efectos de difracción se pueden observar cuando radiación electromagnética de longitud de onda λ incide en una estructura periódica con variaciones geométricas en el mismo orden de escala. Los electrones difractan dicho haz en todas las direcciones produciéndose interferencia constructiva unicamente en aquellas direcciones en las que se cumple que el camino seguido por los diferentes rayos difiere en un múltiplo entero de longitudes de onda. Se representa la intensidad en función de uno (barrido)

o dos (mapa) variables, que puede ser coordenadas traslacionales o rotacionales. De la posición de los picos se puedes extraer información del tipo y tamaño de la estructura, así como de las fases presentes, mientras que de la forma de los picos se puede deducir la calidad cristalina de la muestra.

Capítulo 4

El capítulo 4 está dedicado al crecimiento y caracterización de nanohilos ordenados de $Zn_{1-x}Mg_xO$. Se han utilizado diferentes condiciones para la producción de las pastillas, con el fin de ver cuál es la óptima para conseguir una alta densidad de nanohilos con buenas propiedades ópticas. Los precursores empleados para formar las pastillas son mezclas de ZnS y MgO en distintas proporciones (1.2, 5.7 y 18.9 % atómico de Mg) que son molidas durante 5 o 15 horas. El motivo de usar ZnS en lugar de ZnO es que gracias a su menor presión de vapor, se necesita menos cantidad de material evaporado para favorecer la supersaturación y por tanto permite obtener los mismos resultados a menor temperatura y con menor tiempo de crecimiento [76–79].

Sólo las mezclas molidas durante 5 horas dieron lugar a nanohilos. Las muestras consisten en un total recubrimiento de la superficie por NHs desordenados, con grosores entre 50 y 150 y algunos ramilletes de NHs. El número de ramilletes y la longitud de los NHs que los forman aumenta con el contenido de Mg en la mezcla original. Los NHs pertenecientes a estos ramilletes tienen forma escalonada (telescópica), su longitud es de ~ 40 μm. El contenido de magnesio de estas muestras medido por EDX es bajo, entorno a 7.2% atómico para la muestra con 18.9% nominal y cerca del límite de resolución para la muestra con 5.7%. No se detectó Mg en la muestra de menor porcentaje nominal, por lo que fue descartada para posteriores análisis.

En cuanto a las características estructurales se ha visto que la muestra con alto contenido en Mg presenta la fase cúbica del MgO. Con el fin de estudiar la luminiscencia de los NHs y eliminar la posible contribución del resto de la pastilla, estos fueron rascados y transferidos a sustratos de Si. Las medidas de micro PL a temperatura ambiente muestran una emisión dominante cercana al borde de banda centrada

en 3.26-3.29 eV. En lo referente a la banda de defectos se aprecia una notable disminución en intensidad a medida que aumenta el contenido nominal de Mg. Esta banda está asociada entre otras cosas a vacantes de oxígeno, como se dijo en el capítulo 2, por lo que asociamos el comportamiento de la banda al aporte de oxígeno proviniente del MgO en la mezcla. A pesar de que la muestra de mayor porcentaje de Mg presenta mejores propiedades ópticas, ésta da lugar a una fase detectable cúbica de MgO, por lo que finalmente se eligió la mezcla de 5.7% Mg at. molido durante 5 horas para formar las pastillas. Estas pastillas son utilizadas como fuente en el crecimiento de NHs ordenados, mientras que el sustrato consiste en una pastilla irradiada formada por una mezcla de ZnO y MgO (4.8% Mg at.) molida durante 5 horas.

Cada sustrato presenta 3 cuadrados, de unos 4 mm^2, donde se han aplicado diferentes condiciones de irradiación, dando lugar a los LIPSS, con un periodo de repetición consistente con lo que predice la teoría. Las condiciones de irradiación se corresponden con tres regímenes de energía depositada (por orden creciente, E1, E2 y E3). El spot es de unas 20 μm de diámetro y la irradiación se lleva a cabo a lo largo de líneas separadas unas 15 μm, lo que produce una periodicidad espacial de zonas solapadas. El resto de la pastilla, no irradiada, constituye la cuarta zona de interés.

En cuanto a las características estructurales de los sustratos, no se aprecian diferencias entre las cuatro zonas, pero sí se ve un ligero desplazamiento de los picos de difracción si se compara con muestras puras de ZnO procesadas en las mismas condiciones. Los parámetros de red obtenidos son ($\pm$0.005 Å) a_{ZnO} = 3.2526 Å, a_{ZnMgO} = 3.2566 Å, c_{ZnO} = 5.2068 Å and c_{ZnMgO} = 5.2097 Å. El ligero aumento del parámetro c del ZnMgO va en contra de lo obtenido generalmente en este tipo de aleaciones, por lo que probablemente el Mg ocupa lugares intersticiales en la red del ZnO en lugar de sustitucionales.

En lo referente a las propiedades luminiscentes de los sustratos se aprecian diferencias tanto entre las zonas irradiadas como entre las muestras de ZnO puras y las de ZnMgO. La presencia del MgO en la mezcla produce el mismo comportamiento que en los NHs desordenados, en las 4 zonas se ve un decrecimiento de la banda asociada a defectos. Analizando la influencia en esta banda de las zonas irradi-

adas respecto de la zona no irradiada, se ve un ligero aumento para la condición E1 y una disminución para E2 y E3. Esto puede explicarse como un aumento de defectos producido por una irradiación de baja energía, acompañado de un proceso de recocido y recristalización a medida que la energía aumenta, lo que hace disminuir la intensidad de la banda de defectos.

Las pastillas irradiadas de ZnO fueron sometidas a procesos VS de distintos tiempos de duración, $10, 5$ y 1 h. Para altos tiempos de crecimiento, las zonas irradiadas no son apenas distinguibles desde un punto de vista morfológico, por lo que se decidió usar como tiempo de crecimiento 1 hora para los nanohilos de ZnMgO. La mejor zona para el crecimiento de NHs ordenados es la irradiada con mayor energía, resultando en filas de NHs ordenados a lo largo de la línea de irradiación. Algunas estructuras con forma de colmena aparecen entre dichas líneas. Estas zonas se corresponden con las zonas de solapamiento anteriormente citadas, por lo que el crecimiento de estas estructuras podría estar relacionado con una mayor densidad de puntos de nucleación resultante de una mayor cantidad de material arrancado y repositado. Este efecto es mayor en las muestras de ZnMgO que en las de ZnO probablemente debido a una mayor rugosidad en las pastillas sustrato de partida.

En cuanto a las características ópticas, la presencia del Mg produce un incremento de la banda de defectos en las tres zonas irradiadas. Este aumento también se observa individualmente en las muestras de ZnO puro y ZnMgO si se comparan las zonas irradiadas con la no irradiada.

Este es un aspecto de gran importancia para la obtención de dispositivos basados en el ZnO, ya que la sensibilidad de los NHs a los gases está fuertemente relacionada con la intensidad de la banda de defectos.

Capítulo 5

El capítulo 5 está dedicado principalmente a la caracterización de microcavidades (MCs) no polares de ZnO embebidas entre reflectores de Brag distribuidos (DBR) de $Zn_{1-x}Mg_xO$/ZnO. Se ha visto que tanto para capas individales, como para estructuras con diferente número de

bi-capas, la rugosidad de la superficie crece a medida que aumenta el grosor total de la muestra. El contenido de Mg es homogéneo a lo largo de toda la heterostructura. Debido a la diferencia en los parámetros de red entre las bi-capas, las estructuras están tensionadas a lo largo de la dirección [00.1] y comprimidas a lo largo de [11.0]. Este hecho, sumado a la diferencia en los coeficientes de expansión térmica entre los distintos materiales, da lugar a la aparición de fisuras. Estas se distribuyen a lo largo de $< 11.0 >$ y de forma perpendicular a la superficie, atravesando la totalidad de la heterostructura e incluso penetrando en el sustrato. A pesar de ello, las medidas de difracción de rayos X sugieren que las muestras están uniformemente tensionadas. Esto se debe al gran tamaño del spot del haz, que no permite hacer medidas de micro-difracción para poder evaluar la relajación en el entorno de la fisura.

La caracterización óptica muestra que las capas y multicapas emiten predomidantemente en la banda cercana al gap, siendo la banda de defectos que se aprecia en las capas individuales atribuible al sustrato.

En cuanto a la caracterización del factor de calidad de la cavidad (Q), se ha visto que la posibilidad de producir muestras con un alto contenido de bi-capas en los DBR ha permitido alcanzar Qs $\sim$ 600, siendo este valor homogéneo a largo de la MC, revelando de nuevo la alta homogeneidad y calidad de las hereostructuras.

Capítulo 6

El capítulo 6 está dedicado al crecimiento y caracterización de capas epitaxiales individuales de de $Zn_{1-x}Mg_xO$ con orientación semipolar - r sobre sustratos de ZnO, con el fin de encontrar las condiciones de crecimiento adecuadas para en un futuro, formar MCs al igual que en el capítulo anterior. En este capítulo se analizan tres muestras consistentes en capas epitaxiales con diferentes grosores y diferentes contenidos de magnesio. Desde un punto de vista morfológico, no podemos correlacionar la rugosidad de la superficie con el grosor de la muestra, puesto que tienen diferente contenido de Mg. Sin embargo, los valores obtenidos se encuentran dentro del rango de los reportados en el capítulo anterior para las capas orientadas m-. En cuanto a las

propiedades estructurales, las muestras se encuentran tensionadas, lo que da lugar a una deformación del plano basal y se ha visto que esta deformación crece a medida que aumenta el contenido de Mg en la muestra. Las medidas ópticas revelan una emisión predominante en la banda cercana al gap, mientras que la banda de defectos que se observa en algunas medidas se puede asociar al sustrato.

En estas muestras se ha encontrado un efecto relacionado con la difracción múltiple (MD) de rayos X, poco conocido, llamado difracción múltiple híbrida (HMD). La MD se produce cuando para una determinada incidencia, más de un conjunto de planos está en condiciones de difractar. El set de planos paralelos a la superficie (reflexión simétrica) suele ser llamado primario mientras que el que está inclinado respecto a ésta se le llama secundario. La radiación difractada por los planos secundarios es a su vez difractada por un tercer conjunto de planos (llamado cooperativo) en la misma dirección que el primario (el mismo ángulo de Bragg, θ). Dado que experimentalmente no se puede diferenciar qué parte de la radiación medida proviene de los planos primarios y cuál del efecto conjunto de secundarios y coperativos, este efecto suele medirse para reflexiones primarias prohibidas o de muy baja intensidad. A diferencia de la difracción simétrica, la MD solo se da en determinadas posiciones del ángulo azimutal (φ_0). En el caso de la HMD los planos secundarios y cooperativos pertenecen a materiales distintos (ZnMgO de la capa y ZnO del sustrato en nuestro caso) por lo que el efecto conjunto de ellos ya no se produce exactamente al mismo ángulo que la reflexión primaria, sino a un ángulo ligeramente modificado, θ_H. Esto da lugar a un pico adicional al de la capa y el sustrato llamado pico híbrido. Al igual que la DM normal, la HMD solo se da en determinadas posiciones de φ_0.

Se han encontrado dos familias de picos híbridos en el set de muestras, una con simetría azimutal 6 y otra con simetría 2 y se ha logrado indexar los planos secundarios y cooperativos que los producen, determinando así los valores teóricos para los ángulos θ_H y φ_0. Dichos ángulos calculados se ajustan muy satisfactoriamente a los resultados experimentales.

Una aplicación muy interesante de la HMD es el cálculo de los parámetros de red. En las medidas habituales de los parámetros de

red de estructuras hexagonales, si se desean obtener con alta precisión, es necesario realizar al menos dos mapas del espacio recíproco (RSM). Sin embargo, mediante el uso del fenómeno de la difracción híbrida, midiendo un RSM en el que se vea el pico del sustrato, el de la capa y el híbrido y resolviendo un simple sistema de ecuaciones es posible obtener los parámetros de red de la capa con la misma precisión que con los métodos convencionales, solo que en la mitad de tiempo.

Conclusiones

De acuerdo con el primer objetivo planteado al comienzo de esta tesis consistente en el crecimiento de nanohilos (NHs) ordenados de $Zn_{1-x}Mg_xO$ por el método de vapor-sólido (VS), sobre sustratos policristalinos con patrones en forma de estructuras superficiales autoorganizadas se pueden extraer las siguientes conclusiones:

- Con el fin de encontrar las mejores condiciones para el crecimiento de NHs mediante VS, se realizó un estudio previo sobre el crecimiento de NHs no ordenados de $Zn_{1-x}Mg_xO$, obteniendo que las mejores condiciones para formar las pastillas fuente es utilizar una mezcla de ZnS y 5% en peso de Mg molida durante 5 horas. Fuera de estas condiciones se obtienen muestras con bajas densidades de NHs no homogéneamente distribuidos y algunos segregados de MgO. El análisis de las propiedades luminiscentes de los NHs no ordenados revela un estrechamiento de la banda de emisión cercana al gap y un decrecimiento en la intensidad relativa de la banda de niveles profundos con respecto a la primera.

- Para producir el patrón en los sustratos se han fabricado LIPSS, estructuras superficiales autoorganizadas las cuales son inducidas por la irradiación con un láser de femtosegundo de alta tasa de repetición. Se ha empleado para ello muestras policristalinas basadas en ZnO preparadas en las condiciones previamente determinadas para el proceso de crecimiento. Se ha investigado la capacidad de éstas superficies estructuradas para servir como plantilla en el crecimiento de estructuras ordenadas de baja di-

mensión, mostrando que las mejores regiones para tal efecto son aquellas irradiadas con el régimen de energía más alto.

- En dichas estructuras se obtienen NHs de alta relación de aspecto, ordenados en franjas con un periodo espacial igual al de la línea de irradiación. En cuanto a las propiedades luminiscentes de las nanoestructuras de $Zn_{1-x}Mg_xO$ obtenidas, presentan un aumento de la banda de niveles profundos (DL) respecto de las de ZnO puro. Este es un aspecto de gran importancia para la obtención de dispositivos basados en el ZnO, ya que la sensibilidad de los NHs a los gases está fuertemente relacionada con la intensidad de la banda de defectos.

En relación al segundo objetivo, relacionado con en el crecimiento y caracterización de microcavidades (MCs) de ZnO de alta calidad con orientaciones no polar *m*- y semi polar *r*- usando reflectores de Bragg distriduidos (DBRs) de $Zn_{1-x}Mg_xO$/ZnO, se puede concluir en el caso de las MCs no polares:

- Se han obtenido capas de $Zn_{1-x}Mg_xO$ y MCs completas con superficies e intercaras planas, como demuestran las medidas de microscopía de fuerza atómica y de difracción de rayos X de alta resolución (HRXRD). La rugosidad superficial ha sido estudiada en función del número de capas constituyentes en los DBR y del grosor en el caso de las capas individuales. Se ha visto que la rugosidad de ambas aumenta a medida que crece el grosor total de la muestra, siendo para las MCs a una tasa de crecimiento menor que las capas individuales. El contenido de Mg es homogéneo en toda las heterostructuras. Las capas con grosores mayores de 400 nm y las MCs con más de 20 bicapas presentan fisuras a lo largo de la dirección $< 11.0 >$ aunque dichas fisuras no afectan a las medidas macroscópicas que se han obtenido en esta tesis.

- Medidas de HRXRD muestran que las capas de $Zn_{1-x}Mg_xO$ crecen pseudomórficamente, es decir, completamente estresadas en el plano de crecimiento, exhibiendo parámetros de red próximos a los del sustrato, con un desajuste en compresión de -0.32% a

lo largo de la dirección [11.0] y en tensión de +0.078% a lo largo de la dirección [00.1]. Este hecho, junto a los diferentes coeficientes de expansión térmica entre ambos materiales podrían ser la causa de las fisuras observadas.

- En cuanto a la caracterización óptica, medidas de catodoluminescencia (CL) de las MCs revelan una alta eficiencia de la banda cercana al gap (NBE) y excelentes propiedades ópticas dada la baja intensidad relativa de la banda de defectos. La reflectividad de las MCs es alta dentro de un amplio rango con el modo de la cavidad centrado en $2.94 - 2.96$ eV.

- Finalmente se ha visto que la posibilidad de producir muestras con un alto contenido de bi-capas en los DBR ha permitido alcanzar factores de calidad de entorno a 600 con un desorden fotónico un orden de magnitud más pequeño que el resto de MCs de gap ancho reportadas.

En el caso de las microcavidades orientadas a *r*, solo se ha llevado a cabo el primer paso del estudio equivalente realizado en las MCs *m*-. Así, se han crecido y caracterizado capas epitaxiales individuales de $Zn_{1-x}Mg_xO$ con distintos contenidos de Mg sobre sustratos de ZnO con orientación (01.2). Durante el desarrollo de este estudio, se observaron picos de difracción satélites que nos dieron la oportunidad de estudiar un caso inusual y poco estudiado del fenómeno de la difracción múltiple, llamado difracción múltiple híbrida (HMD) que es consecuencia de la alta calidad cristalina de heteroestructuras. Hasta donde sabemos, la HMD nunca se ha estudiado en sistemas con una simetría tan baja como la de las estructuras. Las principales conclusiones obtenidas en este estudio son:

- Relacionado con la rugosidad, las capas orientadas *r* también muestran superficies planas, independientemente del contenido de Mg en el rango estudiado. Además, las muestras no mostraron fisuras incluso para espesores superiores a 400 nm.

- HRXRD ha demostrado que estas capas también crecen de forma pseudomórfica con respecto al sustrato, independientemente del

contenido de Mg dentro del rango estudiado. Estas mediciones revelaron también que los parámetros de red siguen el comportamiento típico descrito anteriormente del ZnO con contenido de Mg. Sin embargo, también ponen de manifiesto el hecho de que el plano basal tiene una distorsión ortorrómbica, con un ángulo gamma ligeramente superior a 120°, aumentando esta distorsión a medida que crece el contenido de Mg.

- El análisis estructural de capas por HRXRD confirmó la buena calidad de las capas, aunque aparecen unos picos satélite en los barridos $2\theta - \omega$. El valor del ángulo de Bragg al que se observaron estos picos satélite $2\theta_H$ depende del contenido de Mg. Estos picos podrían interpretarse en el marco de la HMD, un tipo especial de difracción múltiple en el que los planos participantes en el fenómeno pertenecen a diferentes materiales, en este caso el sustrato de ZnO y capa de $Zn_{1-x}Mg_xO$.

- Se han encontrado dos conjuntos de reflexiones híbridas, uno exhibiendo $2\theta_H$ más pequeño y con una simetría azimutal de aproximadamente seis y el otro exhibiendo un $2\theta_H$ más grande con una simetría azimutal de aproximadamente dos. Curiosamente, para estas reflexiones híbridas, la diferencia entre la trayectoria del haz hacia adelante y hacia atrás no está girada azimutalmente 180°.

- Se han identificado los planos que contribuyen a la HMD, encontrando cinco conjuntos de planos que explican todos los picos de satélite observados. Este conjunto de planos permite el cálculo de los ángulos teóricos de Bragg $2\theta_H$ y de los ángulos azimutales en los que aparece HMD, obteniendo un acuerdo admirablemente bueno con los valores experimentales.

- El análisis y la precisión angular lograda nos lleva a proponer la HMD para una aplicación tan interesante como la medición precisa de los parámetros de red. Este método proporciona una manera fácil de acortar el tiempo de medición sin sacrificar la precisión.

Desde un punto de vista global, esta tesis ha permitido, no solo los logros anteriormente mencionados, sino también la adquisición de habilidades y amplios conocimientos sobre diferentes técnicas de crecimiento y caracterización.

Bibliography

[1] Ü. Özgür, Y. I. Alivov, C. Liu, A. Teke, M. A. Reshchikov, S. Doğan, V. Avrutin, S. J. Cho, and H. Morkoç, "A comprehensive review of ZnO materials and devices," *J. Appl. Phys.*, vol. 98, no. 4, p. 041301, 2005. (Cited on page 3, 12, 36, 109 and 113.)

[2] A. Osinsky and S. Karpov, "ZnO-Based Light Emitters," in *Zinc Oxide Bulk, Thin Film. Nanostructures*, ch. 15, 2006. (Cited on page 3 and 109.)

[3] S. Kalusniak, S. Sadofev, S. Halm, and F. Henneberger, "Vertical cavity surface emitting laser action of an all monolithic ZnO-based microcavity," *Appl. Phys. Lett.*, vol. 98, no. 1, pp. 98–101, 2011. (Cited on page 3 and 109.)

[4] Y.-J. Lu, H.-F. Li, C.-X. Shan, B.-H. Li, D.-Z. Shen, L.-G. Zhang, and S.-F. Yu, "Improved performance of ZnO light-emitting devices by introducing a hole-injection layer," *Opt. Express*, vol. 22, no. 14, pp. 17524–17531, 2014. (Cited on page 3 and 109.)

[5] Q. Wan, C. L. Lin, X. B. Yu, and T. H. Wang, "Room-temperature hydrogen storage characteristics of ZnO nanowires," *Appl. Phys. Lett.*, vol. 84, no. 1, pp. 124–126, 2004. (Cited on page 4 and 110.)

[6] R. Könenkamp, R. C. Word, C. Schlegel, R. Könenkamp, R. C. Word, and C. Schlegel, "Vertical nanowire light-emitting diode,"

Appl. Phys. Lett., vol. 24, pp. 6004–6006, 2004. (Cited on page 4 and 110.)

[7] J. B. Baxter and E. S. Aydil, "Nanowire-based dye-sensitized solar cells," *Appl. Phys. Lett.*, vol. 86, no. 5, pp. 1–3, 2005. (Cited on page 4 and 110.)

[8] X. Wang, J. Zhou, J. Song, J. Liu, N. Xu, and Z. L. Wang, "Piezoelectric field effect transistor and nanoforce sensor based on a single ZnO nanowire," *Nano Lett.*, vol. 6, no. 12, pp. 2768–2772, 2006. (Cited on page 4 and 110.)

[9] S. M. Al-Hilli, M. Willander, A. Öst, and P. Strålfors, "ZnO nanorods as an intracellular sensor for pH measurements," *J. Appl. Phys.*, vol. 102, p. 084304, 2007. (Cited on page 4 and 110.)

[10] R. Könenkamp, A. Nadarajah, R. C. Word, J. Meiss, and R. Engelhardt, "ZnO nanowires for LED and field-emission displays," *J. Soc. Inf. Disp.*, vol. 16, no. 5, pp. 609–613, 2008. (Cited on page 4 and 110.)

[11] R. D. Shannon, "Revised effective ionic radii and systematic studies of interatomic distances in halides and chalcogenides," *Acta Crystallogr. Sect. A*, vol. 32, no. 5, pp. 751–767, 1976. (Cited on page 4 and 110.)

[12] S. Choopun, R. D. Vispute, W. Yang, R. P. Sharma, T. Venkatesan, and H. Shen, "Realization of band gap above 5.0 eV in metastable cubic-phase MgxZn1-xO alloy films," *Appl. Phys. Lett.*, vol. 80, no. 9, pp. 1529–1531, 2002. (Cited on page 4 and 110.)

[13] Y. Heo, M. Kaufman, K. Pruessner, D. Norton, F. Ren, M. Chisholm, and P. Fleming, "Optical properties of Zn1-xMgxO nanorods using catalysis-driven molecular beam epitaxy," *Solid. State. Electron.*, vol. 47, no. 12, pp. 2269–2273, 2003. (Cited on page 4 and 110.)

[14] R. Kling, C. Kirchner, T. Gruber, F. Reuss, and A. Waag, "Analysis of ZnO and ZnMgO nanopillars grown by self-organization," *Nanotechnology*, vol. 15, no. 8, pp. 1043–1046, 2004. (Cited on page 4 and 110.)

[15] M. Zhi, L. Zhu, Z. Ye, F. Wang, and B. Zhao, "Preparation and Properties of Ternary ZnMgO Nanowires," *Phys. Chem. B*, vol. 109, no. 100, pp. 23930–23934, 2005. (Cited on page 4 and 110.)

[16] C. Y. Lee, T. Y. Tseng, S. Y. Li, and P. Lin, "Single-crystalline MgxZn1-x O (0 ≤x≤ 0.25) nanowires on glass substrates obtained by a hydrothermal method: growth, structure and electrical characteristics," *Nanotechnology*, vol. 16, no. 8, pp. 1105–1111, 2005. (Cited on page 4 and 110.)

[17] H. Pan, J. Luo, H. Sun, Y. Feng, C. Poh, and J. Lin, "Hydrogen storage of ZnO and Mg doped ZnO nanowires," *Nanotechnology*, vol. 17, pp. 2963–2967, jun 2006. (Cited on page 4 and 110.)

[18] H.-C. Hsu, C.-Y. Wu, H.-M. Cheng, and W.-F. Hsieh, "Band gap engineering and stimulated emission of ZnMgO nanowires," *Appl. Phys. Lett.*, vol. 89, no. 1, p. 013101, 2006. (Cited on page 4 and 110.)

[19] C. J. Pan, H. C. Hsu, H. M. Cheng, C. Y. Wu, and W. F. Hsieh, "Structural and optical properties of ZnMgO nanostructures formed by Mg in-diffused ZnO nanowires," *J. Solid State Chem.*, vol. 180, no. 4, pp. 1188–1192, 2007. (Cited on page 4 and 110.)

[20] H. Tang, B. J. Kwon, and J.-Y. Park, "Characterizations of individual ZnMgO nanowires synthesized by a vapor-transport method," *Phys. Status Solidi*, vol. 207, pp. 2478–2482, nov 2010. (Cited on page 4 and 110.)

[21] H. Y. Yang, S. F. Yu, G. P. Li, and T. Wu, "Random lasing action of randomly assembled ZnO Nanowires with MgO coating," *Opt.*

Expree, vol. 18, no. 13, pp. 13647–13654, 2010. (Cited on page 4 and 110.)

[22] H. He, Q. Yang, C. Liu, L. Sun, and Z. Ye, "Size-dependent surface effects on the photoluminescence in ZnO nanorods," *J. Phys. Chem. C*, vol. 115, no. 1, pp. 58–64, 2011. (Cited on page 4 and 110.)

[23] J. Singh, P. Kumar, K. S. Hui, K. N. Hui, K. Ramam, R. S. Tiwari, and O. N. Srivastava, "Synthesis, band-gap tuning, structural and optical investigations of Mg doped ZnO nanowires," *CrystEngComm*, vol. 14, no. 18, p. 5898, 2012. (Cited on page 4 and 110.)

[24] I. Isakov, M. Panfilova, M. J. L. Sourribes, and P. A. Warburton, "Growth of ZnO and ZnMgO nanowires by Au-catalysed molecular-beam epitaxy," *Phys. Status Solidi C*, vol. 10, pp. 1308–1313, 2013. (Cited on page 4 and 110.)

[25] G. Grinblat, L. J. Borrero-González, L. a. O. Nunes, M. Tirado, and D. Comedi, "Enhanced optical properties and (Zn, Mg) interdiffusion in vapour transport grown ZnO/MgO core/shell nanowires.," *Nanotechnology*, vol. 25, no. 3, p. 035705, 2014. (Cited on page 4 and 110.)

[26] S. T. Picraux, J. Yoo, I. H. Campbell, S. A. Dayeh, and D. E. Perea, "Semiconductor Nanowires for Solar Cells," in *Semicond. Nanostructures Optoelectron. Devices*, ch. 11, Heidelberg, Berlin: Springer, 2012. (Cited on page 4 and 110.)

[27] M. Birnbaum, "Semiconductor Surface Damage Produced by Ruby Lasers," *J. Appl. Phys.*, vol. 3688, pp. 1–3, 1965. (Cited on page 5 and 111.)

[28] J. E. Sipe, J. F. Young, J. S. Preston, and H. M. Van Driel, "Laser-induced periodic surface structure. I. Theory," *Phys. Rev. B*, vol. 27, no. 2, pp. 1141–1154, 1983. (Cited on page 5 and 111.)

[29] J. F. Young, J. S. Preston, H. M. Van Driel, and J. E. Sipe, "Laser-induced periodic surface structure. II. Experiments on Ge, Si, Al, and brass," *Phys. Rev. B*, vol. 27, no. 2, pp. 1155–1172, 1983. (Cited on page 5 and 111.)

[30] D. Dufft, A. Rosenfeld, S. K. Das, R. Grunwald, and J. Bonse, "Femtosecond laser-induced periodic surface structures revisited : A comparative study on ZnO," *J. Appl. Phys.*, vol. 105, no. 2009, p. 034908, 2009. (Cited on page 5, 41 and 111.)

[31] J. Z. P. Skolski and J. V. Obona, "Modeling laser-induced periodic surface structures : Finite-difference time-domain feedback simulations," *J. Appl. Phys.*, vol. 115, p. 103102, 2014. (Cited on page 5 and 111.)

[32] G. Escalante, Y. Ryu, A. Ruiíz de la Cruz, D. Puerto, J. Solís, and P. Fernández, "Growth of ZnO nanostructures by femtosecond laser irradiation of polycrystalline targets," *Appl. Phys. A*, 2015. (Cited on page 5 and 111.)

[33] X. D. Guo, R. X. Li, Y. Hang, Z. Z. Xu, B. K. Yu, H. L. Ma, B. Lu, and X. W. Sun, "Femtosecond laser-induced periodic surface structure on ZnO," *Mater. Lett.*, vol. 62, no. 12-13, pp. 1769–1771, 2008. (Cited on page 5 and 111.)

[34] W. Liang, F. Chen, H. Bian, Q. Yang, H. Liu, X. Wang, J. Si, and X. Hou, "Periodic surface nanostructures on polycrystalline ZnO induced by femtosecond laser pulses," *Opt. Commun.*, vol. 283, no. 11, pp. 2385–2389, 2010. (Cited on page 5 and 111.)

[35] A. K. Sharma, J. Narayan, J. F. Muth, C. W. Teng, C. Jin, A. Kvit, R. M. Kolbas, and O. W. Holland, "Optical and structural properties of epitaxial MgxZn1-xO alloys," *Appl. Phys. Lett.*, vol. 75, no. 21, pp. 3327–3329, 1999. (Cited on page 6 and 111.)

[36] C. W. Teng, J. F. Muth, Ü. Özgür, M. J. Bergmann, H. O. Everitt, A. K. Sharma, C. Jin, and J. Narayan, "Refractive indices and absorption coefficients of MgxZn1-xO alloys," *Appl.*

Phys. Lett., vol. 76, no. 8, pp. 979–981, 2000. (Cited on page 6, 18, 19, 65, 99, 111 and 114.)

[37] C. Bundesmann, M. Schubert, D. Spemann, T. Butz, M. Lorenz, E. M. Kaidashev, M. Grundmann, N. Ashkenov, H. Neumann, and G. Wagner, "Infrared dielectric functions and phonon modes of wurtzite MgxZn1-xO(x≤ 0.2)," *Appl. Phys. Lett.*, vol. 81, no. 13, pp. 2376–2378, 2002. (Cited on page 6 and 111.)

[38] R. Schmidt, B. Rheinländer, M. Schubert, D. Spemann, T. Butz, J. Lenzner, E. M. Kaidashev, M. Lorenz, A. Rahm, H. C. Semmelhack, and M. Grundmann, "Dielectric functions (1 to 5 eV) of wurtzite MgxZn1-xO(x≤ 0.29) thin films," *Appl. Phys. Lett.*, vol. 82, no. 14, pp. 2260–2262, 2003. (Cited on page 6 and 111.)

[39] A. Almamun Ashrafi and Y. Segawa, "Determination of Mg composition in MgxZn1-xO alloy: Validity of Vegard's law," *J. Vac. Sci. Technol. B Microelectron. Nanom. Struct.*, vol. 23, no. 5, p. 2030, 2005. (Cited on page 6 and 111.)

[40] Z. Vashaei, T. Minegishi, H. Suzuki, T. Hanada, M. W. Cho, T. Yao, and A. Setiawan, "Structural variation of cubic and hexagonal MgxZn1-xO layers grown on MgO(111) c-sapphire," *J. Appl. Phys.*, vol. 98, no. 5, p. 054911, 2005. (Cited on page 6 and 111.)

[41] S. Heitsch, G. Zimmermann, D. Fritsch, C. Sturm, R. Schmidt-Grund, C. Schulz, H. Hochmuth, D. Spemann, G. Benndorf, B. Rheinlander, T. Nobis, M. Lorenz, and M. Grundmann, "Luminescence and surface properties of MgxZn1-xO thin films grown by pulsed laser deposition," *J. Appl. Phys.*, vol. 101, no. 8, p. 083521, 2007. (Cited on page 6 and 111.)

[42] T. A. Wassner, B. Laumer, S. Maier, A. Laufer, B. K. Meyer, M. Stutzmann, and M. Eickhoff, "Optical properties and structural characteristics of ZnMgO grown by plasma assisted molecular beam epitaxy," *J. Appl. Phys.*, vol. 105, no. 2, 2009. (Cited on page 6 and 111.)

[43] B. Laumer, F. Schuster, M. Stutzmann, A. Bergmaier, G. Dollinger, and M. Eickhoff, "Accurate determination of optical bandgap and lattice parameters of Zn1-xMgxO epitaxial films (0 ≤x≤ 0.3) grown by plasma-assisted molecular beam epitaxy on a -plane sapphire," *J. Appl. Phys.*, vol. 113, no. 23, p. 233512, 2013. (Cited on page 6, 16, 17, 61, 99, 111 and 114.)

[44] J. Perkins, G. M. Foster, M. Myer, S. Mehra, J. M. Chauveau, A. Hierro, A. Redondo-Cubero, W. Windl, and L. J. Brillson, "Impact of Mg content on the structural and optical properties of MgxZn1-x O alloys," *APL Mater.*, vol. 3, no. 1, p. 062801, 2015. (Cited on page 6 and 111.)

[45] A. V. Kavokin, J. Baumberg, G. Malpuech, and F. Laussy, *Microcavities*. New York, USA: Oxford University Pres, 2007. (Cited on page 6, 7 and 111.)

[46] A. Imamoglu, R. J. Ram, S. Pau, and Y. Yamamoto, "Nonequilibrium condensates and lasers without inversion: Exciton-polariton lasers," *Phys. Rev. A*, vol. 53, no. 6, pp. 4250–4253, 1996. (Cited on page 6 and 112.)

[47] L. S. Dang, D. Heger, R. André, F. Bœuf, and R. Romestain, "Stimulation of polariton photoluminescence in semiconductor microcavity," *Phys. Rev. Lett.*, vol. 81, no. 18, pp. 3920–3923, 1998. (Cited on page 6 and 112.)

[48] G. Malpuech, A. Di Carlo, A. Kavokin, J. J. Baumberg, M. Zamfirescu, and P. Lugli, "Room-temperature polariton lasers based on GaN microcavities," *Appl. Phys. Lett.*, vol. 81, no. 3, pp. 412–414, 2002. (Cited on page 6 and 112.)

[49] M. Zamfirescu, A. Kavokin, B. Gil, G. Malpuech, and M. Kaliteevski, "ZnO as a material mostly adapted for realization of room-temperature polariton lasers," *Phys. Rev. B*, vol. 65, 2002. (Cited on page 6 and 112.)

[50] T. Guillet, M. Mexis, J. Levrat, G. Rossbach, C. Brimont, T. Bretagnon, B. Gil, R. Butté, N. Grandjean, L. Orosz,

F. Réveret, J. Leymarie, J. Zúñiga-Pérez, M. Leroux, F. Semond, and S. Bouchoule, "Polariton lasing in a hybrid bulk ZnO microcavity," *Appl. Phys. Lett.*, vol. 99, no. 16, pp. 10–13, 2011. (Cited on page 6 and 112.)

[51] T. Guillet, C. Brimont, P. Valvin, B. Gil, T. Bretagnon, F. Médard, M. Mihailovic, J. Zúñiga-Pérez, M. Leroux, F. Semond, and S. Bouchoule, "Laser emission with excitonic gain in a ZnO planar microcavity," *Appl. Phys. Lett.*, vol. 98, no. 21, 2011. (Cited on page 6 and 112.)

[52] L. Orosz, F. Réveret, F. Médard, P. Disseix, J. Leymarie, M. Mihailovic, D. Solnyshkov, G. Malpuech, J. Zúñiga-Pérez, F. Semond, M. Leroux, S. Bouchoule, X. Lafosse, M. Mexis, C. Brimont, and T. Guillet, "LO-phonon-assisted polariton lasing in a ZnO-based microcavity," *Phys. Rev. B - Condens. Matter Mater. Phys.*, vol. 85, no. 12, pp. 1–5, 2012. (Cited on page 6 and 112.)

[53] F. Li, L. Orosz, O. Kamoun, S. Bouchoule, C. Brimont, P. Disseix, T. Guillet, X. Lafosse, M. Leroux, J. Leymarie, G. Malpuech, M. Mexis, M. Mihailovic, G. Patriarche, F. Réveret, D. Solnyshkov, and J. Zúñiga-Pérez, "Fabrication and characterization of a room-temperature ZnO polariton laser," *Appl. Phys. Lett.*, vol. 102, no. 19, pp. 2011–2015, 2013. (Cited on page 6 and 112.)

[54] F. Li, L. Orosz, O. Kamoun, S. Bouchoule, C. Brimont, P. Disseix, T. Guillet, X. Lafosse, M. Leroux, J. Leymarie, M. Mexis, M. Mihailovic, G. Patriarche, F. Réveret, D. Solnyshkov, J. Zúñiga-Perez, and G. Malpuech, "From excitonic to photonic polariton condensate in a ZnO-based microcavity," *Phys. Rev. Lett.*, vol. 110, no. 19, pp. 1–5, 2013. (Cited on page 6 and 112.)

[55] F. Li, *Fabrication and Characterization of ZnO-based Microcavities Working in the Strong Coupling Regime : Polariton Laser Jury :.* PhD thesis, Université de Nice-Sophia Antipolis, 2013. (Cited on page 6 and 112.)

[56] Y. Y. Lai, Y. P. Lan, and T. C. Lu, "Strong light-matter interaction in ZnO microcavities," *Light Sci. Appl.*, vol. 2, no. JUNE, 2013. (Cited on page 6 and 112.)

[57] J. Zúñiga-Pérez, E. Mallet, R. Hahe, M. J. Rashid, S. Bouchoule, C. Brimont, P. Disseix, J. Y. Duboz, G. Gommé, T. Guillet, O. Jamadi, X. Lafosse, M. Leroux, J. Leymarie, F. Li, F. Réveret, and F. Semond, "Patterned silicon substrates: A common platform for room temperature GaN and ZnO polariton lasers," *Appl. Phys. Lett.*, vol. 104, no. 24, 2014. (Cited on page 6 and 112.)

[58] J. Zúñiga-Pérez, V. Consonni, L. Lymperakis, X. Kong, A. Trampert, S. Fernández, O. Brandt, H. Renevier, S. Keller, K. Hestroffer, M. R. Wagner, J. Sebastián, F. Akyol, S. Rajan, S. Rennesson, T. Palacios, G. Feuillet, O. Brandt, H. Renevier, A. Trampert, S. Fern, S. Keller, K. Hestroffer, M. R. Wagner, and J. Sebasti, "Polarity in GaN and ZnO : Theory, measurement, growth, and devices," *Appl. Phys. Rev.*, vol. 3, no. 25, p. 41303, 2016. (Cited on page 7.)

[59] P. Venéguès, J. M. Chauveau, M. Korytov, C. Deparis, J. Zúñiga-Pérez, and C. Morhain, "Interfacial structure and defect analysis of nonpolar ZnO films grown on R -plane sapphire by molecular beam epitaxy," *J. Appl. Phys.*, vol. 103, no. 8, pp. 1–8, 2008. (Cited on page 7 and 112.)

[60] J. W. Lee, J. H. Kim, S. K. Han, S. K. Hong, J. Y. Lee, S. I. Hong, and T. Yao, "Interface and defect structures in ZnO films on m-plane sapphire substrates," *J. Cryst. Growth*, vol. 312, no. 2, pp. 238–244, 2010. (Cited on page 7 and 112.)

[61] J. M. Chauveau, M. Teisseire, H. Kim-Chauveau, C. Deparis, C. Morhain, and B. Vinter, "Benefits of homoepitaxy on the properties of nonpolar (Zn,Mg)O/ZnO quantum wells on a -plane ZnO substrates," *Appl. Phys. Lett.*, vol. 97, no. 8, pp. 1–4, 2010. (Cited on page 7 and 112.)

[62] C. Feng, *Handbook of Zinc Oxide and Related Materials. Volume one*. Boca Raton, USA: CRC Press, 2013. (Cited on page 11.)

[63] S. C. Abrahams and J. L. Bernstein, "Remeasurement of the structure of hexagonal ZnO," *Acta Crystallogr. Sect. B Struct. Crystallogr. Cryst. Chem.*, vol. 25, no. 7, pp. 1233–1236, 1969. (Cited on page 12.)

[64] A. Jackson, *Handbook of Crystallography*. springer ed., 1991. (Cited on page 12.)

[65] B. K. Meyer, H. Alves, D. M. Hofmann, W. Kriegseis, D. Forster, F. Bertram, J. Christen, a. Hoffmann, M. Straßburg, M. Dworzak, U. Haboeck, and a. V. Rodina, "Bound exciton and donor-acceptor pair recombinations in ZnO," *Phys. Status Solidi*, vol. 241, no. 2, pp. 231–260, 2004. (Cited on page 13, 14, 15, 75 and 99.)

[66] D. Thomas, "The exciton spectrum of zinc oxide," *J. Phys. Chem. Solids*, vol. 15, no. 1-2, pp. 86–96, 1960. (Cited on page 14.)

[67] D. Reynolds, D. Look, B. Jogai, G. Cantwell, and W. C. Harsch, "Valence-band ordering in ZnO," *Phys. Rev. B - Condens. Matter Mater. Phys.*, vol. 60, no. 4, pp. 2340–2344, 1999. (Cited on page 14.)

[68] M. Willander, O. Nur, J. R. Sadaf, M. I. Qadir, S. Zaman, A. Zainelabdin, N. Bano, and I. Hussain, "Luminescence from zinc oxide nanostructures and polymers and their hybrid devices," *Materials (Basel).*, vol. 3, no. 4, pp. 2643–2667, 2010. (Cited on page 15 and 36.)

[69] E. N. Epie and W. K. Chu, "Applied Surface Science Ionoluminescence study of Zn- and O- implanted ZnO crystals : An additional perspective," *Appl. Surf. Sci.*, vol. 371, pp. 28–34, 2016. (Cited on page 16, 41 and 99.)

[70] S. Canney, V. Sashin, M. Ford, and A. Kheifets, "Electronic band structure of magnesium and magnesium oxide: experiment and theory," *J. Phys. Condens. Matter*, vol. 7507, no. 4, 1999. (Cited on page 15, 16 and 114.)

[71] N. Wang, Y. Cai, and R. Q. Zhang, "Growth of nanowires," *Mater. Sci. Eng.*, vol. 60, pp. 1–51, 2008. (Cited on page 18.)

[72] Z. L. Wang, "Zinc oxide nanostructures: growth, properties and applications," *J. Phys. Condens. Matter*, vol. 16, no. 25, p. R829, 2004. (Cited on page 19 and 33.)

[73] D. Puerto, J. Siegel, W. Gawelda, M. Galvan-Sosa, L. Ehrentraut, J. Bonse, and J. Solis, "Dynamics of plasma formation, relaxation, and topography modification induced by femtosecond laser pulses in crystalline and amorphous dielectrics," *J. Opt. Soc. Am. B*, vol. 27, no. 5, p. 1065, 2010. (Cited on page 21.)

[74] D. Puerto, M. Garcia-Lechuga, J. Hernandez-Rueda, A. Garcia-Leis, S. Sanchez-Cortes, J. Solis, and J. Siegel, "Femtosecond laser-controlled self-assembly of amorphous-crystalline nanogratings in silicon," *Nanotechnology*, vol. 27, no. 26, p. 265602, 2016. (Cited on page 21.)

[75] P. Eaton, Peter; West, *Atomic Force Microscopy*. New York, USA: OUP, 2010. (Cited on page 25.)

[76] H. J. Yuan, S. S. Xie, D. F. Liu, X. Q. Yan, Z. P. Zhou, L. J. Ci, J. X. Wang, Y. Gao, L. Song, L. F. Liu, W. Y. Zhou, and G. Wang, "Characterization of zinc oxide crystal nanowires grown by thermal evaporation of ZnS powders," *Chem. Phys. Lett.*, vol. 371, no. 3-4, pp. 337–341, 2003. (Cited on page 33 and 117.)

[77] L. Khomenkova, P. Fernández, and J. Piqueras, "ZnO nanostructured microspheres and elongated structures grown by thermal treatment of ZnS powder," *Cryst. Growth Des.*, vol. 7, no. 4, pp. 836–839, 2007. (Cited on page 33 and 117.)

[78] S. Señorís, B. Sotillo, A. Urbieta, and P. Fernández *J. Alloys Compd.*, vol. 687, pp. 161–167, 2016. (Cited on page 33 and 117.)

[79] A. Urbieta, P. Fernández, and J. Piqueras, "Growth and Luminescence of Nanowires and Oriented Nanoplate Arrays of Mg Doped ZnO," *J. nano Res.*, vol. 4, no. 2008, pp. 27–32, 2009. (Cited on page 33, 50 and 117.)

[80] A. F. Kohan, G. Ceder, D. Morgan, and C. G. V. D. Walle, "First-principles study of native point defects in ZnO," *Phys. Rev. B*, vol. 61, no. 22, pp. 19–27, 2000. (Cited on page 36.)

[81] M. Zamfirescu, A. Dinescu, M. Danila, G. Socol, and C. Radu, "The role of the substrate material type in formation of laser induced periodical surface structures on ZnO thin films," *Appl. Surf. Sci.*, vol. 258, no. 23, pp. 9385–9388, 2012. (Cited on page 38.)

[82] R. Wagner, J. Gottmann, A. Horn, and E. W. Kreutz, "Subwavelength ripple formation induced by tightly focused femtosecond laser radiation," *Appl. Surf. Sci.*, vol. 252, no. 24, pp. 8576–8579, 2006. (Cited on page 39.)

[83] L. Ran and S. Qu, "Structure formation on the surface of alloys irradiated by femtosecond laser pulses," *Appl. Surf. Sci.*, vol. 256, no. 8, pp. 2315–2318, 2010. (Cited on page 39.)

[84] M. R. Querry, "Optical constants, Report No. AD-A158-623," tech. rep., University of Missouri, Kansas city, Missouri 64110, 1985. (Cited on page 41.)

[85] Y. Ortega, P. Fernández, and J. Piqueras, "Al doped ZnO nanoplate arrays and microbox structures grown by thermal deposition," *Journal of Applied Physics*, vol. 105, p. 054315, 2009. (Cited on page 52.)

[86] L. Liao, H. B. Lu, J. C. Li, C. Liu, and D. J. Fu, "The sensitivity of gas sensor based on single ZnO nanowire modulated by helium

ion radiation," *Appl. Phys. Lett.*, vol. 91, no. May 2013, pp. 14–17, 2007. (Cited on page 54.)

[87] O. Lupan, V. V. Ursaki, G. Chai, L. Chow, G. A. Emelchenko, and I. M. Tiginyanu, "Selective hydrogen gas nanosensor using individual ZnO nanowire with fast response at room temperature," *Sensors Actuators B: Chemical*, vol. 144, pp. 56–66, 2010. (Cited on page 54.)

[88] J. Zúñiga-Pérez, L. Kappei, C. Deparis, F. Reveret, M. Grundmann, E. L. de Prado, O. Jamadi, J. Leymarie, S. Chenot, and M. Leroux, "Homoepitaxial $(10-10)$ m-plane ZnO/ZnMgO monolithic microcavities: towards reduced photonic disorder," *Appl. Phys. Lett.*, vol. 108, pp. 39–44, 2016. (Cited on page 59, 65, 66, 101 and 102.)

[89] K. Okamoto, T. Tanaka, M. Kubota, and H. Ohta, "Pure blue laser diodes based on nonpolar m-plane gallium nitride with InGaN waveguiding layers," *Japanese J. Appl. Physics, Part 2 Lett.*, vol. 46, no. 33-35, pp. 8–11, 2007. (Cited on page 60.)

[90] E. C. Young, A. E. Romanov, C. S. Gallinat, A. Hirai, G. E. Beltz, and J. S. Speck, "Anisotropy of tensile stresses and cracking in nonbasal plane AlxGa1-xN/GaN heterostructures," *Appl. Phys. Lett.*, vol. 96, no. 4, pp. 11–14, 2010. (Cited on page 60.)

[91] Y. V. Kaneti, Z. Zhang, J. Yue, Q. M. D. Zakaria, C. Chen, X. Jiang, and A. Yu, "Crystal plane-dependent gas-sensing properties of zinc oxide nanostructures: experimental and theoretical studies," *Phys. Chem. Chem. Phys.*, vol. 16, no. 23, pp. 11471–11480, 2014. (Cited on page 62 and 102.)

[92] D. M. Schaadt, O. Brandt, S. Ghosh, T. Flissikowski, U. Jahn, and H. T. Grahn, "Polarization-dependent beam switch based on an M-plane GaN/AlN distributed Bragg reflector," *Appl. Phys. Lett.*, vol. 90, no. 23, pp. 1–4, 2007. (Cited on page 64.)

[93] T. Zhu, A. Dussaigne, G. Christmann, C. Pinquier, E. Feltin, D. Martin, R. Butté, and N. Grandjean, "Nonpolar GaN-based

microcavity using AlNGaN distributed Bragg reflector," *Appl. Phys. Lett.*, vol. 92, no. 6, pp. 1–4, 2008. (Cited on page 64.)

[94] G. Rossbach, J. Levrat, A. Dussaigne, G. Cosendey, M. Glauser, M. Cobet, R. Butté, N. Grandjean, H. Teisseyre, M. Bockowski, I. Grzegory, and T. Suski, "Tailoring the light-matter coupling in anisotropic microcavities: Redistribution of oscillator strength in strained m-plane GaN/AlGaN quantum wells," *Phys. Rev. B - Condens. Matter Mater. Phys.*, vol. 84, no. 11, pp. 1–8, 2011. (Cited on page 64.)

[95] J. Levrat, G. Rossbach, A. Dussaigne, G. Cosendey, M. Glauser, M. Cobet, R. Butté, N. Grandjean, H. Teisseyre, M. Boćkowski, I. Grzegory, and T. Suski, "Nonlinear emission properties of an optically anisotropic GaN-based microcavity," *Phys. Rev. B - Condens. Matter Mater. Phys.*, vol. 86, no. 16, 2012. (Cited on page 64.)

[96] J. M. Chauveau, Y. Xia, I. Ben Taazaet-Belgacem, M. Teisseire, B. Roland, M. Nemoz, J. Brault, B. Damilano, M. Leroux, and B. Vinter, "Built-in electric field in ZnO based semipolar quantum wells grown on $(10-12)$ ZnO substrates," *Appl. Phys. Lett.*, vol. 103, no. 26, pp. 0–5, 2013. (Cited on page 72 and 103.)

[97] T. Hanada, "Basic Properties of ZnO, GaN, and Related Materials," in *Oxide Nitride Semicond.*, ch. 1, pp. 1–19, Heidelberg, Berlin: Springer, 12 ed., 2009. (Cited on page 73.)

[98] B. D. Cullity, *Elements of diffraction*. United States of America: Addison-Wesley, 1978. (Cited on page 73 and 88.)

[99] M. R. Laskar, T. Ganguli, A. A. Rahman, A. Mukherjee, N. Hatui, M. Gokhale, and A. Bhattacharya, "Distorted wurtzite unit cells : Determination of lattice parameters of nonpolar -plane AlGaN and estimation of solid phase Al content," *J. Appl. Phys.*, vol. 109, p. 013107, 2011. (Cited on page 73.)

[100] M. Renninger, ""Detour-excitation" a hitherto unobserved interaction effect in space-lattice interference," *Zeitschrift für Phys.*, vol. 106, no. November, pp. 141–76, 1937. (Cited on page 77.)

[101] M. Renninger, "Beitrag zur Kenntnis der röntgenographischen Unterschiede zwischen den beiden Diamant-Typen," *Acta Crystallogr.*, vol. 8, no. 10, pp. 606–610, 1955. (Cited on page 77.)

[102] H. Cole, F. H. Chambers, and H. M. Dunn, "Simultaneous diffraction. Indexing unweganregung peaks in simple cases," *Acta Crystallogr.*, vol. 15, no. 2, pp. 138–144, 1962. (Cited on page 77.)

[103] B. Post, "Accurate Lattice Constants from Multiple Diffraction Measurements .I. Geometry, Techiniques and Systematic errors," *J. Appl. Cryst*, vol. 8, pp. 452–456, 1975. (Cited on page 77.)

[104] T. Hom, W. Kiszenik, and B. Post, "Accurate lattice constants from multiple reflection measurements. II. Lattice constants of germanium silicon, and diamond," *J. Appl. Crystallogr.*, vol. 8, no. 4, pp. 457–458, 1975. (Cited on page 77.)

[105] J. Biäsing and A. Krost, "X-ray multiple diffraction (Umweganregung) in wurtzite-type GaN and ZnO epitaxial layers," *Phys. Status Solidi Appl. Res.*, vol. 201, no. 4, pp. 17–20, 2004. (Cited on page 77 and 82.)

[106] M. C. Martínez-Tomás, D. N. Montenegro, V. Sallet, and V. Muñoz-Sanjosé, "High resolution x-ray diffraction methodology for the structural analysis of one-dimensional nanostructures," *J. Appl. Phys.*, vol. 112, no. 1, p. 014305, 2012. (Cited on page 77.)

[107] M. C. Martínez-Tomás, D. N. Montenegro, S. Agouram, V. Sallet, and V. Muñoz-Sanjosé, "Assessment of the out-plane and in-plane ordering of high quality ZnO nanorods by X-ray multiple diffraction," *Thin Solid Films*, vol. 541, pp. 107–112, 2013. (Cited on page 77 and 84.)

[108] M. Grundmann, M. Scheibe, M. Lorenz, J. Bläsing, and A. Krost, "X-ray multiple diffraction of ZnO substrates and heteroepitaxial thin films," *Phys. Status Solidi Basic Res.*, vol. 251, no. 4, pp. 850–863, 2014. (Cited on page 77, 82 and 84.)

[109] S.-L. Chang, "A multibeam x-ray topographic method for a double-crystal arrangement," *J. Appl. Phys.*, vol. 53, no. 4, p. 2988, 1982. (Cited on page 77.)

[110] S. L. Morelhão and L. P. Cardoso, "X-ray Multiple Diffraction Phenomenon in the Evaluation of Semiconductor Crystalline Perfection," *J. Appl. Crystallogr.*, vol. 29, no. 4, pp. 446–456, 1996. (Cited on page 77 and 98.)

[111] Y. Chuan-zheng, H. a. O. Jian-min, and P. E. I. Guang-wen, "Brief Introduction of X-Ray Multiple Diffraction," *Rigaku J.*, vol. 17, no. 1, pp. 46–57, 2000. (Cited on page 78.)

[112] E. De Prado, M. C. Martínez-Tomás, C. Deparis, V. Muñoz-Sanjosé, and J. Zuñiga-Pérez, "Hybrid multiple diffraction in semipolar wurtzite materials: (0112)-oriented ZnMgO/ZnO heterostructures as an illustration," *J. Appl. Crystallogr.*, vol. 50, pp. 1165–1173, 2017. (Cited on page 78 and 103.)

[113] B. J. Isherwood, B. R. Brown, and M. A. G. Halliwell, "X-ray multiple diffraction as a tool for studying heteroepitaxial layers. I," *J. Cryst. Growth*, vol. 54, no. 3, pp. 449–460, 1981. (Cited on page 79.)

[114] S. L. Morelhão and L. P. Cardoso, "Simulation of hybrid reflections in X-ray multiple diffraction experiments," *J. Cryst. Growth*, vol. 110, no. 3, pp. 543–552, 1991. (Cited on page 79.)

[115] S. L. Morelhão, L. P. Cardoso, J. M. Sasaki, and M. M. G. De Carvalho, "Hybrid multiple diffraction in Renninger scan for heteroepitaxial layers," *J. Appl. Phys.*, vol. 70, no. 5, pp. 2589–2593, 1991. (Cited on page 79.)

[116] S. L. Morelhão and L. P. Cardoso, "Structural properties of heteroepitaxial systems using hybrid multiple diffraction in Renninger scans," *J. Appl. Phys.*, vol. 73, no. 9, pp. 4218–4226, 1993. (Cited on page 79.)

[117] S. L. Morelhão, A. A. Quivy, and J. Härtwig, "Hybrid and effective satellites for studying superlattices," *Microelectronics J.*, vol. 34, no. 5-8, pp. 695–699, 2003. (Cited on page 79 and 98.)

[118] S. L. Morelhão and J. Z. Domagala, "Hybrid reciprocal space for X-ray diffraction in epitaxic layers," *J. Appl. Crystallogr.*, vol. 40, no. 3, pp. 546–551, 2007. (Cited on page 79 and 98.)

[119] J. Z. Domagała, S. L. Morelhão, M. Sarzyński, M. Maździarz, P. Dłużewski, and M. Leszczyński, "Hybrid reciprocal lattice: application to layer stress appointment in GaAlN/GaN(0001) systems with patterned substrates," *J. Appl. Crystallogr.*, vol. 49, no. June, pp. 798–805, 2016. (Cited on page 79 and 81.)

[120] M. C. Martínez-Tomás, V. Hortelano, J. Jiménez, B. Wang, and V. Muñoz-Sanjosé, "High resolution X-ray diffraction, X-ray multiple diffraction and cathodoluminescence as combined tools for the characterization of substrates for epitaxy: the ZnO case," *CrystEngComm*, vol. 15, no. 19, p. 3951, 2013. (Cited on page 84.)

[121] A. Redondo-Cubero, A. Hierro, J.-M. Chauveau, K. Lorenz, G. Tabares, N. Franco, E. Alves, and E. Muñoz, "Single phase a-plane MgZnO epilayers for UV optoelectronics: substitutional behaviour of Mg at large contents," *CrystEngComm*, vol. 14, no. 5, pp. 1637–1640, 2012. (Cited on page 114.)